Alma Mater Studiorum · Università di Bologna

School of Science
Department of Physics and Astronomy
Master Degree Programme in Astrophysics and Cosmology

A numerical study of the hadronic gamma ray emission from cosmic ray protons in radio jets

Graduation Thesis

Supervisor:
Prof. Franco Vazza

Submitted by:
Koushika Sri Lakshmi Srikanth

Academic Year 2022/2023
Graduation date II

Contents

List of Figures

List of Tables

Abstract

This thesis is a numerical study of the gamma ray emission from clusters and it is aimed at constraining the cosmic ray content of jets from radiogalaxies. It involves the simulation and numerical analysis of Lagrangian tracers injected by the jets from radio galaxies into the medium of clusters of galaxies evolving in a cosmological simulation.

Non- relativistic particles can be accelerated to relativistic speeds in different ways like magnetic reconnection, Fermi I, Fermi II acceleration etc., [1]. Relativistic particles, including cosmic ray electrons and protons, exhibit different energy loss behaviors. Cosmic ray electrons primarily lose energy through synchrotron and inverse compton processes, with a short timescale of approximately 10^8 years. On the other hand, relativistic protons, can undergo hadronic interactions and experience energy losses during their propagation through space. Cosmic ray protons participate in hadronic interactions with thermal protons in the gas medium, leading to the production of neutral pions. These unstable pions, given their shorter lifetime subsequently decay into gamma-rays. Therefore, the detection of gamma-rays signifies the presence of cosmic ray protons.

However in the Intracluster Medium (ICM) there are instead only non-reported non-detection of gamma-rays [2]. Since cosmic ray protons do not undergo major losses and have longer lifetime, these constraints can be used to constrain the source or acceleration mechanism present in the environment. My thesis mainly focuses on constraining the composition of cosmic ray protons and electrons injected in clusters of galaxies by radio jets.

I have analyzed different sets of radio jet simulations, in which the cosmic rays are transported into the ICM [3]. I have utilized Lagrangian tracers within the simulations to monitor the transport of cosmic rays originating from the radio jets into the ICM. The jet simulations encompasses a single radio galaxy Vazza et al (2021) A&A, a single radio galaxy with varying powers Vazza et al (2023) A&A and multiple radio galaxies Vazza et al (2023) Galaxies. I have calculated the gamma-ray flux under various radio jet conditions and compared it with the observational data from FERMI LAT. This comparative analysis has enabled me to establish constraints on the allowed cosmic ray

energy content in the radio jets. I concluded that if radio galaxies have multiple bursts, then they violate the FERMI limit. In my simulations, for $N_{burst} = 4$, the gamma-ray flux surpasses the FERMI limit. Therefore, this can be used to limit the cosmic ray energy budget to be $\leq 25\%$ of magnetic field energy in radio jet. This is due to the fact that the initial conditions have an equality between cosmic ray energy and the magnetic field energy. In my thesis I also proved that such limits hold for even variations of the initial jet power. The charged pions in hadronic emission also decay into muons and neutrions. Since neutrino and gamma ray flux are linked by the same process, in my thesis as an additional task I also focus on the injection of neutrinos diffused into the clusters of galaxy by hadronic collision and comparing the neutrino flux with the observational results of IceCube.

Overall my thesis has shown that the joint use of gamma-ray and neutrino data can be used to refine existing physical models of radio jets in clusters of galaxies.

Chapter 1

Introduction

1.1 Galaxy Clusters

Galaxies that are gravitationally bound together form a cluster. According to the Lambda Cold Dark Matter (LCDM) model it is believed that clusters are formed by a hierarchical sequence of mergers and by accretion of smaller systems over the timescale of $10^9 \sim 10^{10}$ years [7]. The "Lambda" (Λ) in LCDM model refers to the cosmological constant, which represents the dark energy responsible for the accelerating expansion of the Universe. The model combines the cosmological constant (dark energy) with cold dark matter as the primary components of the Universe's energy density. The LCDM model predicts that the early Universe had tiny fluctuations in matter density. Over time, under the influence of gravity, these density fluctuations grew, leading to the formation of larger structures. Dark matter plays a significant role in this process, as it acts as the dominant gravitational component, attracting ordinary matter and causing it to collapse into halos, which serve as the building blocks for galaxies and clusters. Clusters are very important cosmological probe in the present day astronomy as they cause gravitational lensing [8]. They could extend to a size of $\sim$ Mpc scale. Clusters can have a few galaxies to hundreds and thousands of galaxies. Galaxy clusters have masses between 10^{14} - 10^{15} $M_\odot$ in which most of the mass (around $\sim$ 70% - 80%) is by dark matter. The plasma present between the galaxies in a cluster forms the hot ICM that has a temperature around $10^8 K$ and a very low number density of 10^{-4} - 10^{-1} cm^{-3}[1]. The strong gravitational energy that bounds the cluster is the main reason for such a high temperature in the ICM because the gas is in approximate virial equilibrium with the gravitational potential of the cluster. The ICM emits thermal X-ray radiation via bremsstrahlung and it is also observed due to the Compton effects of Cosmic Microwave Background (CMB) called as Sunyaev-Zel'dovich (SZ) effect in mm range[1]. The SZ effect can either cause emission or depression ("SZ Decrement") at mm wavelengths. This effect occurs because the CMB photons scattered by the cluster's electrons lose energy when they interact with the cluster while moving towards the observer. The SZ Decre-

ment effect is typically observed in clusters with high temperature or in the presence of large-scale flows in the Universe.

Figure 1.1: Gravitational lensing by Abell 2218 cluster captured by Hubble" [9].

1.1.1 Physical properties of clusters of galaxies

Galaxy clusters are commonly observed as relaxed and dynamically stable systems in equilibrium. In these clusters, galaxies and dark matter exhibit collisionless behavior. On the other hand, the gas component within galaxies can be collisional at larger scales, typically exceeding 10 kiloparsecs (kpc). However, as we examine smaller scales, the gas undergoes a transition towards a collisionless regime. The presence of magnetic fields further complicates the gas behavior, resulting in a "weakly collisional" nature at larger scales due to the interplay between magnetic fields and the gas. Utilizing the framework of collisionless dynamics, we can apply the scalar virial theorem to estimate the mass of the cluster. The scalar virial theorem is a fundamental principle that describes the balance between the kinetic and potential energy of a system, enabling us to infer important physical quantities within the cluster [10].

$$\frac{1}{2}\frac{d^2I}{dt^2} = 2\mathrm{K} + \mathrm{W} + \Sigma \tag{1.1}$$

For a stationary (I (moment of inertia) = constant) system,

$$\mathrm{E} = \text{-}\mathrm{K} = \mathrm{W}/2 \tag{1.2}$$

where,

- E is the total energy,
- K is the kinetic energy,
- W is the potential energy,

- Σ is the external pressure, that is negligible in this case.

$$\begin{aligned} \mathrm{K} &= \frac{1}{2}mv^2 \\ \mathrm{W} &= -\frac{GM^2}{r_g} \end{aligned} \tag{1.3}$$

where $r_g = 2.5 \times r_h$ (half mass radius) The mass of the cluster is given by [10],

$$M_{tot} \simeq \frac{5}{2}\frac{< v^2 > r_h}{G} \sim 6 \times 10^{14} \frac{r_h}{1Mpc}(\frac{\sigma_{3D}}{1000\mathrm{K}m/s})^2 M_\odot \tag{1.4}$$

if we use isotropic velocity distribution, then

$$\sigma_{3D} = \sqrt{3}\sigma_r \tag{1.5}$$

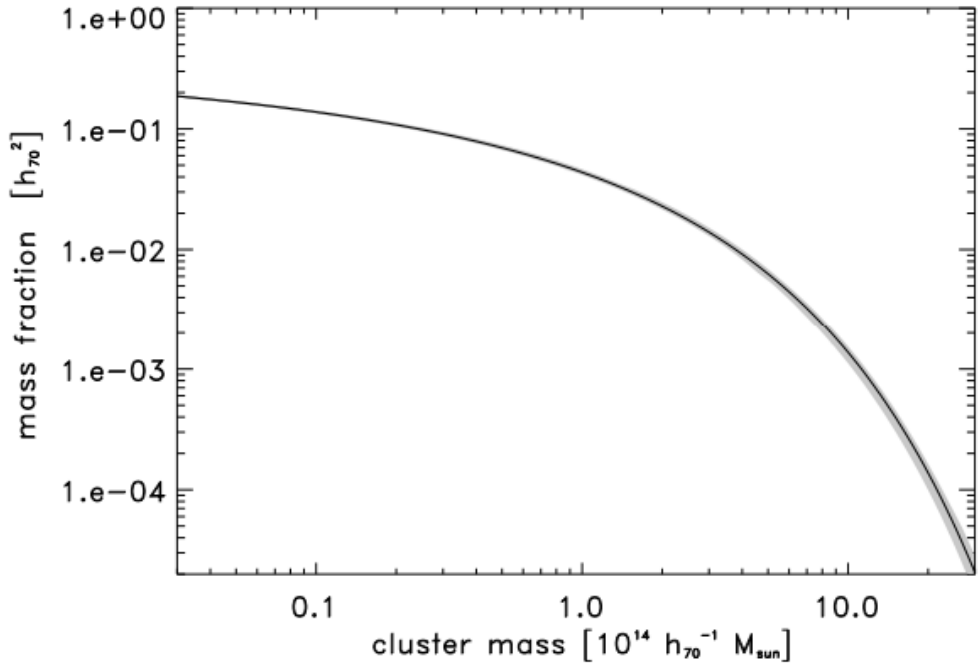

Figure 1.2: Mass fraction bound in groups and clusters of galaxies inside r_{200} at a redshift of zero. The mass fraction in groups and clusters has been normalised by the total amount of matter in the Universe for $H_0 = 70$ km/s/Mpc and $\Omega_m = 0.285$ for the best-fitting model [11].

Within a cluster, a significant number of galaxies are categorized as E-type, elliptical galaxies dominated by old stellar populations and exhibiting minimal dust content. These galaxies maintain a consistent appearance across various wavelengths. In a typical cluster with a mass of $5 \times 10^{14} M_\odot$, E-type galaxies possess a velocity dispersion of approximately 1000 km/s. The stellar mass is only a few percent of total mass as most of the mass is due to dark matter present in the clusters. It is more centrally concentrated, as σ (velocity dispersion) decreases with radius, and is well fitted by a de Vaucouleurs profile or by a

NFW profile. According to Navarro-Frenk-White (NFW) profile, $r_h \sim 0.4 - 0.5 r_{vir}$. Based on the properties of their galaxies, in general clusters are classified as,

- cD clusters- they are regular, compact, have a dense core and massive galaxies are located closer at the center.
- Spiral-rich clusters -they are irregular, with little central concentration, early-type and late-type galaxies are distributed similarly. There is no mass segregation like massive galaxies being located closer to the center.
- Spiral-poor clusters -they have intermediate characteristics.

Massive clusters are considered to be baryonically closed systems, meaning that they retain a significant portion of their baryonic content within their boundaries. Due to their extremely high temperatures, these clusters are less efficient in forming stars. The cosmic ratio of baryonic matter density (ρ_{bary}) to total matter density (ρ_{matter}) is approximately 0.17. In contrast, the contribution of stars to the total matter density, as represented by the ratio of stellar density (ρ_{star}) to total matter density, is approximately 0.02. The deep potential wells of clusters make it unlikely for baryons to escape, leading us to conclude that the majority of baryons within clusters exist in the form of plasma.

For the simplest isothermal case, where both T and σ_r are spatially invariant then by beta model the density profile of the ICM is given by [12] ,

$$\frac{n_{\text{gas}}(r)}{n_{\text{gas}}(0)} = \left(\frac{\rho_{\text{gas}}(r)}{\rho_{\text{gas}}(0)}\right)^{\beta} \tag{1.6}$$

where,

$$\beta = \frac{\mu \cdot m_p \cdot \sigma_r^2}{K \cdot T} \tag{1.7}$$

Using the empirical approximation,

$$\rho_{\text{gas}}(r) = \rho_{\text{gas}}(0) \left[1 + \left(\frac{r}{r_{\text{c}}}\right)^2\right]^{-3/2} \tag{1.8}$$

where r_c is the core radius thus yielding,

$$n_{\text{gas}}(r) = n_{\text{gas}}(0) \left[1 + \left(\frac{r}{r_{\text{c}}}\right)^2\right]^{-\frac{3\beta}{2}} \tag{1.9}$$

This beta model is simple with minimal parameters where the gas density is often described as a power-law profile, and the pressure height scale is related to the core radius and the beta parameter. To understand more about the physical structure of the cluster we can characterize the volume filled up by the hot ICM with the pressure height scale.

The pressure height scale varies based on the density model used to describe the density distribution in the ICM. To derive the expression for the pressure height scale in the simplistic case of a beta model, we can consider the hydrostatic equilibrium in the ICM, where the pressure gradient is balanced by the gravitational force:

$$\frac{dP}{dr} = -\rho_{\rm gas}(r)\frac{GM(r)}{r^2} \tag{1.10}$$

$$\frac{dP}{H_p} = -\rho_{\rm gas}(r) \cdot g \tag{1.11}$$

where dP/dr represents the pressure gradient, $\rho_{\rm gas}(r)$ represents the gas density, G represents the gravitational constant, M(r) represents the total mass enclosed within radius r and H_p represents the pressure height scale. Using the ideal gas equation , we can rewrite the pressure height scale in Eq 1.11 just with temperature as,

$$H_p = \frac{KT}{\mu m_p g} \tag{1.12}$$

For T = 10^8 K $\rightarrow$ $H_p \sim 0.5$ Mpc.

1.1.2 Timescales in clusters of galaxies

There are different kinds of timescales that have to be considered to have a complete analysis of dynamics of a galaxy cluster. The crossing time is the time taken for gravitationaly bound galaxies to cross or move inside the cluster. This time is similar to dynamical or free fall time [10].

$$t_{cr} = \frac{2R}{v} \tag{1.13}$$

where v is the typical velocity of the system

$$v \sim (\frac{GM}{R})^{1/2} \tag{1.14}$$

The next important timescale is the relaxation timescale. This is the time required to relax for a 2-body system after encounters. It also defines whether the system is collisional or non-collisional [10].

$$t_{relax} \sim \frac{0.1N}{lnN}\frac{R}{v} \tag{1.15}$$

where, N is the number of particles or galaxies. For a whole cluster with N $\sim$ 1000, v$\sim$1000 km/s and R$\sim$1 Mpc it takes 14 Gyr to relax which is close to the age of the Universe. The last timescale, is the direct collisional time. Consider a system of size R

with N particles, each of radius r_p, direct collison time is given by [10],

$$t_d = \frac{4\pi \mathrm{R}^3}{3N\pi r_p^2} \frac{R}{v} \frac{1}{R} \tag{1.16}$$

For a stable equilibrium cluster, the following condition must be satisfied,

$$t_{cr} \ll \text{age of the Universe} \ll t_{relax} \ll t_{cool} \ll t_d \tag{1.17}$$

The parameter t_{cool} represents the cooling time during which the cluster can dissipate energy through radiative cooling mechanisms. The timescale becomes significant when there are processes that allows radiative cooling in the cluster (Subsec 1.2.1).

1.1.3 Metallicity in clusters of galaxies

Supernova explosions play a crucial role in enriching the ICM with metals. It is widely believed that clusters of galaxies represent "chemically closed systems," where the metals produced by supernovae remain gravitationally bound within the ICM, possessing high potential energy and thus remaining confined to the cluster [13]. Metallicity serves as a valuable tracer for studying various processes within a cluster, such as star formation rates, supernova explosions, and the yields of these explosions. Additionally, it aids in understanding the gas cycle between galaxies and the ICM. The expected metallicity in the ICM can be determined through various observational methods and theoretical models, providing insights into the chemical composition and evolutionary history of clusters. The expected metallicity in ICM is given by [14],

$$< Z_{Fe} >_{ICM} = 3.64 \times 10^{-3} \frac{M_*}{M_{ICM}} \sim 0.47 Z_\odot \tag{1.18}$$

where M_* is the stellar mass. If we take into account that some Fe is still locked inside the star then the metallicity is around 0.23 $M_\odot$. On an average the total cluster metallicity is given by $< Z_{Fe} >_{cluster} \sim 0.38 M_\odot$ [14].

1.2 Non-Thermal process in clusters of galaxies

Non-Thermal processes are very important as they provide us more information regarding the source of relativistic particles in the cluster [4]. Through this study of cosmic rays in the ICM, we can learn about the fundamental physics of Diffusive Shock Acceleration (DSA), large scale magnetic fields in the ICM and also the turbulence that remains as a source for accelerating relativistic particles. Non-Thermal processes are responsible for several emission processes like synchroton radiation, inverse Compton and hadronic emission of gamma rays. Relativistic charged particles inside a magnetic field accelerate

perpendicular to the magnetic field and the velocity vectors and electro-magnetic radiation is emitted in the form of synchroton radiation. To conserve momentum in B field, a photon is released when the electron bends due to the magnetic field. In case of clusters, cosmic ray electrons in a magnetised plasma ($\sim \mu$G) [15] produces synchroton radiation in radio waves. It is also possible to have inverse Compton of synchroton produced radio waves in X-rays [1]. On the other hand, when cosmic ray protons collide with target thermal protons, they produce pions which then decays into gamma rays (Sec 1.14).

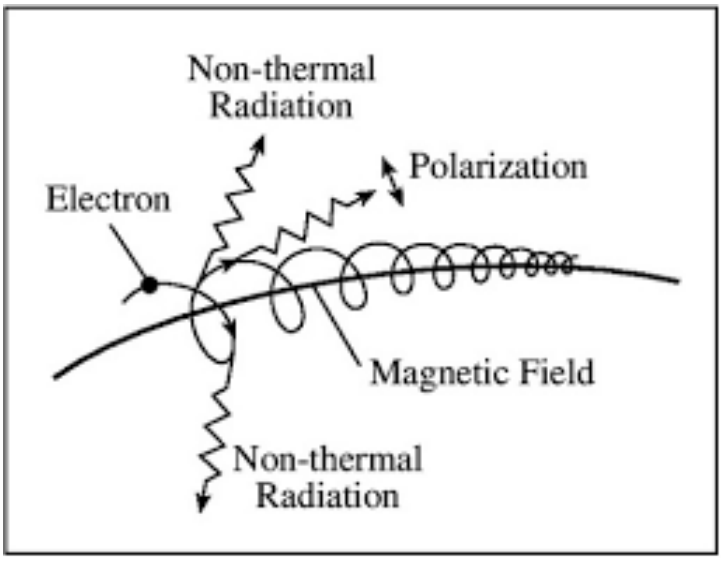

Figure 1.3: Representation of an electron losing energy in a magetised field due to synchrotron.

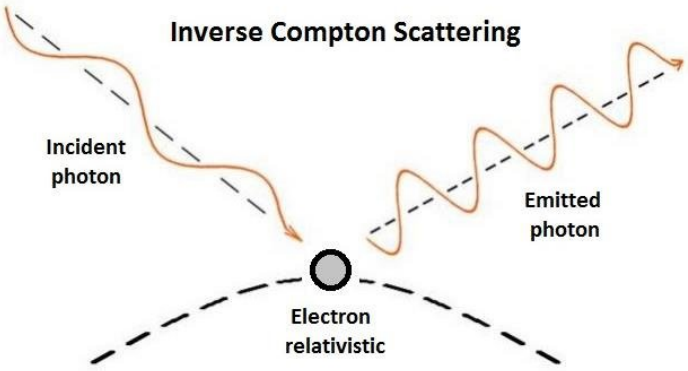

Figure 1.4: Low energy photon is upscattered by a relativistic electron [16].

The rate of energy loss by synchroton and Inverse Compton process is given by [17],

$$(dE/dt)_{synch} = \frac{-4}{3}\sigma_T \gamma^2 \beta^2 (U_B)^2 \tag{1.19}$$

$$(dE/dt)_{IC} = \frac{-4}{3}\sigma_T \gamma^2 \beta^2 (U_{ph})^2 \tag{1.20}$$

where,

- σ_T is the Thomson cross-section,
- γ is the Lorentz factor,
- β is the Doppler factor (speed of the particle v/ speed of light c),
- U_B is the magnetic field energy density which is given by, $B^2/8\pi$,
- U_{ph} is the photon energy density.

When synchrotron emission happens due to an ensemble of electrons in a region then the emissitivy function is given by [17], $j_\nu(\nu) = N_0 B^{\alpha+1}\nu^{-\alpha}$, where $\alpha = \frac{\delta-1}{2}$ is the spectral index, representing the slope of the photon energy spectrum.

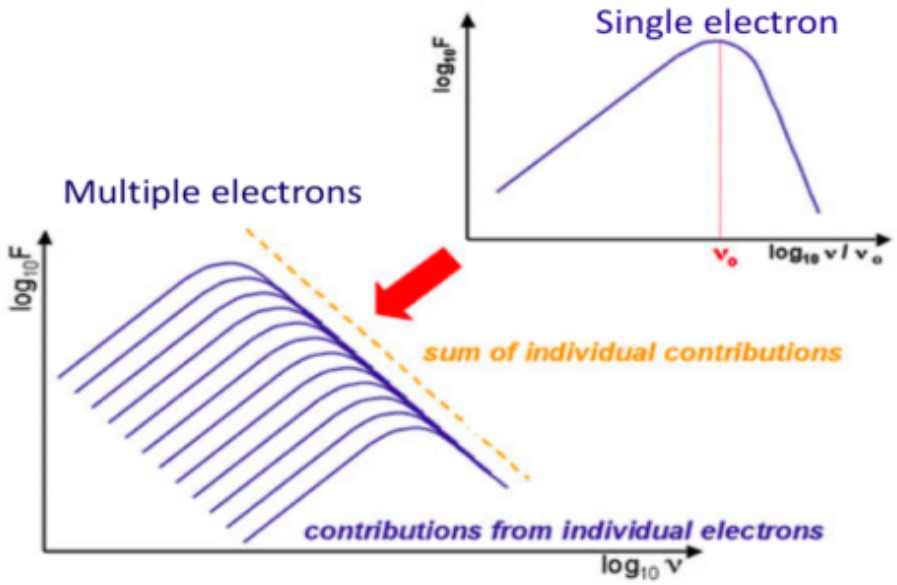

Figure 1.5: Synchrotron emission due to multiple electrons.

1.2.1 Cooling time

The cooling time for synchrotron emission depends on the strength of the magnetic field [17].

$$t_{\text{cool,syn}} \sim \frac{(\gamma-1)mc^2}{\frac{4}{3}\sigma_T c\gamma^2\beta^2 U_B} \tag{1.21}$$

For an Interstellar Medium, the cooling time is given by 10^8 year and for radio galaxy it is 0.1 s. The difference in cooling time totally depends on the strength of magnetic field. The Inverse Compton cooling time is also similar to Eqn 1.21, except that magentic field energy density is replaced by the photon energy density. In a given medium with electrons and a field of photons, we can have both Compton and Inverse Compton scattering, depending on the average energies; these processes cause the modification of

the photon spectrum. In order to derive the spectral shape, the diffuse equation known as Kompaneets equation must be solved [18].

$$\text{Comptonization parameter } y = \frac{\Delta E}{E} N_{\text{scatt}} \tag{1.22}$$

$$E = E_0 e^y \tag{1.23}$$

The detailed explanation of synchrotron and inverse Compton process in cosmic rays is explained in Subsec 1.10.2.

1.3 Fermi I and Fermi II acceleration

Fermi mechanisms are very important as they explain Galactic and extra-Galalactic cosmic rays. Fermi-I acceleration is related to acceleration of particles by shocks and Fermi-II is related to acceleration by turbulence. The key result of Fermi's theory is [19],

$$N(E) \propto E^{-p} \tag{1.24}$$

The power law index 'p' represents the relationship between energy and the number of particles within that energy range. It can be determined through the DSA method, which statistically connects it to the maximum energy attained by the particles for strong shocks. According to DSA the power law index 'p' is 2, which corresponds to the flattest spectrum achievable. Figure 1.6 shows that the low energy cosmic rays are due to Fermi accelerations from our own galaxy, while the high energy part are due to acceleration from extra galactic regions. To understand the concept of Fermi accelerations let's assume elastic particle-cloud collisions or "moving-mirror" collisions. In a head-on collision, the particles are always accelerated with $cos\theta > 0$. On a rear-on collision the particles are decelerated, $cos\theta < 0$. The increase in energy per collision is given by [19],

$$\frac{\Delta E}{E} = \frac{2vVcos\theta}{c^2} + \frac{2V^2}{c^2} \tag{1.25}$$

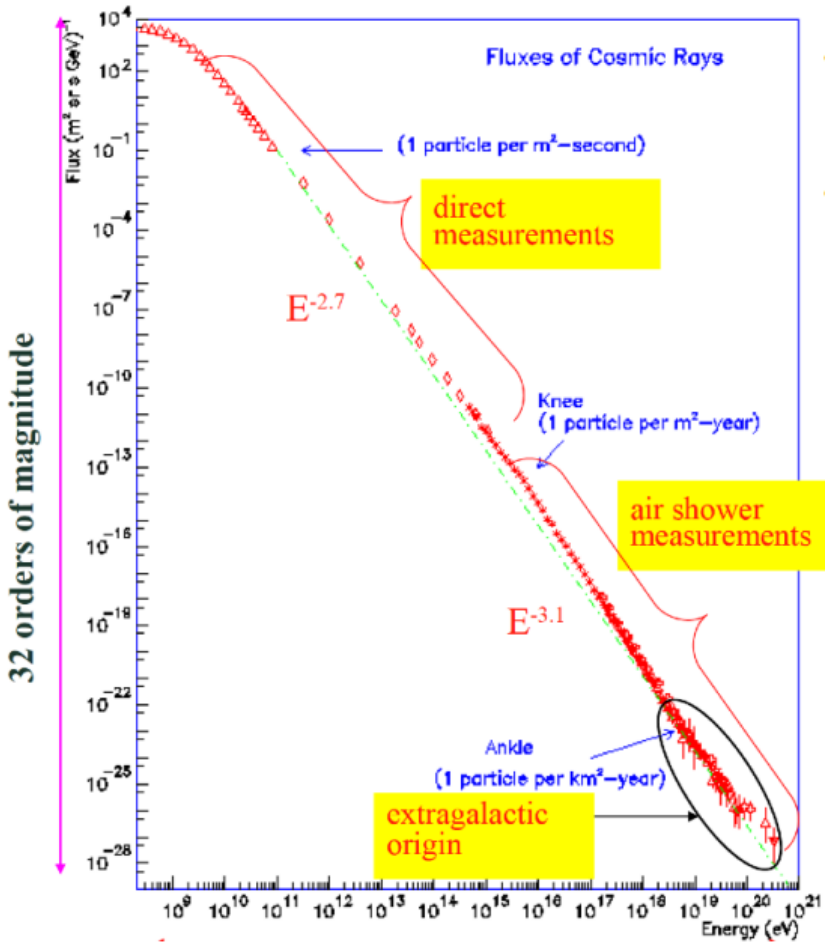

Figure 1.6: Energy vs Flux of cosmic rays, a power law spectrum [20].

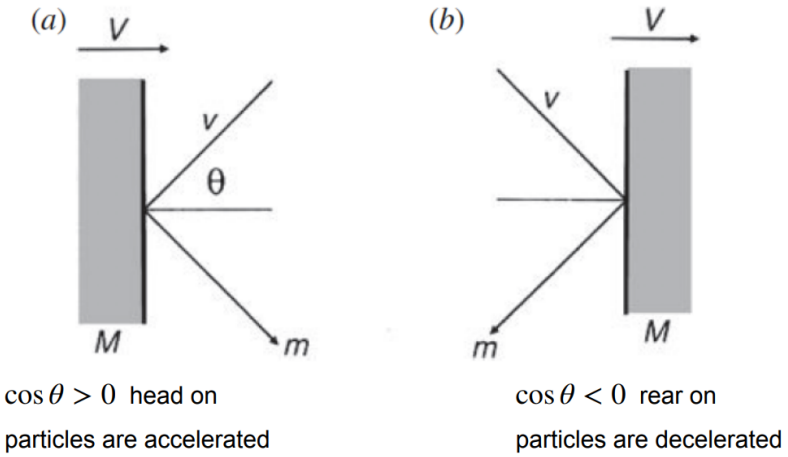

Figure 1.7: a) represents head on collision b) represents rear on collisions [19].

where

- v is the velocity of the particle,
- V is the velocity in which the cloud is moving,

- θ is the angle at which the particle and the cloud collide,
- c is the speed of light.

The first term in **Eq 1.25** is called the stochastic term, and it depends on the angle at which the particle and cloud collide. The second term in **Eq 1.25** is called systematic term, and it depends only on the velocity of the cloud. If the stochastic term dominates we have Fermi-I acceleration, and if the systematic term dominates we have Fermi-II acceleration. Averaging over the angles we obtain the average acceleration efficiency or the net Fermi acceleration as [19],

$$\frac{< \Delta E >}{E} = \frac{8V^2}{c^2} \tag{1.26}$$

Since the average acceleration does not depend on angle and velocity of the particle, it can be termed as Fermi II acceleration. Similarly, the rate at which the energy is increased can be calculated from [19],

$$\frac{dE}{dt} = \frac{4V^2 E}{3c\lambda} \tag{1.27}$$

where λ is the size of the cloud. In regions where ionisation losses are high, as in typical ISM condition in Milky Way, we have an insufficient acceleration. The particles in those regions get accelerated only by Fermi-I acceleration. Fermi-I mechanism can explain Galactic and even extra-Galalactic cosmic rays from supernovae, due to the strong shocks present.

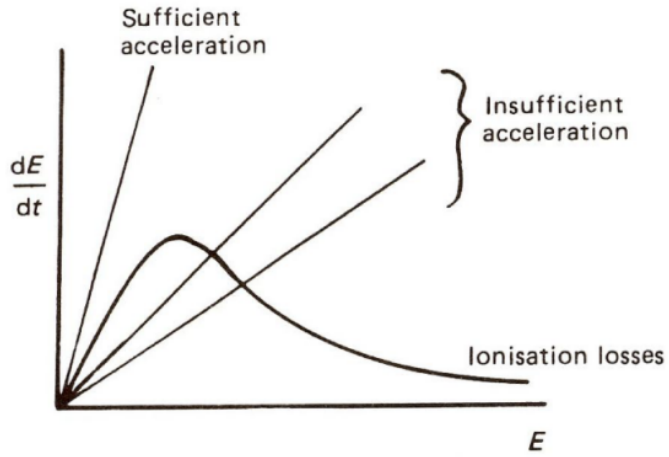

Figure 1.8: Comparison of the acceleration rate and energy loss rate due to ionisation losses for a high energy particle [19].

1.4 Diffusive Shock Acceleration

The specialisation of Fermi-I acceleration in the case of shocks is explained by DSA theory. DSA theory allows us to link the power law index p to the Mach number in **Eq 1.25**. As mentioned earlier, for strong shock predictions, M $\rightarrow \infty$ and the power law index p $\rightarrow$ 2 by DSA [19].

$$p = 2\frac{M^2 + 1}{M^2 - 1} \tag{1.28}$$

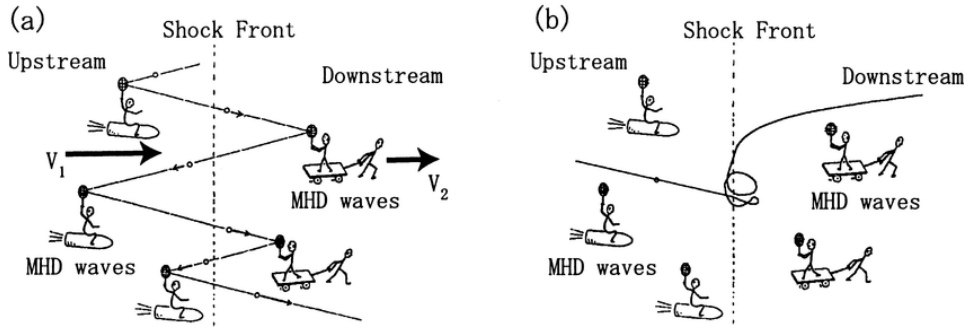

Figure 1.9: (a) An illustration of the diffusive shock acceleration mechanism (b) An illustration of thermal particles at shock transition [21].

According to this theory, thermal particles experience a single bounce across the shock, resulting in a decrease in their velocity downstream of the shock. Their gyro-radius remains small, and their kinetic energy becomes thermalized within the downstream region of the shock. In contrast, as illustrated in Fig 1.9 cosmic rays undergo multiple back-and-forth bounces across the shock, allowing them to be accelerated to very high energies. Compared to thermal particles, cosmic rays have a larger final gyro-radius. Larger the gyro-radius of a particle within the shock, the greater the velocity jump it experiences, leading to relativistic speeds through Fermi acceleration. During the process of DSA, particles are typically injected from a Maxwellian distribution. If these particles undergo acceleration, they contribute to the power-law distribution of energy. However, the specific minimum energy required for a particle transition from the Maxwellian distribution to the power law remains uncertain, and this is referred to as the "injection problem." There is a minimum momentum at which particles can be injected from the Maxwellian distribution, determining their entry into the power-law regime which is given by [19],

$$P_{min} = q_{inj} P_{thermal} \tag{1.29}$$

Where,

- q_{inj} is $\sim$ 3-4. Even with advanced simulations constraining q_{inj} is not easy, because in reality there is no clear numerical boundary, but a “window function” , i.e. smooth range of high values , with different probabilities to start the acceleration.

- $P_{thermal}$ is given by,

$$P_{thermal} = \sqrt{2m_p k_p T} \tag{1.30}$$

m_p is the mass of the proton, k_p is the Boltzmann constant, T is the temperature of the medium.

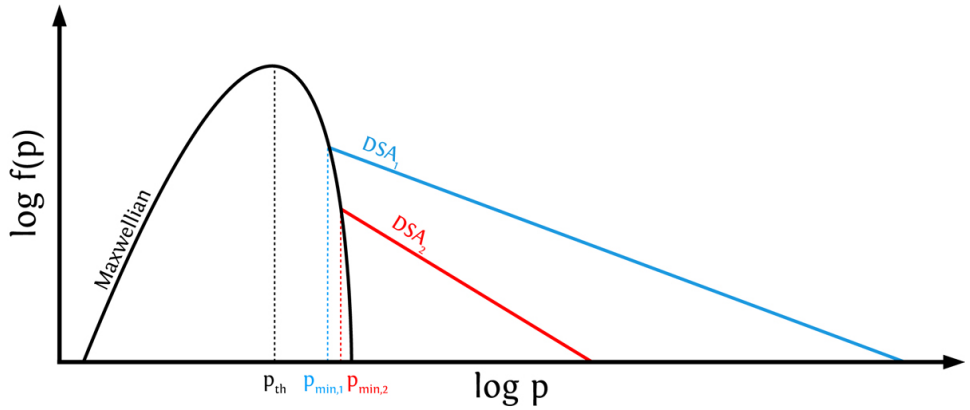

Figure 1.10: Different slopes of DSA based on injection momentum in the maxewellian distribution [22].

1.5 Radio halos and Radio relics

In galaxy clusters, two types of acceleration processes, known as Fermi-I and Fermi-II acceleration are believed to give rise to distinct radio emission phenomena: radio relics and radio halos respectively. Radio relics are observed at the outskirts of galaxy clusters and exhibit highly polarized emission. They are believed to trace shock waves resulting from cluster mergers. On the other hand, radio halos are detected in the central regions of galaxy clusters. They typically follow the distribution of X-ray emission and are thought to be generated by turbulence induced by cluster mergers. The turbulent motions in the ICM accelerate electrons, which in turn emit synchrotron radiation, producing the observed radio halos. Radio relics are due to the shocks dissipated by mergers. Additionally, there are also shocks generated by jets originating from Active Galactic Nucleus (AGN). As the jets propagate through the ICM, they create shock due to the interaction with the surrounding gas. These shocks compress and heat the plasma, leading to the acceleration of electrons and protons to relativistic energies. The accelerated particles then emit synchrotron radiation, which is observed as the radio emission associated with the radio relics and halos which is explained in detail in Subsec 1.6. Rankine-Hugonoit jump conditions are used to calculate the temperature, mach number and pressure across the downstream of the shock. These shocks are weak with a low mach number $2 \sim 3$. Particles are accelerated at the radio relics by DSA. The spectral index found at the relic

is related to the Mach number by,

$$\alpha_{inj} = \frac{1}{2} - \frac{M^2 + 1}{M^2 - 1} \tag{1.31}$$

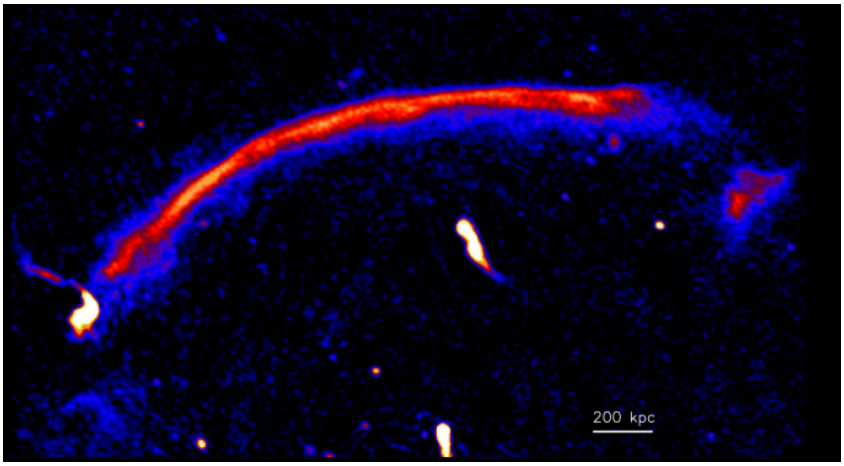

Figure 1.11: Sausage relic found in the cluster CIZA J2242+53 [23].

The tangled magnetic fields in the ICM are compressed, amplified and aligned with the propagating shock plane, generating strong linearly polarized emission in relics. The main problems with radio relics is the life time of cosmic ray electrons (10^8 years which is less than the age of clusters) and acceleration efficiency of such a weak shock (M $\leq$ 5). The possible solutions for this problem could be shock re-acceleration, where the electrons are already accelerated before reaching the relics and still not emitting in radio. The suggested mechanisms where the electrons are re-accelerated include shock drift, multiple shock acceleration etc., ([22],[24]) On the other side, looking into radio halos they are diffuse, patchy emissions that are unpolarised and centrally located. Fermi II acceleration of electrons in the turbulent ICM provides a good explanation for observed radio halos.

1.6 Radiogalaxies in clusters

Radio emission from active galaxies driven by jets on scales from $\sim$ pc to $\sim$ Mpc scale are termed as radio galaxies. These radio galaxies can be further classified into FRI (Fanaroff-Riley) and FRII galaxies. FRI galaxies are edge-darkened while FRII are edge-brightened [25]. This phenomenon likely occurs because of the high jet power of FRII, which allows it to travel over longer distances and create hotspots. The abrupt termination of shocks within FRII contributes to the formation of hotspots. Additionally, these shocks serve as active regions where particles can be accelerated to reach relativistic speeds. The substantial radio emissions observed are a result of the synchrotron process, where relativistic electrons interact with the highly magnetized environment [26]. Using

the excitation index (EI) (the ratio between the [OIII] line and the Hβ line, minus the lines of other elements, such as [NII], [SII], [OI]) as a proxy, the radiative efficiency of the accretion disc radio galaxies could be classified as High Excitation Radio Galaxy (HERG) and Low Excitation Radio Galaxy(LERG).

- EI $>$ 0.95 - HERG - Efficient accretion disk, Shakura-Sunyaev disk. This disk has a large amounts of gas flow inwards, feeding the BH through a radiatively efficient disc; this mode may have a role in reducing star formation at high redshift and setting up the observed Magorrian relation (correlation between black hole mass and velocity dispersion in the bulge Ref Subsec1.7) through radiative feedback.
- EI $<$ 0.95 -LERG - Inefficient accretion disk, Advection domination accretion flow (ADAF). In ADAF the material is accreted onto the BH in a radiatively inefficiently way, leading to a limited radiation. There are cases where the radiation efficiency of the accretion is insufficient to emit all the E_{grav} liberated in the disc. So, a part of the energy is then advected with the adiabatic flow, instead of being radiated from, and the accretion flow then ultimately is accreted beyond the horizon of the Black hole. Thus, the flow retains most of it energy and does not radiate/cool efficiently.

In FR I the jets are thought to be decelerated, to become sub-relativistic on scales of pc to kpc and their nuclei are powered by an inefficient engine (LERG). In FR II the jets are at least moderately relativistic and supersonic from the core to the hot spots and most of their nuclei are powered by an efficient engine (HERG).

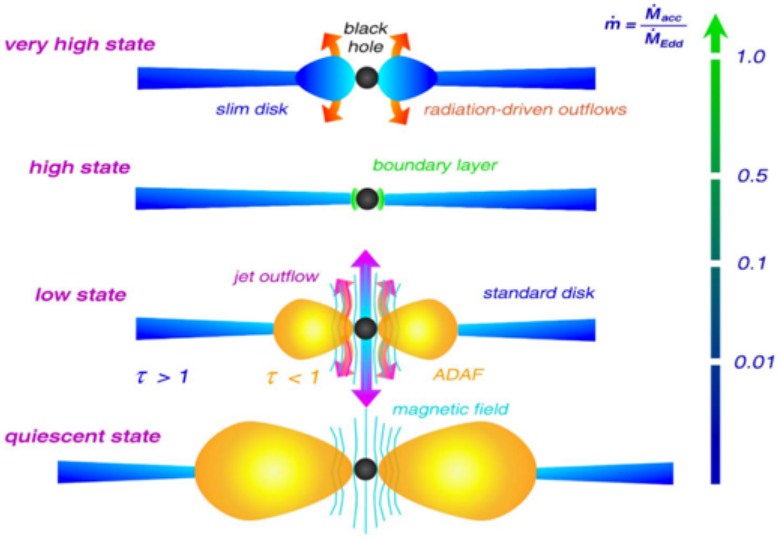

Figure 1.12: The schematic figure of the state of a black hole accretion disk [27].

Galaxy clusters hosts thousands of galaxies in which a few active radio galaxies are present. The jets and lobes of radio galaxies in a cluster interact with the ICM resulting

in different morphologies like WAT (wide-angle), NAT (Narrow-angle) and head-tail radio sources [26].
A new class of radio galaxy has been introduced which is termed as FR0. They are extremely compact radio galaxies (< 10 kpc) often unresolved at very high resolutions. In FR0 radio galaxies the ratio between the core and the total emission is ~ 30 times higher than the FR I. FR0 have moreover same properties as FRI except for the extension of radio jets.

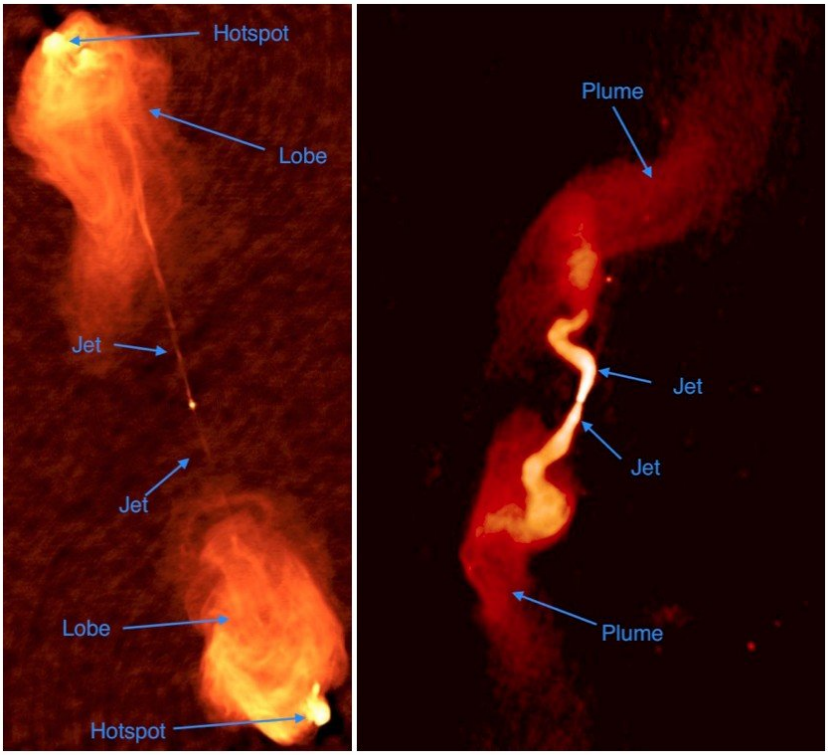

Figure 1.13: Powerful FR II radio jets in CygnusA (left) and the weak FRI jets in 3C 31 (right) from the VLA (Very Large Array) radio maps [28].

It is well-known that the ICM within galaxy clusters loses its energy through X-ray emission, which should result in a rapid cooling process at the cluster's center. Without any counteracting heating mechanisms, the ICM is expected to cool down within a relatively short time frame of around 1 Gyr, which is shorter than the age of the clusters. Additionally, this cooling process would lead to an increased Star Formation Rate (SFR) in the cluster, which contradicts observations since such a high SFR is not commonly observed. To address this cooling problem, one possible solution is the presence of heating mechanisms within the system that can balance the radiative losses in the ICM. One potential source of heating could be radio galaxies, which plays a significant role in supplying energy to the ICM. This idea is supported by the observation of numerous cavities within cool core clusters. These cavities are formed when the radio plasma from the jet displaces the X-ray emitting plasma, creating empty regions or cavities. Due to buoyancy forces, these cavities rise and expand into the ICM, effectively distributing

the energy into the surrounding medium [29]. Chandra images of Perseus and Cygnus-A clusters have uncovered numerous disruptions, including ripples, shocks, and abrupt changes in density, within clusters' cores. Comparatively analyzing these images with radio data at a similar angular resolution has demonstrated that AGN jets are responsible for many such disruptions [30]. This will be discussed further in the Section 1.7

1.7 AGN feedback in Galaxy clusters

The AGN is fueled by the accretion of matter into the black hole situated at the center of the galaxy. The immense energy released by the AGN can significantly influence the evolution of the host galaxy throughout its lifetime. This process, which involves the energy released by the AGN into the surrounding gaseous environment and its subsequent effects on the galaxy's evolution, is known as AGN feedback. AGN feedback plays a crucial role in regulating the fuelling of the nucleus, thereby controlling its duty-cycle and impacting various aspects of the host galaxy's evolution [31]. AGN feedback has far-reaching consequences, influencing various aspects such as galaxy formation and the observed correlation between black hole mass and velocity dispersion in the bulge, often referred to as the Magorrian relation. Local M_{BH} - galaxy relations are the result of a balance between AGN activity, which tends to expel the gas, and galaxy gravitational attraction, which tends to retain it.

The balance between mass of galaxy and black hole is found at $M_{BH} \sim 0.001 M_{sph}$ (Mass of spheroidal virial mass) [32]. AGN feedback is also considered as a potential solution to the cooling flow problem observed in galaxy clusters, where the rate of star formation continues at a diminished pace [30]. When matter accretes onto a black hole, it releases energy in the form of radiation, given by the equation $E_{BH} = \epsilon M c^2$, where $\epsilon \approx 0.1$ represents the radiative efficiency. For supermassive black holes (SMBHs) with masses around 10^9 solar masses ($M_\odot$), the total energy released can reach an astounding value of 10^{62} ergs [30]. Even a small fraction of this energy can entirely blow away the gas content in the bulge thus preventing the cooling flows and limiting the star formation. Since clusters of galaxies consist the most of the baryons and active galaxies, studying them will help our understanding in the feedback mechanism that regulates the galaxy formation. This feedback is a negative feedback where the star formation is inhibited and prevents the host galaxy in becoming too massive that can disrupt the balance in the surrounding environment. Negative feedback from AGN helps account for the BH mass-σ correlation and for the luminosity function of massive galaxies.

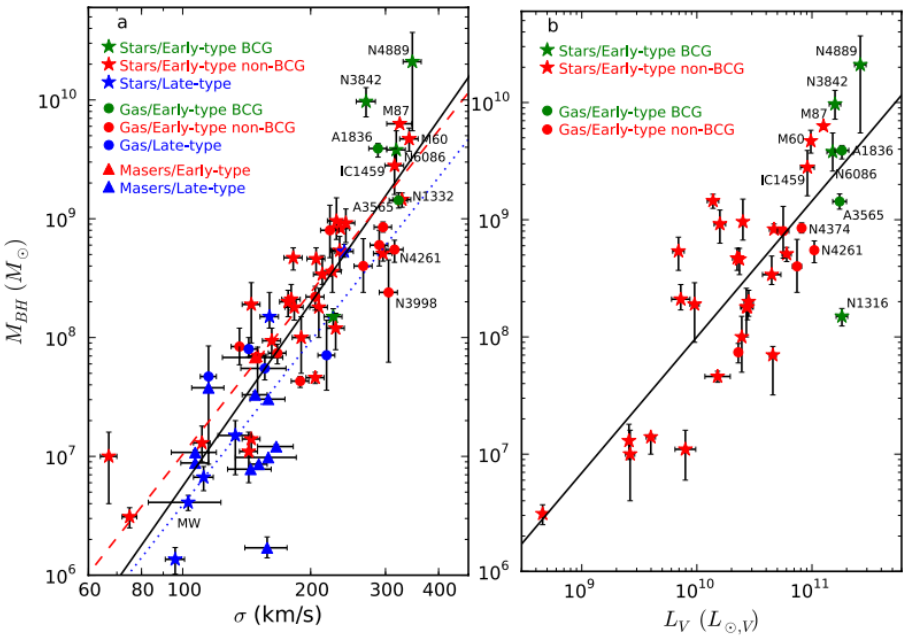

Figure 1.14: Mass of the Black hole vs spheroidal velocity dispersion [33].

Simultaneously, the activity of AGN can also lead to positive feedback on the star formation rate. This occurs when the pressure exerted by the AGN surpasses the dynamic pressure governing the surrounding medium. As a result, the AGN can trigger star formation by compressing dense clouds within its vicinity. Numerical simulations provide evidence that the increased pressure generated by AGN-driven jets can compress the gas within a disk, leading to an enhanced star formation [34].

AGN feedback can happen in two different modes. The quasar (or radiative) mode is referred to high luminosity AGN, i.e. those emitting close to the Eddington limit, where most of the energy is released by radiation (or a wind). They are radiatively coupled process as wide-angle winds are launched from the accretion disc and driven by the coupling of the radiation to the ambient medium. The jet (or kinetic) mode is dominant in low-power AGN where the radio plasma provides the main source of energy [31]. It prevents the gaseous atmosphere from cooling back into the galaxy. It is a mechanical coupling process where parsec-scale jets can produce over-pressured cavities from which the wide-angled outflows can be driven by the mechanical action of the radio plasma emanating from the AGN [35].

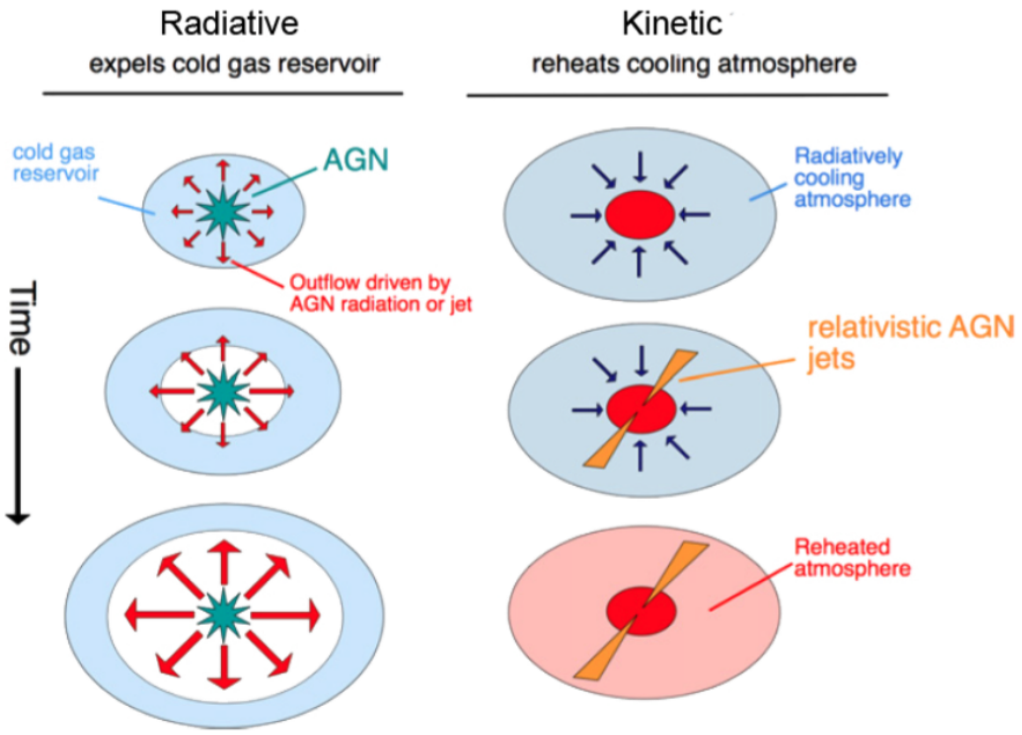

Figure 1.15: Representation of radiative and kinetic mode [36].

1.8 How do clusters accelerate particles?

There are multiple sources and mechanisms that contribute to the production of relativistic particles within a cluster. One significant source is radio jets associated with AGN which transport relativistic particles into the ICM. Additionally, the presence of highly polarized magnetic fields and turbulence within the cluster can lead to Fermi II acceleration, where particles gain relativistic energies through multiple scattering events. In ICM, the Reynold's number is very high ($\mathrm{Re} >> 10^3$) which makes it a perfect spot for turbulence. Turbulent fluctuations arising from continuous accretion processes can re-accelerate particles, providing a plausible explanation for the presence of radio halos observed in some clusters. Furthermore, highly magnetized fields within the cluster can facilitate particle acceleration through magnetic reconnection. Although particles accelerated through this mechanism may have lower energies compared to those accelerated by shocks or other mechanisms, they can still serve as active regions for the re-acceleration of particles. It is important to note that cosmic ray electrons have a life time of 10^8 years and some re-acceleration mechanisms are required to explain their presence on larger scale. Thus, turbulent sites behave as an excellent site for re-acceleration of cosmic ray electrons.

The merger and accretion shocks between galaxies, shocks in radio jets, weak merger

shocks (around Mach 2) during collision of clusters causes Fermi I acceleration of particles. Inspite of being the most energetic events since Big Bang, cluster-cluster mergers produce weak shocks. This is due to the fact that speed of sound in ICM is close to the circular velocity of self-gravitating system producing a weak shock around Mach $1 \sim 2$. Cluster merger shocks can be detected via X-ray observations. The discontinuities in the surface brightness and temperature of X-ray observations highlights the presence of shocks. Finally, thermal leakage of particles in high energy tail of Maxwellian distribution into DSA can also accelerate particles.

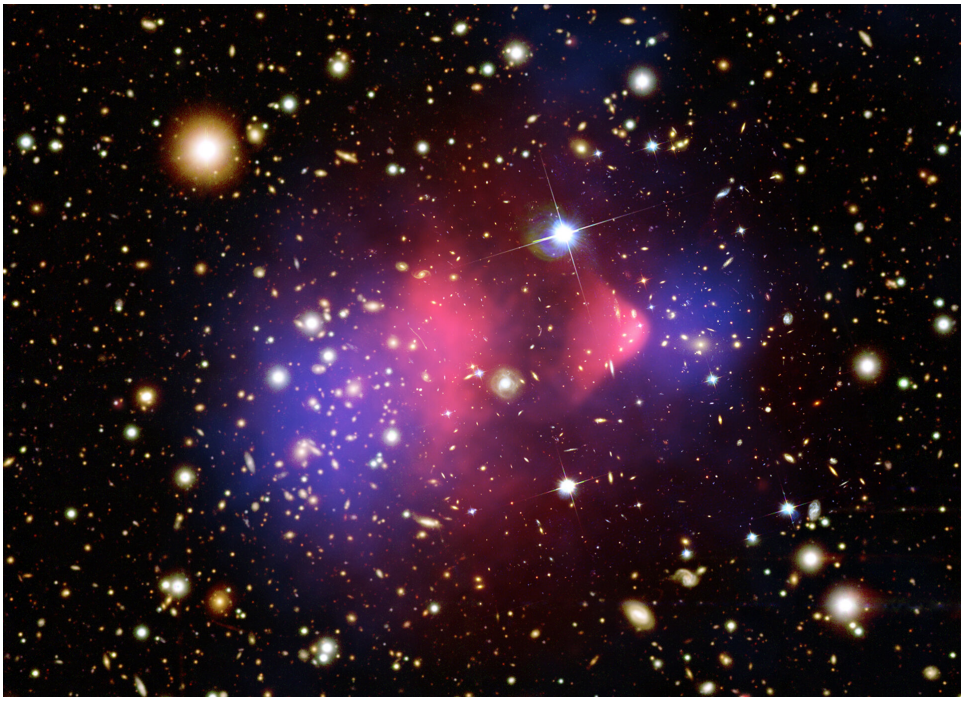

Figure 1.16: Bullet cluster - galaxy cluster that has collided head on. Chandra X-ray image, shows the hot intracluster gas (pink) and gravitational lensing due to Dark Matter present(blue) [37].

1.9 Cosmic rays in clusters of galaxy

Clusters of galaxy are considered to be a storehouse of cosmic rays. As discussed in earlier sections supernovae explosions, pulsars, AGN, merger shocks produced by gravitational energy dissipation , accretion shocks (also known as "external shocks") accelerate cosmic ray particles. Merger shocks are formed during the merging of two clusters with a weak mach number of M$\sim$ 1.4. This is due to the fact that during collision, the collisional velocity is the free fall velocity which is given by [19],

$$v_{infall} \sim \sqrt{\frac{2GM}{R}} \tag{1.32}$$

And the sound speed of the ICM is equal to the circular velocity of a self-gravitating system,

$$c_s \sim v_{circ} \sim \sqrt{\frac{GM}{R}} \tag{1.33}$$

Therefore, the typical Mach number (M $\sim v_{infall}/c_s$) is around 1.4.
Accretion shocks arise from the ongoing accumulation of matter from distant regions, spanning several Mpcs, towards the central core of the cluster. These shocks generate powerful disturbances with Mach number greater than 10. It has to be taken into account that strong shocks formed in less dense region dissipate less energy when compared to weak shocks formed at the high dense region. A small portion of the kinetic energy flux in the shock surfaces of accretion shock is transferred to internal shocks that form during merger events. Even if a small amount of shock dissipated energy can be converted into non-thermal particles then significant population of cosmic rays must be present, including cosmic ray protons [1].

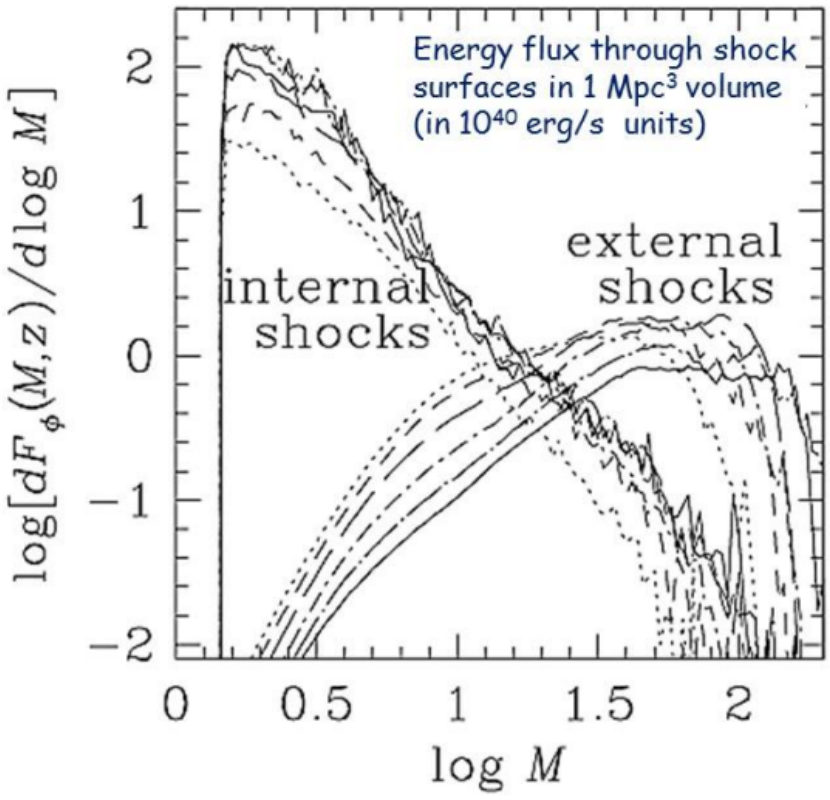

Figure 1.17: Distribution of the energy flux at shocks surfaces as a function of the shock-Mach number from numerical simulations [38]. The units are in 10^{40} ergs/s $(1+z)^3$ h^3 Mpc^{-3}.

The acceleration time required depends on the time interval between shock crossing of

the cosmic rays and is given by [1],

$$\tau \sim \frac{4DV_p}{V_{shock}} \tag{1.34}$$

where, D is the diffusion coefficient, V_p is the velocity of the particle and V_{shock} is the velocity of the shock. Since acceleration time is inversely proportional to shock velocity, higher the mach number the acceleration time reduces. However ultimately the amount of cosmic rays in the ICM totally depends on how efficiently these particles are transported into the ICM.

The formation of cavities within galaxy clusters due to AGN was already discussed in Section 1.6. These cavities have been observed in approximately one-fourth of the galaxy clusters surveyed by the *Chandra* observatory. They possess a significant amount of energy ranging from 10^{55} to 10^{66} erg. These cavities contribute around 1% of the total energy of the ICM $E_{\rm gas}$, and their lifetime corresponds to the buoyancy timescale, which typically ranges from 10^7 to 10^8 years. Although the energy of cosmic rays within these cavities fills a considerable portion, the mechanism by which they are diffused throughout the entire volume of the ICM remains unclear. The diffusion process may involve convective and turbulent mixing, with uncertainties regarding the amount of energy retained by cosmic rays after losses. In the case of low-luminosity AGNs, it is suggested that the energy distribution occurs more easily through ICM turbulence and the sloshing effect. Numerical simulations support the idea that approximately half of the AGN's power is irreversibly deposited into the ICM in the form of shocks which in turn accelerate the cosmic ray particles [1].

In addition to AGNs, all galaxies contribute to the cosmic ray content in the ICM through supernova events. The number of supernovae encountered by an average cluster since its formation (N_{SN}) can be estimated by examining the metal enrichment in the ICM, assuming that these metals originate from supernova explosions. Utilizing this information, we can determine the overall energy budget in the form of cosmic ray protons (CR_p), as they are more effectively accelerated than electrons within supernova remnants (SNRs). The energy budget of comic rays contributed by supernovae is given by [1],

$$E_{CR}^{SN} = N_{SN}\eta_{CR}^{SN}E_{SN} \leq \frac{[Fe]_{\odot}X_{cl}M_{cl,gas}}{\delta M_{Fe}}E_{SN}\eta_{CR}^{SN} \tag{1.35}$$

where,

- $[Fe]_{\odot}X_{cl}M_{cl,gas}$ is the mass of iron in the ICM ($[Fe]_{\odot} \sim \frac{4}{10^5}$ is the iron abundance, $X_{cl} \sim 0.35$ is the typical metallicity measured in galaxy clusters, $M_{cl,gas}$ is the baryon mass of the cluster.

- δM_{Fe} is the iron mass available from single supernova explosion into the ICM.
- $E_{SN} \sim 10^{51}$ ergs is the kinetic energy of supernova.
- η_{CR}^{SN} is the fraction of SN kinetic energy in the form of CRp.

Assuming the absence of adiabatic losses and the transport of CRp from supernovae to the ICM, the following represents the anticipated CRp content in galaxy clusters. Eq 1.35 implies a ratio between CRp and thermal energy budget in galaxy clusters as $\frac{E_{CR}^{SN}}{E_{gas}}$ $\sim 10^{-3}$ for $\delta M_{Fe} \sim 0.1 M_{\odot}$ (typical for a Type II supernovae) and $T_{gas} \sim 10^{8} K$ [1].

1.10 Energy losses in cosmic rays

There are different ways in which cosmic rays in the ICM can lose their energy. Ionisation losses, adiabatic losses, synchrotron emission, inverse Compton emission etc.,

1.10.1 Ionisation losses

When high-energy particles, such as cosmic rays, interact with a solid or gas, they can cause significant damage to the atoms, molecules, and nuclei of the material. These particles have enough energy to excite or ionize the atoms and molecules they encounter, leading to various effects. In case of molecular clouds, which are dense regions in space where stars and planetary systems form, cosmic rays can play a crucial role. Molecular clouds are optically thick, meaning that radiation has difficulty ionizing the atoms and molecules within them. However, cosmic rays can penetrate even these dense clouds and ionize the particles they interact with. For example, when a cosmic ray particle interacts with a hydrogen atom in a molecular cloud, it can ionize the atom, resulting in the formation of a positively charged hydrogen ion and a free electron.

$$CR + H \rightarrow CR + H^{+} + e^{-} \tag{1.36}$$

The ionization caused by cosmic rays is an important process that influences the chemistry of the environment. It can initiate various chemical reactions and affect the abundance of different species in molecular clouds. In non-relativistic regime protons lose their energy faster than electrons as the mass of protons is very high compared to mass of electrons (protons move slower). The energy loss of proton for one encounter is given by [19],

$$\Delta E = \frac{Z^2 e^4}{8\pi^2 \epsilon_{\odot}^2 b^2 v^2 m_e} \tag{1.37}$$

where,

- Z is the atomic number of target particle,
- m_e is the mass of electron,
- $\epsilon_\odot$ permittivity in free space,
- b is the impact parameter (shortest distance between the CR and target particle),
- v is the velocity of the particle.

In Eq 1.37 it is observed that as the impact parameter and velocity decreases, the energy loss of a proton increases. This phenomenon occurs because when the impact parameter is small and the velocity is low, the proton comes closer to the target particle during the interaction. The impact parameter can be determined either by classical or quantum approaches. In the classical approach, the closest approach is when the electrostatic energy is equal to the maximum energy transfer.

$$b_{\text{min,classic}} = \frac{Ze^2}{8\pi\varepsilon_0 m_e v^2} \tag{1.38}$$

In quantum mechanics, the closest approach is provided based on Heinsenberg Uncertainity principle.

$$b_{\text{min,quantum}} \approx \Delta x \approx \frac{\hbar}{2m_e v} \tag{1.39}$$

The correct b_{min} to use depends upon the physical condition of the problem.

$$\frac{b_{\text{min,quantum}}}{b_{\text{min,classic}}} = \frac{\hbar}{2m_e v} \times \frac{8\pi\varepsilon_0 m_e v^2}{Ze^2} = \frac{1}{z\alpha}\left(\frac{v}{c}\right)^2 = \frac{137v}{zc} \tag{1.40}$$

Thus, for a very high energy particle with v/c >> 0.01, a quantum limit is required and the energy loss is calculated by Beth-Bloch formula [19].

$$\frac{dE}{dx} = \frac{Z^2 e^4 n_e}{4\pi\varepsilon_0^2 v^2 m_e}\left[\ln\left(\frac{2\gamma^2 m_e v^2}{\bar{I}}\right) - \frac{v^2}{c^2}\right] \tag{1.41}$$

where, $\bar{I}$ is the ionisation potential and expressed in the Bohr model relating angular frequency as $\bar{I} = \frac{\hbar\omega_0}{2}$. Finally the coulomb or ionisation loss timescale is given by [4],

$$\tau_c = 7934\text{Myr}\left(\frac{n/10^{-3}}{\gamma/300}(1.168 + 1/75(\ln\frac{\gamma/300}{n/10^{-3}}))^{-1}\right) \tag{1.42}$$

When ionization losses are the dominant factor, the energy spectrum is characterized by N(E) $\propto E^{-(p-1)}$. Thus, the energy spectrum is flatter by one power in E.

1.10.2 Synchrotron and Inverse Compton losses

Non-thermal processes play a significant role in indicating the presence of cosmic rays. One such process involves the energy loss of electrons through synchrotron radiation, which occurs when charged particles move in the magnetic fields. Electrons, in particular, emit synchrotron radiation and have a relatively short radiative lifetime. In contrast, protons do not undergo significant energy loss through synchrotron radiation. This is because the energy loss rate in synchrotron radiation is inversely proportional to the mass of the particles. As protons have a much higher mass compared to electrons, their energy loss rate through this process is considerably lower. Therefore, the detection of synchrotron emission is often indicative of the presence of cosmic ray electrons [19].

The rate at which cosmic ray electrons lose energy is inversely proportional to the Lorentz factor(γ) and square of magnetic field [4].

$$\tau_{rad} = \frac{7720\text{Myr}}{(\gamma/300)[(B/3.25\mu G)^2 + (1+z)^4]} \tag{1.43}$$

where,
z is the redshift.

In the case of a fixed magnetic field strength, the energy loss time for cosmic ray electrons is primarily dependent on their Lorentz factor. High energy particles have shorter energy loss time. For extragalactic sources with a Lorentz factor of around 10^3 and a magnetic field strength of approximately 10μG, the energy loss time is estimated to be on the order of 10^7 to 10^8 years. If synchroton or inverse Compton losses dominate then the spectrum becomes N(E) $\propto E^{-(p+1)}$. The energy spectrum is steeper by one power in E. In inverse Compton process the photons gain energy at the expense of kinetic energy of the electron. In SNR, the same electrons responsible for the synchroton emission visible at X-ray energies can scatter the same photons to $\sim$ 10 Tev energies via Synchroton Self-Compton. Along with Eqn 1.20 the rate of energy loss through inverse Compton is given by [19],

$$(\frac{-dE}{dt})_{IC} = 1 \cdot 10^{-13}(\gamma)^2 + (1+z)^4[J/s] \tag{1.44}$$

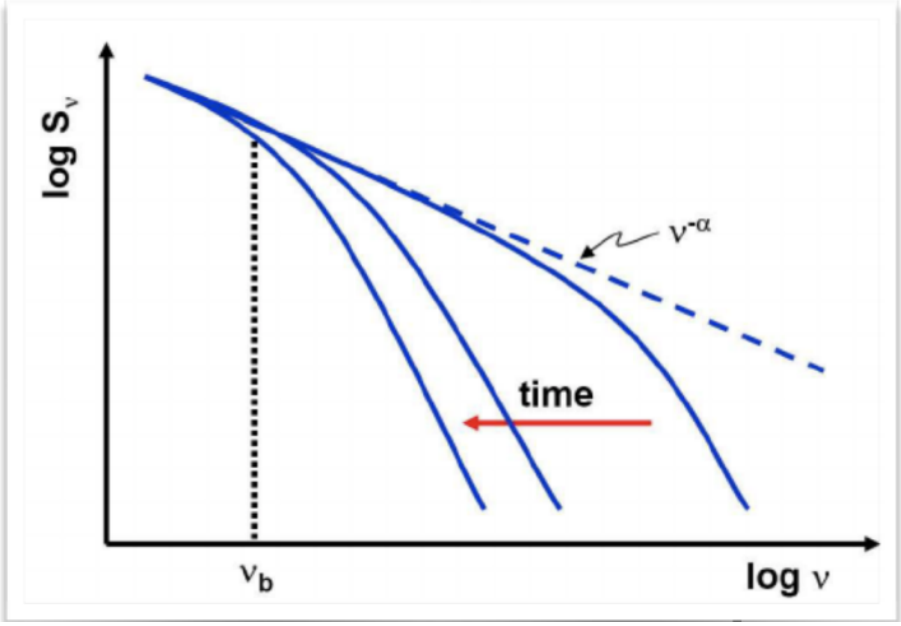

Figure 1.18: Evolution of spectra over time due to synchrotron losses [39].

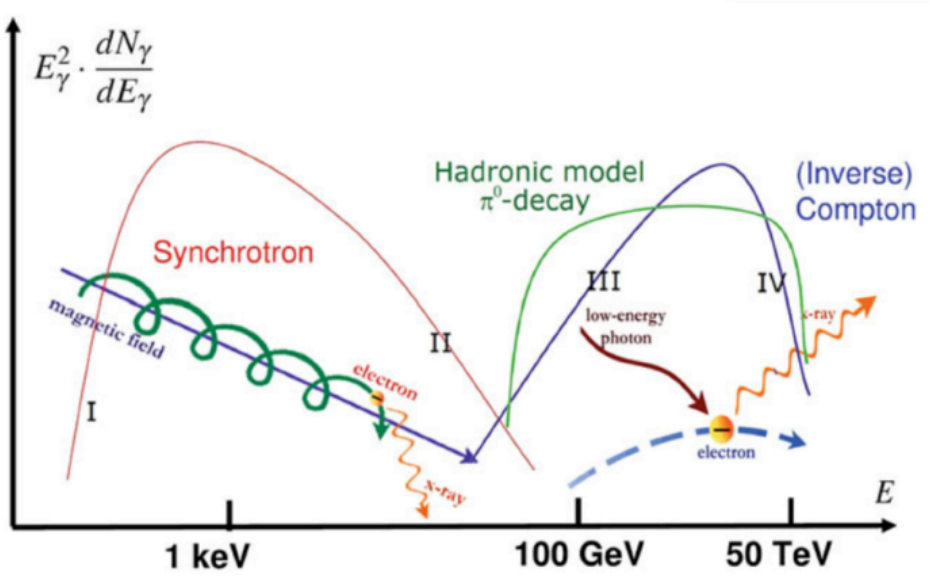

Figure 1.19: Energy vs Flux for different processes in a SN remnant [39].

1.10.3 Adiabatic losses

Other channels of energy loss can be verified during adiabatic processes, specifically during the expansion of a volume of cosmic rays. When electrons are confined within an expanding bubble, they experience adiabatic losses as they perform work to decrease the internal energy (U) of the gas. The amount of energy lost during adiabatic expansion depends on the energy of the particle undergoing expansion as well as the divergence of

its velocity. The energy loss rate for adiabatic process is given by [4],

$$(\frac{-dE}{dt})_{adi} = \frac{-2}{3} \cdot E(\nabla \cdot \vec{v}) \tag{1.45}$$

The adiabatic loss time is calculated by [4],

$$\tau_{adi} = \frac{951\text{Myr}}{\nabla \cdot \vec{v}/10^{-16}} \tag{1.46}$$

An important expression to understand if the gas is compressing or expanding is given by [19],

$$(\frac{d\gamma}{dt})_{adiab} = -3.5 \times 10^{-17}\gamma \frac{\nabla \cdot \mathbf{v}}{[10^{-16}\text{s}]^{-1}} \tag{1.47}$$

From Eq 1.47 the divergence of the vector field, $\nabla \cdot \vec{v} \leq 0$ it indicates that the gas is undergoing compression and it becomes a gain term. Finally unlike ionisation and synchroton losses if adiabatic losses dominate the spectrum is unchanged i.e, N(E) $\propto$ E^{-p} .

1.10.4 Collisional losses

In collisional losses, cosmic ray particles experience inelastic collisions with lightweight atomic nuclei, resulting in the generation of a cascade of secondary particles. These collisions occur over an extremely short distance, characterized by the radius of the nucleus, denoted as $R_{nucleus}$, which is equal to $1.2 \cdot 10^{-15}$ $A^{1/3}$ m, with A representing the mass number of the atom. These interactions occur at energies equal to or greater than GeV. At such high energy levels, the de Broglie wavelength of the incident particles is smaller than the separation between two particles within the nucleus.

When cosmic ray particles undergo inelastic collisions near the "front edge" of a nucleus, a variety of secondary particles such as strange particles or pions can be generated. In the center-of-momentum frame of the proton-nucleon collision, the majority of pions are predominantly emitted in the forward and backward directions. However, they may still possess lateral components of momentum on the order of p $\sim$ 100 - 200 MeV/c. Both the nucleons and pions involved in these collisions carry a significant amount of forward momentum in the laboratory frame. The resulting products of these interactions, including the pions and other particles, exhibit high energies. This high-energy release initiates a cascade or shower of particles, where additional secondary particles are generated as a consequence of the initial collision. These secondary particles possess the capability to initiate subsequent collisions within the same nucleus, thereby setting off a cascade reaction inside the nucleus. The primary product resulting from this process is known as a "spallation" fragment. Spallation, induced by cosmic rays, is a fundamental phenomenon

that occurs when heavy particles interact with cosmic rays while traversing a medium [40].

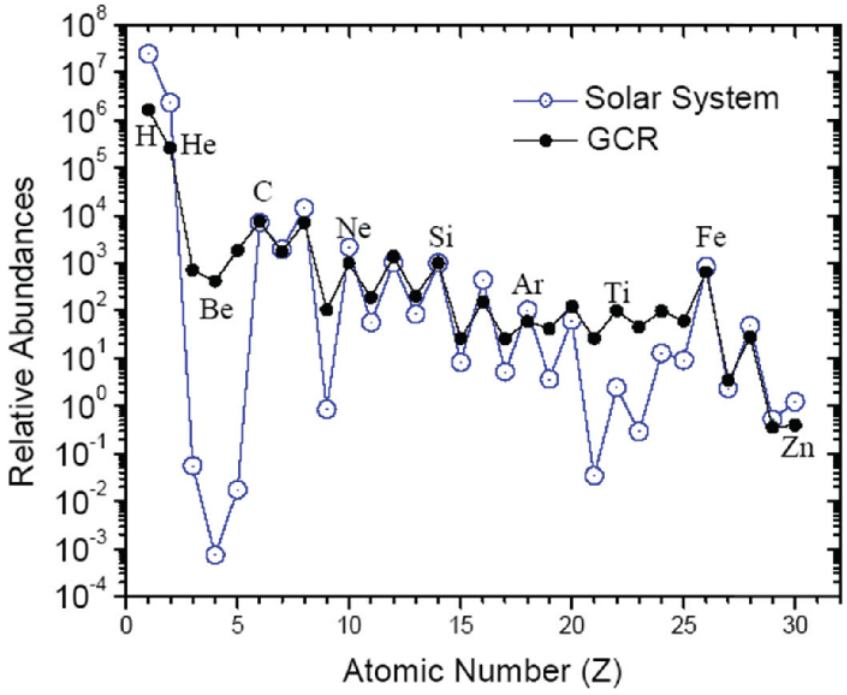

Figure 1.20: Galactic cosmic ray relative abundances compared with the Solar System [21].

The process of spallation by cosmic rays in the ISM is a fundamental mechanism that helps to account for the relative abundances of various heavy nuclei observed in our galaxy. While the majority of cosmic ray elements exhibit abundances similar to those found in the Sun, certain nuclei such as Li, Be, and B are considered to be secondary nuclei formed through the spallation of heavier elements like C and O. Similarly, Mn, V, and Sc are derived from the fragmentation of Fe. These nuclei are commonly referred to as secondary cosmic rays, as they are produced through the process of spallation [19].

1.11 Cosmic ray showers

Primary cosmic rays composed of protons and nuclei initiate a hadronic shower by interacting with the nuclei of the atmosphere after traveling an average distance of one interaction length λ. The hadronic cascade solely depends on λ, which is inversely proportional to the the interaction cross-section (σ) and the number density (n), $\lambda_{\text{cm}} = \frac{1}{n\sigma}$. This equation is usually multiplied by the number density [41]:

$$X[\text{g/cm}^2] = \frac{\rho}{n\sigma} = \frac{Am_p}{\sigma} \tag{1.48}$$

The nuclear interaction length for a nucleus with mass number A multiplied with the mass density is called "grammage" or atmospheric depth. For $\sigma \approx 45$ mb and $\rho \sim 0.1$

kg/m^3, we have $\lambda \sim 1$ m and $X \sim 0.1$ kg/m^2. The secondary hadrons generated in the atmospheric cosmic ray shower, deposit energy through two main mechanisms. Firstly, they interact with the medium and cause ionization or excitation of the surrounding atoms or molecules, leading to the energy deposition. Secondly, these secondary hadrons undergo successive interactions with nuclei present in the medium, resulting in the production of lower energy hadrons. These interactions can yield various types of hadrons, including charged pions, neutral pions , charged kaons ($K^{+/-}$), neutral kaons (K^0), protons, and neutrons. Each of these particles carries a portion of the initial energy of the primary cosmic ray and contributes to the overall energy deposition in the medium during the cosmic ray shower.

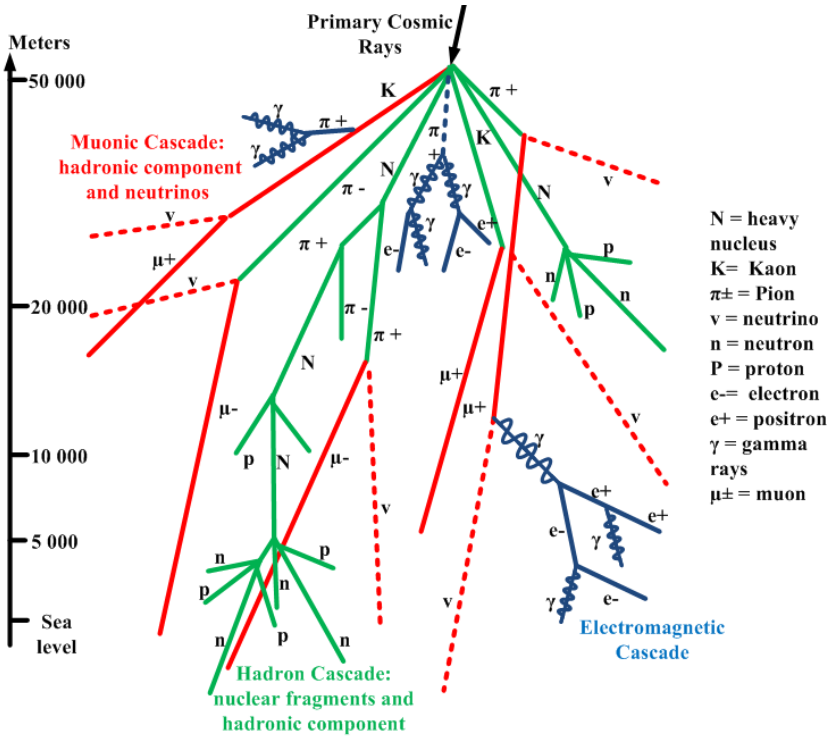

Figure 1.21: Showers of cosmic ray reactions with particles of the atmosphere [42].

Nuclear interactions are very common in Earth's atmosphere as it is one of the most densest environment that cosmic rays enter.

During the cascade of an atmospheric cosmic ray shower, neutral mesons decay into a pair of gamma rays immediately. High-energy photons traverse through matter and each photon can again convert into an electron-positron pair known as pair production. Each electron (or positron) in this pair is capable of emitting energetic photons through bremsstrahlung. Thus, a chain reaction of photon conversions and subsequent pair emission occurs within the cascade. It clearly signifies that along with hadronic shower we also have electromagnetic shower. The electromagnetic cascade persists until the energies of the leptons involved decrease below a critical energy threshold E_c. At this point,

electrons primarily lose their energy through the process of excitation and ionization within the medium [41]. This phenomenon also occurs in the ICM, which is connected to the generation of gamma rays studied in this thesis.

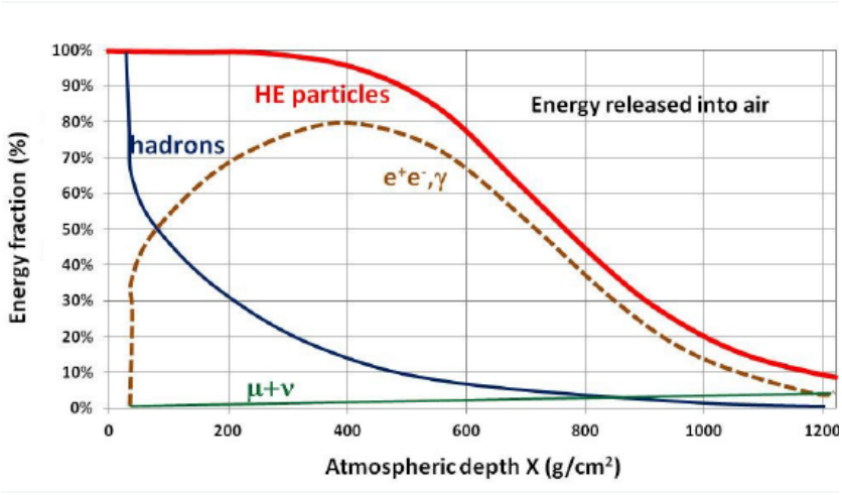

Figure 1.22: Energy fraction remaining with respect to atmospheric depth for various particles following cosmic shower [39].

1.12 Energy loss by high energy cosmic rays

Ultra-high-energy cosmic rays (UHECRs) with energies significantly exceeding 10^{18} eV propagate across cosmological distances ($>> 100Mpc$) and exhibit minimal deflection when encountering extragalactic magnetic fields. These cosmic rays with energies exceeding "the ankle" in the power-law distribution are thought to originate from sources outside our own galaxy. This conclusion is drawn from the observation that these cosmic rays have gyro radii larger than the height of our galaxy. As a result, they must be generated by extra galactic sources rather than originating solely from our galaxy. They have a spectrum $I(E) \propto E^{-3.1}$ which is stepper than that of galactic cosmic rays [43]. Possible sources for UHECRs are proposed based on Hillas criterion. According to the criteria the maximum energy that can be obtained depends upon atomic number of the particle, magnetic field and their gyro radius [19].

$$E_{\max} \approx 10^{21}\mathrm{eV} Zc \left(\frac{R}{1\mathrm{Mpc}}\right)\left(\frac{B}{\mu\mathrm{G}}\right) \tag{1.49}$$

The natural solution that satisfies Hillas criterion are relativistic jets, launched by both GRBs and AGNs. These UHECRs experience energy losses when they propogate through space by several mechanisms:

- When UHECRs travel through cosmic voids, they can undergo pion-production interactions with the photons of the CMB.

- Adiabatic energy losses occur due to the expansion of the Universe. As UHECRs traverse through the expanding space, they experience a decrease in energy.
- Pair production is another energy loss mechanism, resulting in the creation of electron-positron pairs.

1.12.1 Pion-production

The UHECRs possess exceptionally high Lorentz factors, causing the photons of the CMB to have extremely high energies when observed in the rest frame of the cosmic ray. As a result, photo-pion and photo-pair production become viable processes for UHECRs due to the significant energy available in the CMB photons. The different ways in which photon-pion production can take place are [41],

$$\gamma_{\text{CMB}} + p \rightarrow \Delta^+ \rightarrow n + \pi^+ \tag{1.50}$$

$$\gamma_{\text{CMB}} + p \rightarrow \Delta^+ \rightarrow p + \pi^0 \rightarrow p + \gamma + \gamma \tag{1.51}$$

$$\gamma_{\text{CMB}} + p \rightarrow \Delta^+ \rightarrow p + N\pi \tag{1.52}$$

The reactions are mediated by the creation (and quick decay) of Δ^+ baryons.
When a proton is subjected to bombardment by high-energy gamma rays, pions are produced. The threshold for this process is $\epsilon_t = 200\text{MeV}$, and the cross section is $\sigma_{\gamma p} \approx 250\mu\text{b}$. In the cosmic ray reference frame, the energy of the photon is given by $\epsilon = \gamma\langle\epsilon_{\text{CMB}}\rangle\left(1 + \frac{v}{c}\cos\theta\right)$.

For $v \approx c$ and $\cos\theta = 1$, we need to have $\gamma \geq 1.7 \times 10^{11}$ in order to satisfy $\epsilon \geq \epsilon_t$. Such a high Lorentz factor can be produced only at $\text{E} = 5 \times 10^{19}$ eV (after considering full CMB spectrum and angular dependancies) which sets the threshold condition for pion-prodution.

1.12.2 Pair-production

During the propagation in the CMB, electron-positron pairs can be produced through the process [41]:

$$p + \gamma_{\text{CMB}} \rightarrow p + e^- + e^+ \tag{1.53}$$

The threshold for pair production is approximately 200 times lower than that of the photo-pion mechanism. Therefore, it becomes significant even for gamma-ray energies on the order of $\gamma \sim 10^9$ for cosmic rays (specifically, for protons). This process removes only $\Delta E/E \sim 10^{-3}$ per scatter, hence the loss timescale is longer than pion-production.

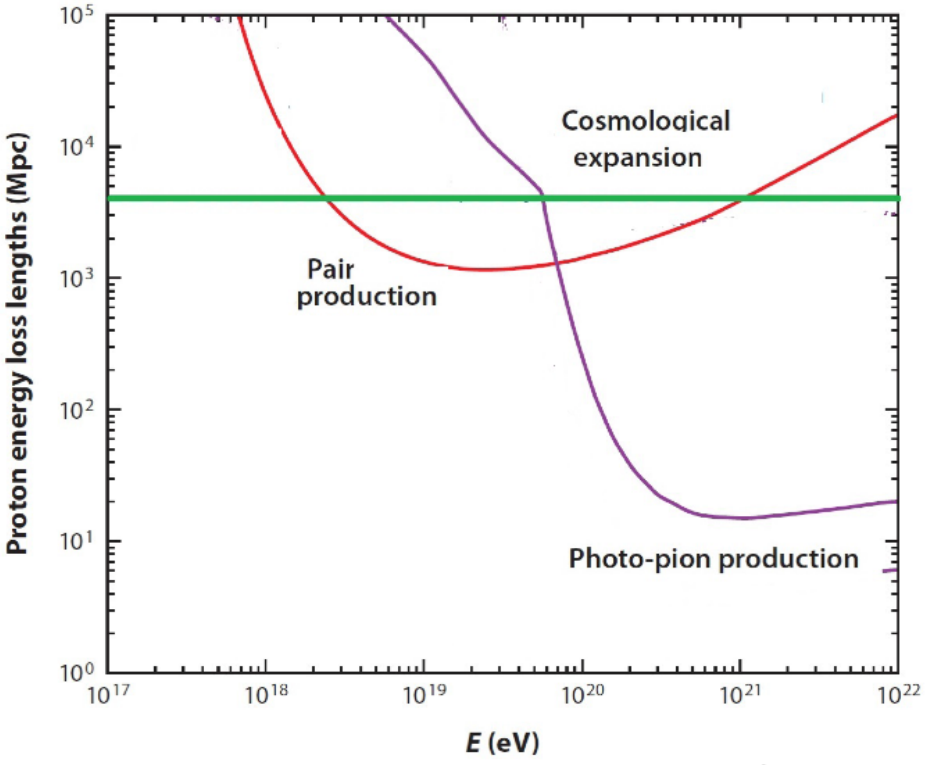

Figure 1.23: Comparison of the relative contributions of the three loss processes for UHECRs as a function of energy (for a proton) [19].

1.12.3 GZK cut off

The number density of CMB photons is given by, $n_\gamma \approx 500/\text{cm}^3 = 5 \times 10^8/\text{m}^3$. The mean free path for a single scattering is $\lambda = (n_\gamma \sigma_{\gamma p})^{-1} \approx 10^{23} \approx 3$ Mpc [19].

From the above data we can calculate the maximum distance an UHECR can travel before losing all of it's energy. The fractional energy loss during every collision for an UHECR is $\Delta E/E \sim \frac{1}{10}\ (m_\pi/m_\gamma)$, which means UHECR proton entirely loses it's total energy in ~ 10 scatters in a distance of L ~ 30 Mpc or after propagation time of $\sim 10^8$ years. This limitation is known as GZK cut-off. As a consequence, UHECRs originating from distances beyond the GZK cutoff are unable to reach us. For UHECR protons, the cutoff distance is approximately 30 Mpc. Heavier nuclei have even larger cutoff distances, for example, iron has a cutoff distance of 80 Mpc [19].

1.13 Hadronic gamma ray emission of cosmic ray protons

This thesis centers around an in-depth exploration of hadronic gamma-rays originating from galaxy clusters and its constraints. To comprehensively comprehend the constraints

associated with gamma-ray emissions within these clusters, it is important to understand the mechanisms governing the production of gamma-rays via hadronic emission. Two primary processes contribute to the generation of gamma-rays: hadronic and leptonic emissions. In the context of leptonic emission, high-energy electrons drive the process through inverse Compton scattering of synchrotron radiation, ultimately yielding gamma-ray emissions. Hadronic emission involves a distinct process wherein cosmic ray protons engage in inelastic collisions where,

$$p + p \rightarrow \pi^{+/-} + \pi^0 + \text{anything} \tag{1.54}$$

$$\pi^{+/-} \rightarrow \mu^{+/-} + \nu_\mu \tag{1.55}$$

$$\mu^{+/-} \rightarrow e^{+/-} + \bar{\nu}_\mu + \nu_e \tag{1.56}$$

$$\pi^0 \rightarrow 2\gamma \tag{1.57}$$

In hadronic collisions, both charged and neutral pions are produced. The charged pions subsequently undergo decay, resulting in the formation of muons and muonic neutrinos. These muons then further decay into electrons, anti-muon neutrinos, and electronic neutrinos. On the other hand, the neutral pions, formed during the hadronic collision, are unstable and have an extremely short lifetime of 8.4×10^{-17} s. They rapidly decay into two gamma rays. Approximately in one-third of the systems, the predicted gamma rays from the neutral pion decay should exceed the observation limits of the FERMI telescope. This thesis thoroughly investigates this aspect, analyzing whether any limitations exist in the generation of gamma-rays within galaxy clusters.

1.14 Constraints on gamma ray emission in clusters

Despite successful gamma-ray detections from individual sources within galaxy clusters, such as radio galaxies NGC 1275, IC 310 in the Perseus cluster and M87 in the Virgo cluster, the search for the first direct detection of high-energy gamma rays specifically from the ICM of galaxy clusters is still ongoing Ackermann et al (2014). As discussed in the earlier sections, the identification and study of gamma rays induced by cosmic rays within galaxy clusters hold significant importance. They provide valuable insights into the physical heating mechanisms associated with the feedback from AGNs as well as into CR re-acceleration processes.

Radio observations provide evidence of the presence of numerous cosmic ray electrons within galaxy clusters. However, the absence of detectable gamma rays raises uncertainties regarding the presence of cosmic ray protons. The acceleration of relativistic protons is expected to be equally, if not much more efficient than that of electrons in accretion and merger shocks. As mentioned in the earlier Section 1.13 gamma rays are anticipated

to be generated through inverse compton scattering by cosmic ray electrons and through inelastic proton-proton collisions by cosmic ray protons. The upscattering of secondary leptons are considered to be subdominant when compared to gamma rays produced by decaying neutral pions in the ICM [44]. This factor stands as a motive to focus the thesis exclusively on the study of hadronic emission and its constraints. Recently gamma-ray emission has been reported in the Coma cluster using the Fermi-LAT instrument. The reasons behind the lack of gamma-ray detection in other clusters remain unclear.

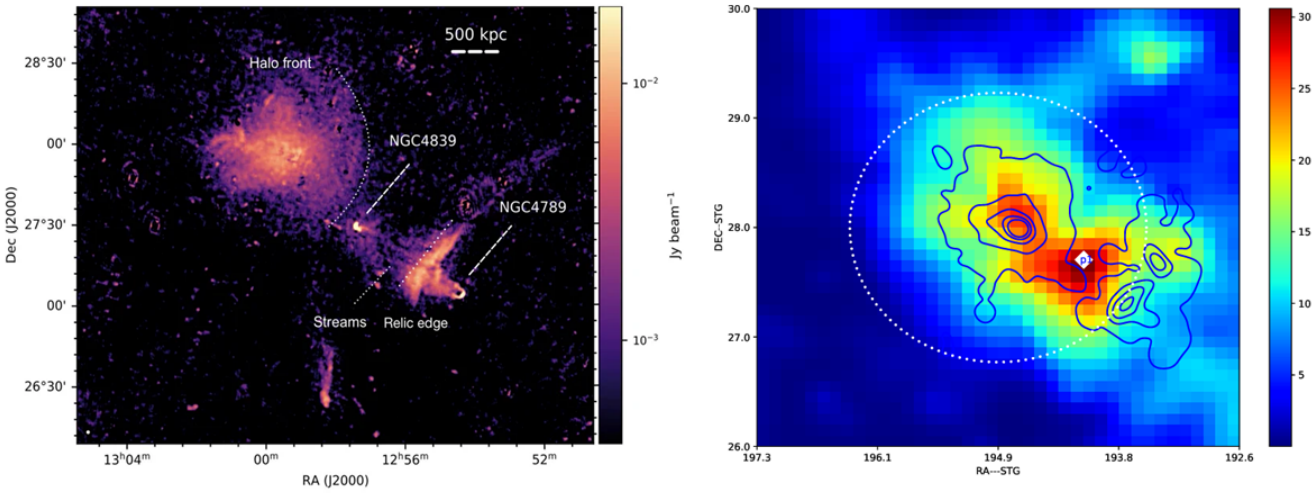

Figure 1.24: On the left the Coma cluster in radio (LOFAR [45]), on the right in gamma rays (FERMI [46]).

Considering the significantly long radiative lifetime of protons, which exceeds several billions of years, and their relatively slow diffusion into the ICM, galaxy clusters act as an efficient reservoir for the storage of cosmic ray protons. The accumulation of cosmic rays within clusters over cosmological timescale implies the presence of a considerable population of relativistic particles within the ICM [4].

One of the deepest upper limit of gamma ray flux from clusters is given by FERMI-LAT obeservations. The analysis of the upper limit is described in detail in Ackermann et al (2014). It was analysed utilizing a data set spanning 4 years of all-sky observations from the Fermi-LAT detector to investigate high-energy gamma-ray emission from 50 X-ray luminous galaxy clusters. Later analysis with longer integrations by FERMI have only slightly lowered these limits. The analysis focused on determining the upper limit of the flux and classifying the clusters. The study specifically considered hadronically induced gamma rays originating from the ICM. To constrain the normalization of a common scale factor among the clusters, which is expected to describe the gamma-ray luminosity of the ICM, a joint likelihood analysis was employed. By performing this analysis and combining the data from multiple clusters, the potential gamma-ray emission from the ICM was understood and constraints on the scale factor that characterizes

the gamma-ray luminosity in relation to the clusters' properties were established.

In Figure 1.25 there are two cases, contrasting the individually derived gamma - ray flux limits for extended emission from those derived when assuming the cluster emission to be point-like. These upper limits were derived to establish boundaries on the gamma-ray flux and provide insights into the behavior of cosmic rays within the studied system. In Fig 1.26, the upper limits of individual gamma-ray flux for two distinct cosmic ray profiles were compared. The first profile, characterized by a constant X_{CR} (the ratio of CR pressure to thermal pressure), corresponds to the ICM model. The second profile represents a constant P_{CR} (CR pressure) and is associated with the flat model. The flux limit was also caried for different kinds of clusters like Cool Core cluster, Non-Cool Core cluster (Fig 1.27). Thus, by examining these upper limits and comparing different models and cluster types, we can refine our understanding of gamma-ray flux behavior and its connection to cosmic ray dynamics within diverse cluster environments.

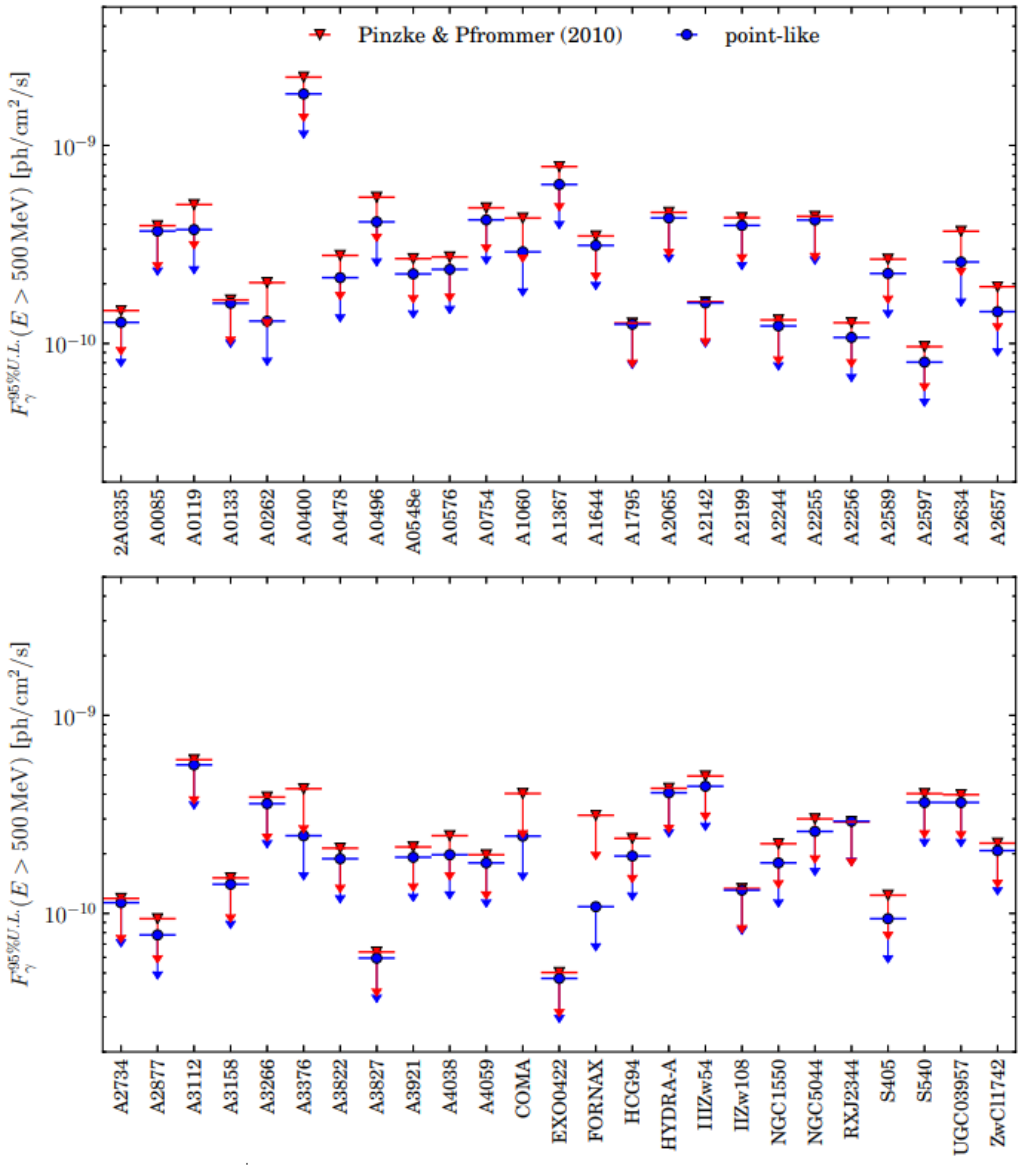

Figure 1.25: Shown are the 95% upper limits on hadronic CR-induced gamma-ray flux for 50 galaxy clusters in this analysis. The individually derived upper limits for both the extended emission (red downward triangle) and assuming the cluster emission to be point-like (blue circle) [2]).

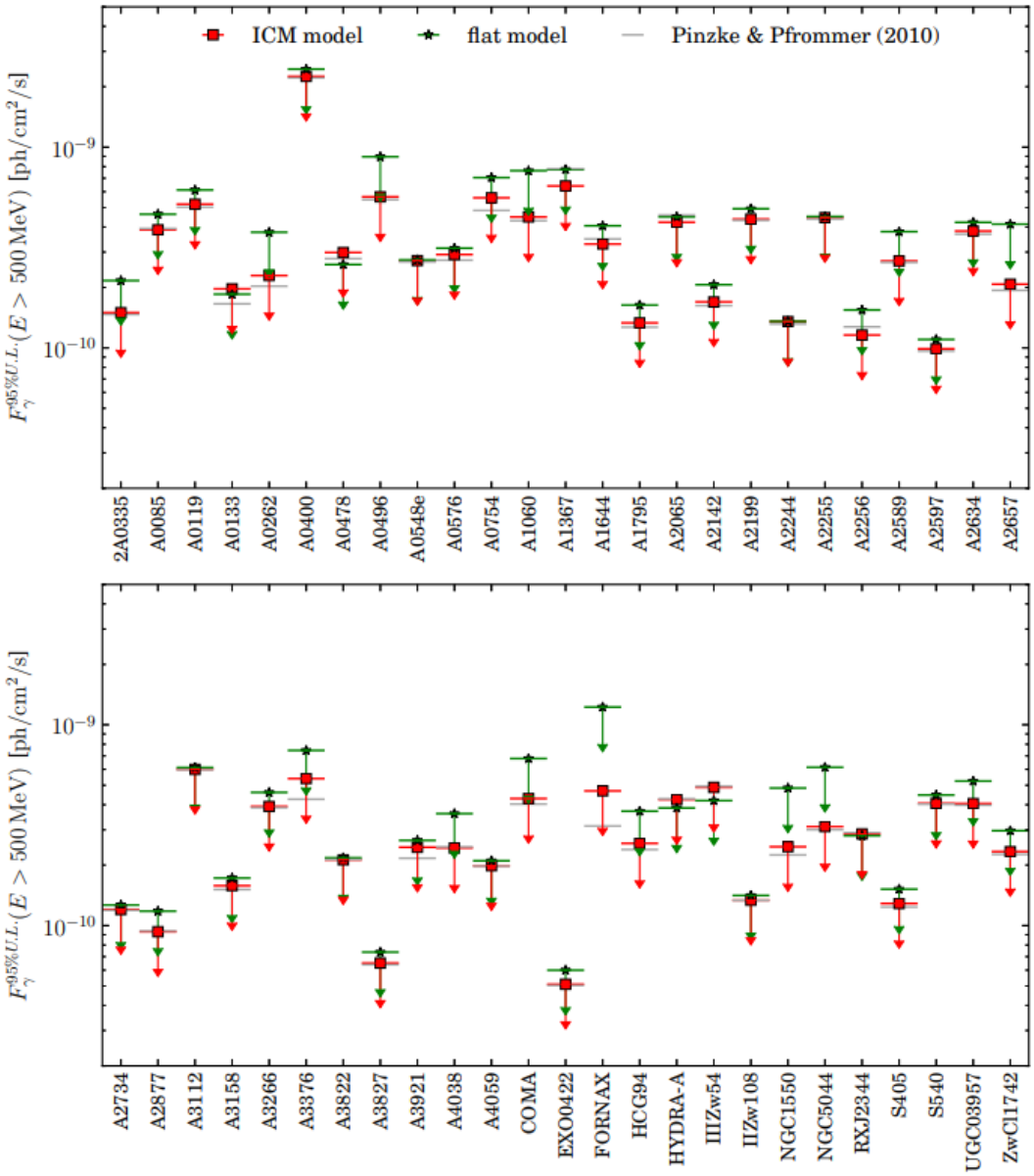

Figure 1.26: Same as fig 1.25 but for spatial CR profiles following a constant X_{CR} profile (CR to thermal pressure ratio) (ICM model, red squares) and a constant P_{CR} profile (flat model, green stars). To allow for an easier comparison, we show the limits from the baseline analysis Fig 1.25 in horizontal gray lines [2]).

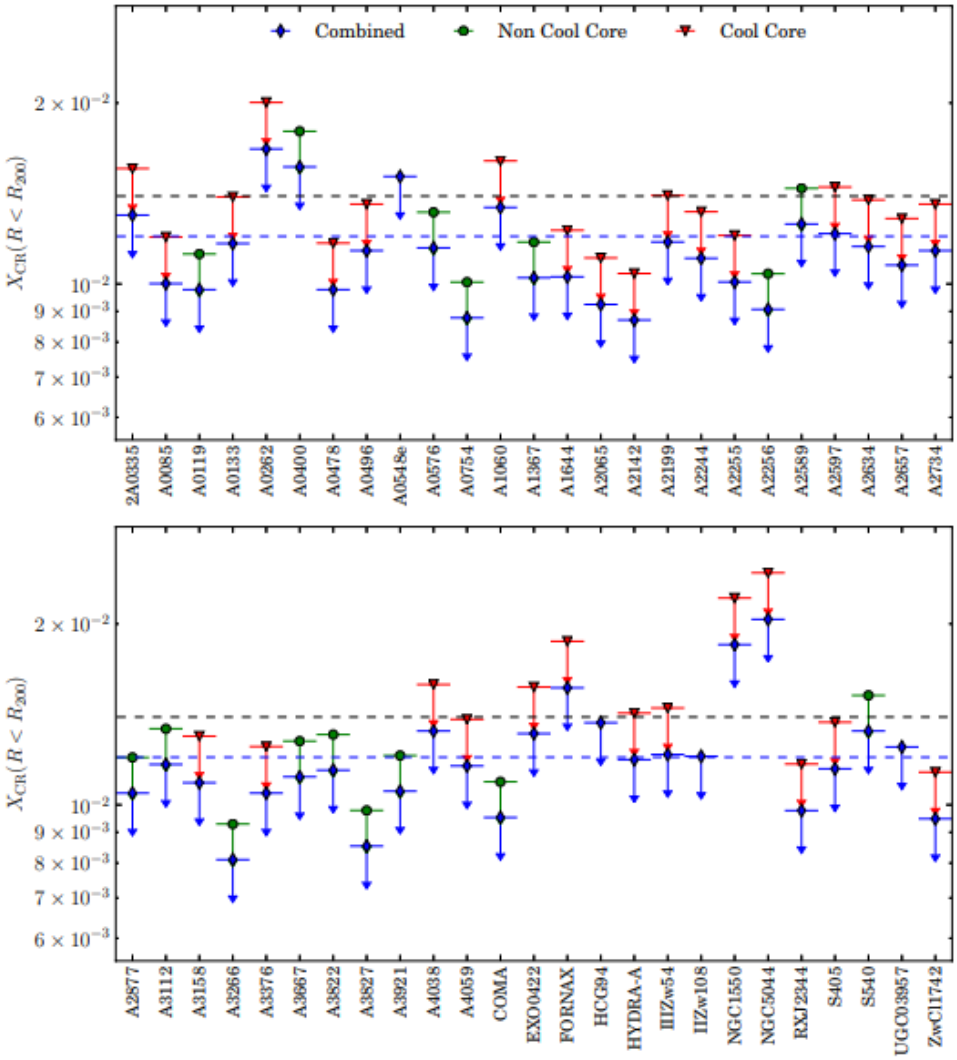

Figure 1.27: Individual 95% upper limits on X_{CR} for 50 galaxy clusters in this analysis assuming the jointly derived scale factor. The analysis for the full sample (blue diamond), CC clusters (red downward triangle), and NCC clusters (green circle). The dashed lines represent the median upper limit for the combined (blue) while the median upper limits for CC and NCC are the same (shown in black) [2]).

Through a comparison between the upper limits and simulated scenarios, we can determine the highest allowable CR budget within the ICM in relation to the thermal gas pressure. FERMI limit constraints the P_{CR}/P_{gas} ratio to be $\leq 1\%$. In many systems, this is lower than what was predicted by early simulations. Therefore, a more refined view of particle acceleration by shocks for example Particle In Cell (PIC) simulations was attempted. In PIC simulation the acceleration efficiency not only depends on shock strength but also on its obliquity (the angle between shock normal and local magnetic field). It was reported that cosmic ray protons are mostly injected by shocks with a parallel alignment, while cosmic ray electrons require a more perpendicular alignment. In case of quasi parallel alignment(M $>$ 2.25) the gamma ray flux didn't drop down significantly and should be still detected by FERMI. Only in case, if we add an additional condition of obliquity such that $\theta < 45°$ (M$>$ 2.25) the predicted gamma ray flux drops

below the FERMI limits (Wittor et al (2020)).

This thesis takes a distinct approach to constrain cosmic ray protons by primarily focusing on the AGN source of these relativistic particles. The study centers around radio jets, which inject relativistic particles into the ICM. Through the utilization of various jet simulations, lagrangian tracers are employed to track the diffusion of cosmic rays from the radio jets into the ICM. One of the simulations involves multiple radio galaxies, resulting in a larger mixing of relativistic particles into the ICM with increased power. By comparing the obtained observational results from the Fermi LAT Satellite, it becomes possible to tentatively constrain the initial conditions of the radio jets. Thus, it constraints the energy content of cosmic rays within the radio jets.

1.14.1 The Neutrinos from the ICM

In addition to gamma rays produced through the decay of unstable pions resulting from hadronic collisions, neutrinos are also generated. As an additional aspect of the study, in this thesis I compare the predicted neutrino production in the cluster to the observations made by the IceCube Neutrino Observatory. Considering that the comparison involves the emission from a single cluster with a few radio galaxies to a diffuse emission, it is expected that the predicted neutrino flux will be considerably lower than what has been detected by IceCube. The neutrino emission analysis conducted in Ha et al. (2020) serves as a reference for a similar study. There the neutrino flux was obtained in a simulated galaxy cluster using a particle-mesh/Eulerian cosmological hydrodynamic code with a ΛCDM cosmology model of baryon density $\Omega_{bm} = 0.044$, dark matter (DM) density $\Omega_{DM} = 0.236$, cosmological constant $\Omega_{\Lambda} = 0.72$, Hubble constant parameter h = 0.7 (Fig 1.28). In this paper, DSA model was used to model the injection of CRs. Initially, the CRp are generated through fresh-injection of DSA at ICM shocks within the simulated cluster samples. Subsequently, under the assumption that these CRp permeate the cluster volume as pre-existing particles, a simplified re-acceleration model is adopted where enhancement in CRp energy resulting from the successive interactions of the ICM plasma with shocks.

According to the results of Ha et al. (2020) the anticipated levels of neutrino flux originating from neighboring clusters are notably lower, by a factor of 10^4, than the neutrino flux observed by the IceCube experiment at an energy of 1 PeV. Moreover, these predicted neutrino fluxes are even more reduced, by approximately 10^6, in comparison to the flux of atmospheric neutrinos within the energy range of ≤ 1 TeV. Due to these significantly diminished predicted fluxes, the prospects of detecting these neutrinos using ground-based facilities like IceCube, Super-Kamiokande, and future Hyper-Kamiokande appear improbable. The suggested explanation for the differences in the neutrino flux

obtained is possibly due to the relatively low efficiency of the DSA model, in addition to the methodologies applied to model the CRp spectrum in Ha et al. (2020) .

Other notable results to be considered include Murase et al. (2008) and Murase et al. (2013) conducted estimations of neutrino emissions arising from CRp generated at AGNs and SNRs within the ICM and galaxies within the cluster. The presence of AGNs can introduce additional neutrino signals compared to cluster shocks. This complexity can arise either due to AGNs emitting neutrinos within the PeV–EeV energy range themselves or by injecting CRs that generate neutrinos independently of cluster shock interactions. According to the findings of Murase et al. (2008), the outcomes suggest that the event rates necessary to detect energies exceeding 0.1 PeV should be between 2-5 yr^{-1} for the different models considered. This inference significantly points to the prospective ability of forthcoming telescopes to find multi-PeV neutrino signals that originate from clusters of galaxies. But more realistic evaluations are needed, considering inhomogeneous structure of accretion and merger shocks, the magnetic field distribution inside and outside the clusters of galaxies. Also, the way CRs are confined can potentially reduce the CR flux while simultaneously leading to an increase in the neutrino flux Murase et al. (2008).

Conversely, Zandanel et al. (2015) and Murase et al (2016) proposed a different perspective, suggesting that the primary sources of CRp contributing significantly to the IceCube neutrino flux with energies below approximately 10 TeV are not due to the ICM shocks or the accretion shocks surrounding clusters. With the simulation parameters and model considered in Zandanel et al. (2015) when the value of α_p exceeds 2, the background levels of gamma-rays and neutrinos in all the scenarios under consideration remain below 1% of the gamma-ray and neutrino fluxes that have been observed by Fermi and IceCube respectively.

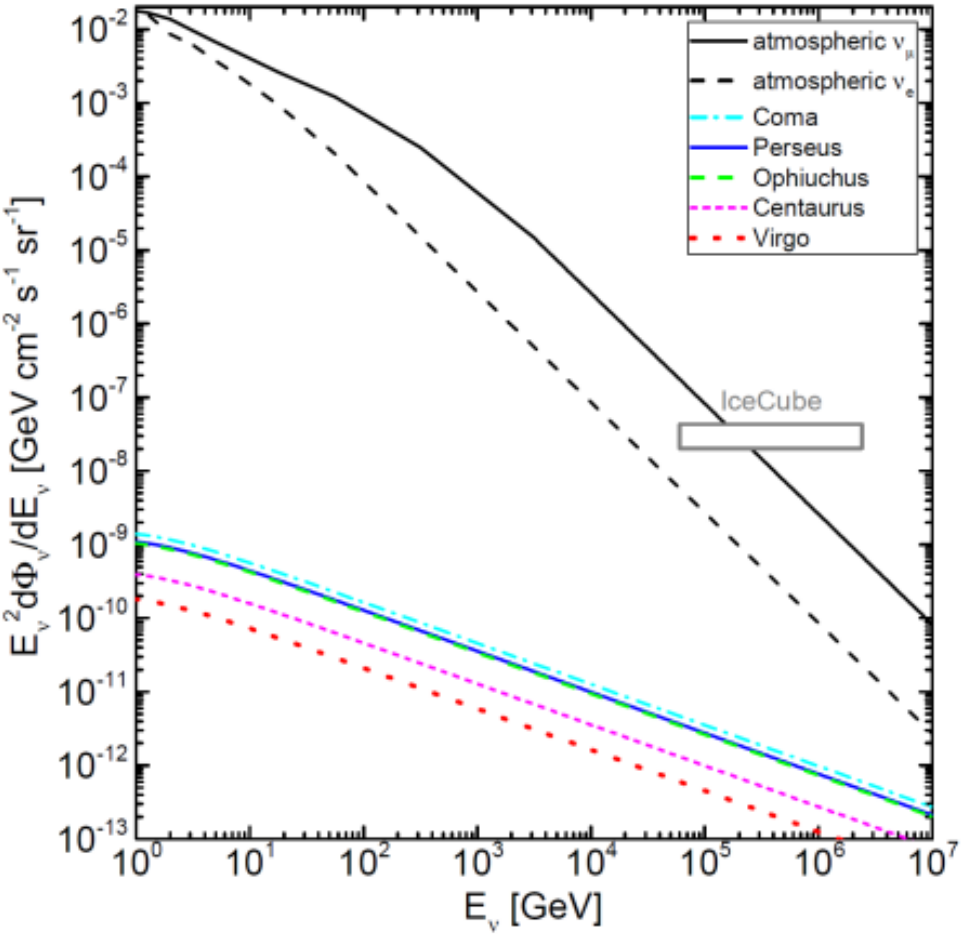

Figure 1.28: Predicted neutrino fluxes from nearby clusters. For the CRp distribution, the model with a spectral index of 2.4 and δ =0.75 is used. The gray box denotes the IceCube flux (Aartsen et al. 2014), and the black solid and dashed lines draw the fluxes of atmospheric muon and electron neutrinos (Richard et al. 2016)[48])

Thus, we have diverse outcome from different simulation parameters. In my thesis, I intend to concentrate producing revised estimates of the neutrino productions from CRp injected by radio galaxies in clusters of galaxies, and re-accelerated by pressure perturbations (shocks and turbulence). This involves investigating how neutrinos will be generated under different conditions, such as a single radio galaxy, single radio galaxy with varying power and multiple radio galaxies. The aim is to potentially yield improved findings for scrutinizing neutrinos and conducting a comparative analysis with the IceCube observations.

Chapter 2

Methodology

The approach of the thesis is explained in this chapter. The methodology is divided into two main parts, as explained below:

The first section explains the simulation Dataset (Section 2.1). In this section, the focus is on studying the simulation used to generate the dataset for analyzing the gamma ray and the neutrino flux. The simulation process and relevant parameters are examined in detail to understand how the dataset was obtained. In the second section mathematical modelling and numerical analysis (section 2.3) is carried out. This section delves into the comprehensive calculation of the gamma ray and the neutrino flux. The methodology for computing these flux values is described in depth, incorporating mathematical models and employing numerical analysis techniques. Furthermore, in Section 3, the obtained flux is critically analyzed in conjunction with the observational data. This analysis aims to provide insights into the flux characteristics, compare the findings with existing observations, and constrain the results within the observational limits.

2.1 Simulation dataset

Single radio galaxy

The mathematical modeling for a single radio galaxy is based on the results obtained from the simulation in Vazza et al (2021) A&A and Vazza et al (2023) A&A with the following conditions:

A cosmological, Adaptive Mesh Refinement (AMR) ENZO [53] simulation based on the magnetohydrodynamical (MHD) solver with a Lax-Friedrichs (LLF) Riemann solver to compute the fluxes in the Piecewise Linear Method (PLM), combined with the Dedner cleaning method [54] implemented by Wang et al (2009). The simulation is initiated from a simple uniform magnetic field at a redshift $z = 50$, with an initial magnetic field

value of $B_0 = 0.1$ nG in each direction.

The simulation encompasses a total volume of $(50\text{Mpc/h})^3$, which is discretized with a root grid consisting of 128^3 cells and dark matter particles. To achieve higher resolution in specific regions of interest, a nested grid approach is adopted. This involves four nested regions, each successively refining the spatial resolution, ultimately converging to a smaller volume of $(4\text{Mpc/h})^3$, where a cluster with a mass of approximately $1.5 \times 10^{14} M_\odot$ forms. In this refined cluster region, the spatial resolution is uniform, set at $\Delta x = 24.4$kpc/h. Furthermore, during the simulation runtime, two additional levels of mesh refinement are implemented using a local gas/dark matter overdensity criterion, specifically $\Delta\rho/\rho \geq 3$. This adaptive refinement strategy allows the simulation to reach a maximum resolution of about $\sim$ 6kpc/h, equivalent to $\sim$ 8.86kpc. Consequently, due to the nested grid approach, the mass resolution for dark matter in the cluster formation region is $M_{DM} = 2.82 \times 10^6\ M_\odot$ per dark matter particle for the highest resolution particles utilized since the start of the simulation.

2.1.1 AGN and radio jets

All the simulations presented in this study are non-radiative and differ only in the feedback power of AGN bursts. The injection of jets and relativistic electrons in this simulation set occurs at redshift z = 0.5. Radiative cooling is neglected in these simulations, and there is no self-regulating mechanism to switch the feedback cycle on and off. The primary objective of the simulations is to study the interplay between thermal and magnetic feedback mechanisms around a SMBH. The SMBH is situated at redshift z = 0.5 and is positioned at the center of mass of a galaxy group with a mass of approximately $\sim 10^{14} M_\odot$. To govern the SMBH's accretion of matter from the surrounding cells, the Bondi-Hoyle formalism is employed.:

$$\dot{M}_{\rm BH} = \frac{4\pi\alpha_B G^2 M_{\rm BH}^2 \rho}{c_s^3}, \tag{2.1}$$

where $M_{\rm BH}$ is the mass of the SMBH, ρ is the surrounding gas density, α_B is a dimensionless factor, G is the gravitational constant, and c_s is the sound speed. For different values of α_B we have different power being produced.

Due to the limited resolution achievable and the absence of radiative cooling in the simulations, a boost factor denoted as α_B is introduced. This boost factor is intended to account for clumpy accretion, which cannot be fully resolved due to the finite spatial resolution in this method. By incorporating the α_B factor, the simulations aim to capture the effects of clumpiness in the accretion process, which would otherwise be challenging to represent accurately at the available resolution level.

Table 2.1: Main jet parameters for the Initial Run A as a function of the assumed α_B (boost factor) in the Bondi accretion mode Vazza et al (2021) A&A.

Parameter	Run A
$z_{\rm jet}$	0.5
$M_{\rm BH}$ [M]	10^9
$\alpha_{\rm B}$	10
$\dot{M}_{\rm BH}$ [M/yr]	1.0×10^{-7}
$t_{\rm jet}$ [Myr]	10
$L_{\rm BH}$ [erg/s]	1.7×10^{45}
$E_{\rm kin,jet}$ [erg]	2.6×10^{56}
$E_{\rm th,jet}$ [erg]	1.2×10^{57}
$E_{\rm mag,jet}$ [erg]	1.6×10^{56}
$B_{\rm av,jet}$ [μG]	1.4
$B_{\rm max,jet}$ [μG]	3.9
$v_{\rm av,jet}$ [km/s]	630

Initially, the simulation considers the boost factor α_B to be 10, and the parameters mentioned in Table 2.1 are used. In this Run the SMBH releases thermal and magnetic energy feedback for 10 Myr [4]. To gain a deeper understanding of the impact of the boost factor and different jet powers, a second set of re-simulation explored five different sets of α_B values: 1, 3, 10, 30, and 50. These variations are studied with a jet injection phase of 32 Myr. At the beginning of the simulation, the jets are composed

Table 2.2: Main jet parameters for the runs as a function of the assumed α_B (boost factor) in the Bondi accretion mode Vazza et al (2023) A&A.

Parameter	Run					Run 0
	B	C	D	E	F	
α_B	1	3	10	30	50	0
P_j [erg/s]	3×10^{43}	9×10^{43}	3×10^{44}	9×10^{44}	1.5×10^{45}	0
$\frac{\dot{M}_{\rm BH}}{\dot{M}_{\rm Edd}}$	0.002	0.006	0.02	0.06	0.1	0
$B_{av,j}$ [μG]	28.6	70.1	66.4	70.4	41.5	0
$T_{av,j}$ [K]	1.5×10^7	3.6×10^7	1.8×10^8	4.3×10^8	5.8×10^8	0
$v_{av,j}$ [km/s]	260	1754	2750	3888	4215	0
$v_{max,j}$ [km/s]	424	2567	4355	10286	7943	0
N_{CRe}	2.7×10^{64}	3.9×10^{64}	6.7×10^{64}	9.9×10^{64}	1.2×10^{65}	0

of thermal and magnetic energy exclusively. Subsequently, around 32 Myr after the injection, a rapid injection phase, the combined thermal and magnetic pressure results in the emergence of strong outflows. To prevent any interference with the dynamics of the jets, the tracers are incorporated during the post-processing stage. In the simulation, we add approximately 10^4 to 10^5 tracers. In all simulations, we observe that after the injection phase lasting approximately 32 Myr, the kinetic, thermal, and magnetic energy

within the jet region are very close to equality, with the energy components satisfying $E_{th} \sim E_B \sim E_{kin} \sim E_{jet}/3$. In reality, the cosmic-ray component is expected to play a significant role in the internal pressure of radio jets embedded in clusters [56]. However, in this simulation, we track cosmic-ray particles as a passive fluid, with no contribution to the dynamical pressure. It should be noted that in all the runs the jet orientation remains the same and in Vazza et al (2023) A&A it was proved that jet orientation does not have any impact on the long term evolution of the ICM.

The SMBH feedback is applied at each root-grid timestep, which is $\Delta t \approx 32$ Myr at the epoch of activation ($z = 0.5$). The corresponding values of total power released by both jets, $P_j = \epsilon_r \epsilon_{BH} \dot{M}_{\rm BH} c^2$, are given in Table 2.2. Due to the variations of α_B the power ranges from 3×10^{43} erg/s to 1.5×10^{45} erg/s. These values are compatible with the range typically inferred from the modeling of FRI radio galaxies in clusters and groups and are also within the power range that single sources in clusters can produce in multiple events [57].

2.1.2 Lagrangian tracer particles

The passive Lagrangian tracers used to simulate electron and proton spectra were injected only once in each run. The Lagrangian code CRaTer was used to follow the spatial evolution of the cosmic-ray proton and electron in the runs. In post-processing, $10^4 \sim 10^5$ particles in the jet region at $z = 0.5$ with a mass resolution $m_{\rm trac} = 5 \times 10^5 M_\odot$ were injected, and evolved them using all snapshots of the simulation for ~ 100 timesteps. The various grid quantities like density and velocity, are assigned to the tracers using a cloud-in-cell (CIC) interpolation method.

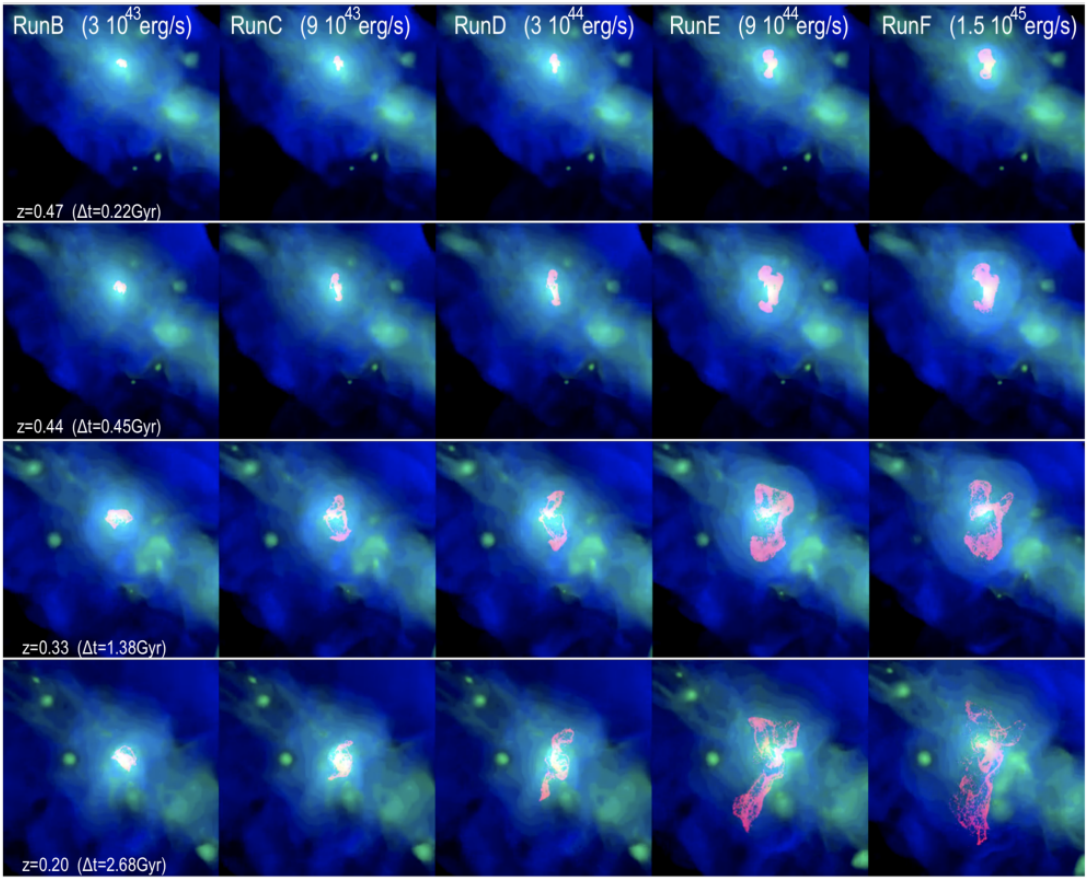

Figure 2.1: RGB rendering of the evolution of thermal gas and passive tracers (marking relativistic electrons/protons injected by jets) in the runs. The red colour marks the density of passive tracers, the blue the gas temperature and the green the X-ray emission. Each panel has a side of 5.5 Mpc (comoving) [3].

2.2 Multiple radio galaxies

In my thesis, I explore not only single radio galaxies but also the effects of multiple radio galaxies and establish constraints on the cosmic ray energy content associated with these multiple radio galaxies. The mathematical modeling of multiple radio galaxies is based on the results obtained from the simulation in Vazza et al (2023) Galaxies, with the following conditions:

Multiple radio galaxies follows the same principles and parameters as those used for a single radio galaxy. In both cases, we inject thermal and magnetic energy into the jets, and shortly after the injection phase, the thermal and magnetic pressure drive powerful outflows. The Lagrangian tracers, which simulate the electron and proton spectra, are injected only once during the epoch when jets from the radio galaxies are released.The bolometric luminosity of each SMBH is given by the standard formula $L_{BH} = \epsilon_r \dot{M}_{\rm BH} c^2$, where $\epsilon_r = 0.1$ is the radiative efficiency of the SMBH. This is used to compute the jet

power released in the feedback stage (which only lasts, by construction, one root grid timestep, i.e., $\sim$ 32 Myr) as $P_j = \epsilon_r \epsilon_{BH} \dot{M}_{\rm BH} c^2$, where ϵ_{BH} is the factor that converts the bolometric luminosity to the thermal feedback energy ($\epsilon_{BH} = 0.05$).

The spatial distribution of radio galaxies within the model is a critical factor that significantly influences the trend of gamma-ray flux produced. The model comprises one dominant and powerful radio galaxy (A) situated at the central region of the cluster, accompanied by four additional radio galaxies positioned in the peripheral region (Fig 2.3). During the initial phase (z = 0.5 $\sim$ 0.4), it is primarily the central powerful radio galaxy that transports tracers into the ICM. The power generated by the jets is not sufficient to propel the tracers to far distances. Instead, they accumulate within bubbles created by the activity of each radio galaxy and subsequently diffuse into the surrounding ICM.

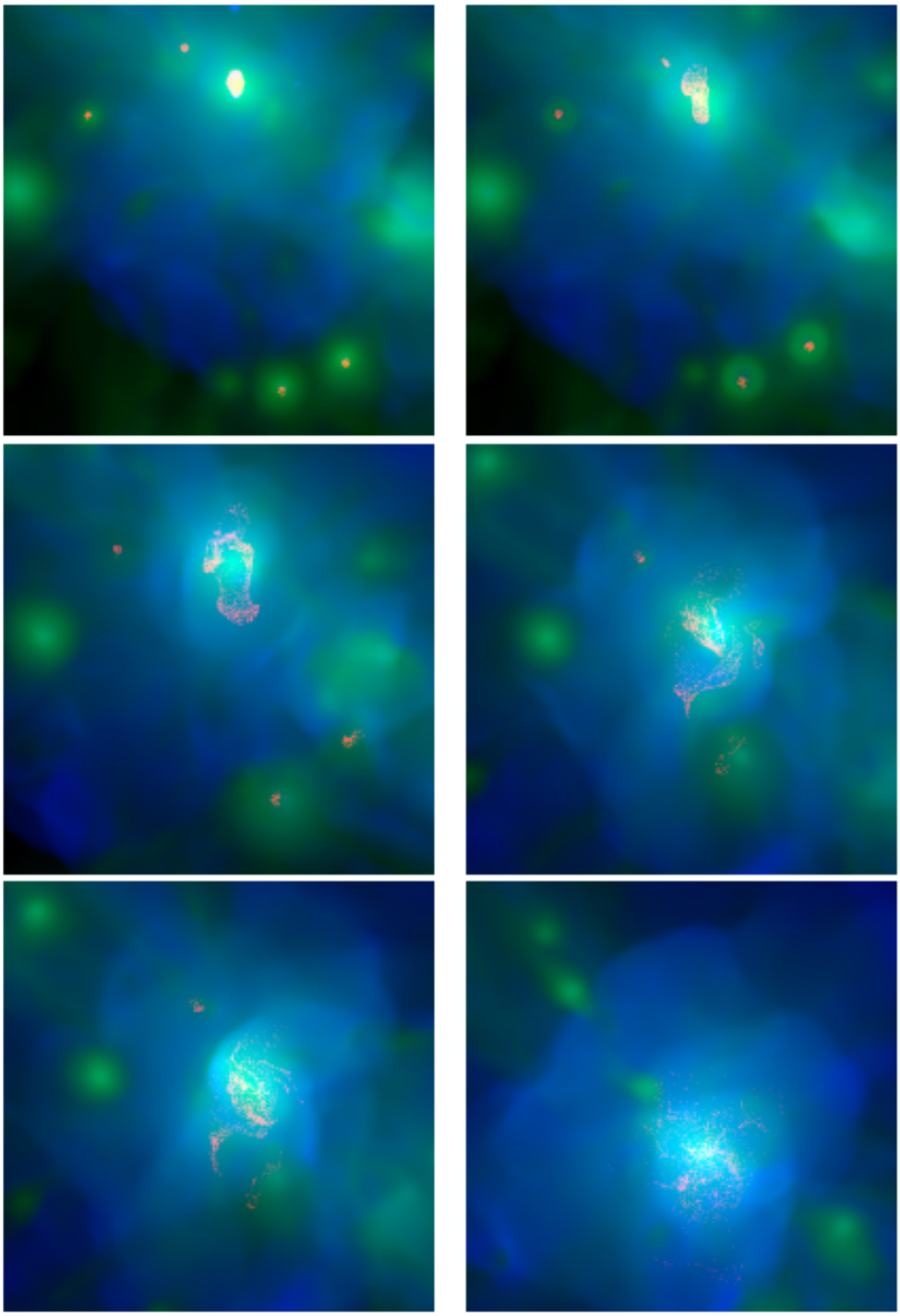

Figure 2.2: Red-green-blue composite images showing the evolution of simulated cluster of galaxies, and of the location of electron tracers injected by the simulated (5) radio galaxies. Each image is 5×5 Mpc^2 across. They show the mass-weighted gas temperature projected along the full line of sight (blue), the projected gas density (green) and the location of the electron tracer, regardless of energy (red). From the top left to the lower right panel, the redshifts are z = 0.493, 0.452, 0.382, 0.201, 0.102, and 0.032 [6].

By properly modelling the synchroton radiative emission for the injected relativistic electrons, Vazza et al (2023) Galaxies showed that following the initial intense phase of jet emission, only a small amount of radiation from the injected electrons is observable at

Table 2.3: Main parameters of SMBH and jet/radio power associated with the jets they emit Vazza et al (2023) Galaxies.

ID	M_{BH} $[M_\odot]$	$\frac{\dot{M}_{\mathbf{BH}}}{\dot{M}_{\mathbf{Edd}}}$	P_j	L_{140} **ergs/s/Hz**
A	8.7×10^8	0.0026	1.4×10^{43}	3.2×10^{32}
B	3.5×10^7	0.0004	1×10^{41}	1.6×10^{31}
C	1.4×10^7	0.0004	1.1×10^{40}	5.3×10^{30}
D	1.3×10^7	0.0007	1.3×10^{39}	2.9×10^{31}
E	8.1×10^8	0.0004	7.1×10^{38}	1.9×10^{31}

radio frequencies. The visible emission is primarily from the elongated remnants of the jet lobes. These remnants have started to blend and mix within the innermost cluster atmosphere.

The observable structures are predominantly filamentary and patchy, with lengths of up to 500 kpc, until z = 0.38. After this period, there is no significant detection of radio emission. This is because of the well known fact that the lifetime of cosmic ray electron is around 10^8 years. However, "fossil" electrons, continue to mix and disperse. At later stages e.g., z $\sim$ 0.37, 0.26, 0.21 some patches of electrons that encounter shock waves or turbulence get re-accelerated and become visible again Fig 2.4. These events are often triggered by accretion of substructures. These accretion events can release pairs of weak (M $\leq$ 3) shock waves and induce new subsonic turbulence in the central region of the main cluster. This great significance due to the predominant role of turbulent and shock re-acceleration processes in one of the cosmic ray evolution model studied in the upcoming section of the thesis. For this thesis, I have analysed the new simulated spectra of cosmic ray protons evolved onboard of the same tracers, in all simulations presented above, which were so far used only to study cosmic ray electrons instead.

CR protons are initially assumed to be in equality with magnetic field energy in jets, $E_{CRp} = E_B$. Spectra are then evolved under the effect of ionisation and coulomb losses, adiabatic changes (Np1 model) and also including the re-acceleration by shocks (Fermi I) and turbulence (Fermi II) following the model by Brunetti & Vazza et al (2020).

From the simulation, the spectra of cosmic ray protons is being evolved and further analysis are carried out. In the case of multiple radio galaxies, a higher number of tracers are transported into the ICM compared to a single radio galaxy simulation. However, apart from this difference, there are overall similarities between the two simulations. Both simulations involve the evolution of Lagrangian tracers and are subjected to two different models. In the first model (Np1), the jets directly transport the tracers into the ICM without any additional processes. In contrast, the second model (Np2) incorporates re-acceleration effects due to shocks and turbulence. This means that in the second

model, some of the tracers experience re-acceleration when they encounter shock waves or turbulence, leading to additional emission and to the flatenning of CR spectra.

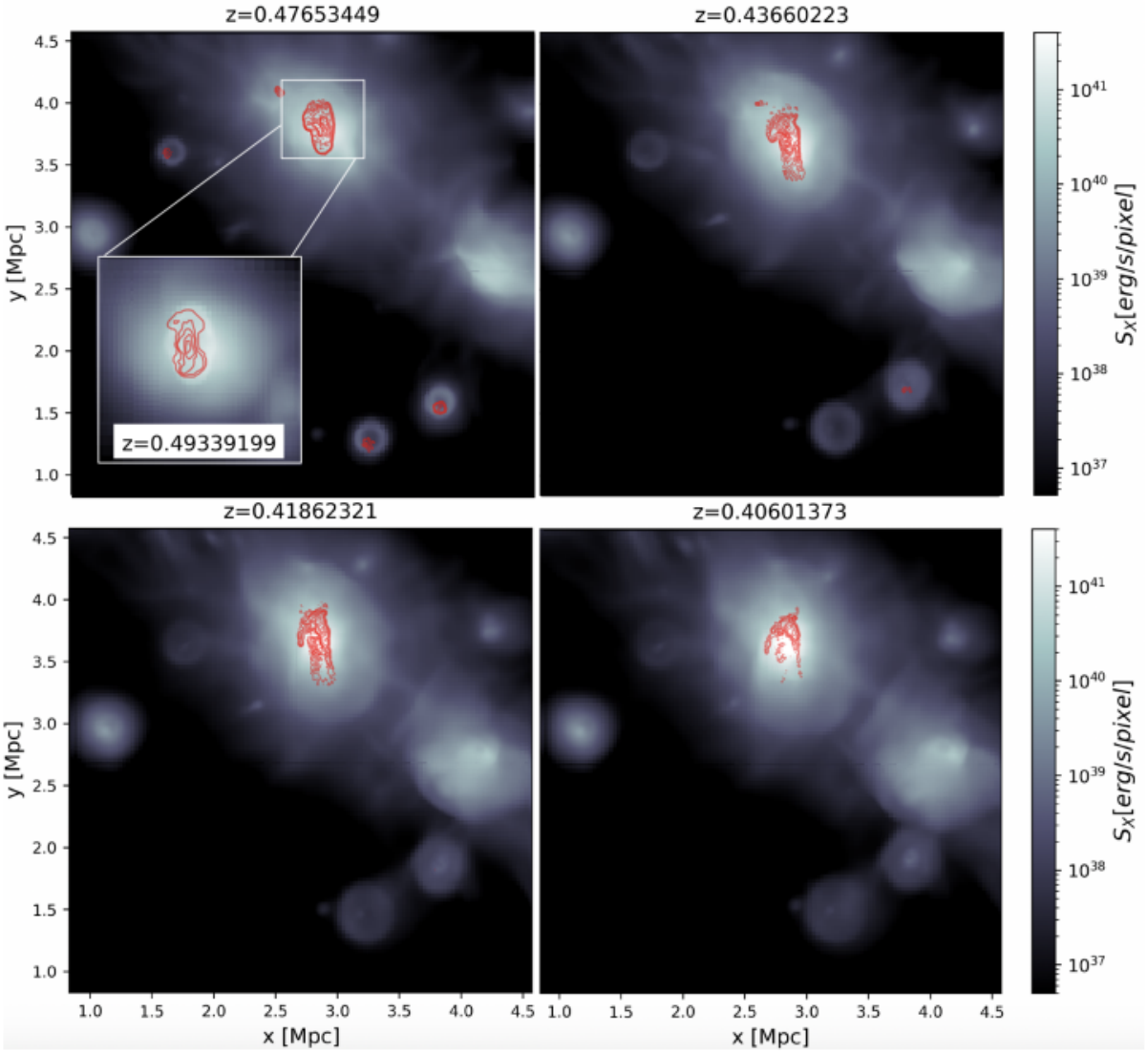

Figure 2.3: Evolution of the X-ray surface brightness (grey colours) and of the detectable radio emission at 50 MHz with LOFAR LBA for all electrons seeded by radio jets at z = 0.5 and later re-accelerated by shocks and turbulence [6].

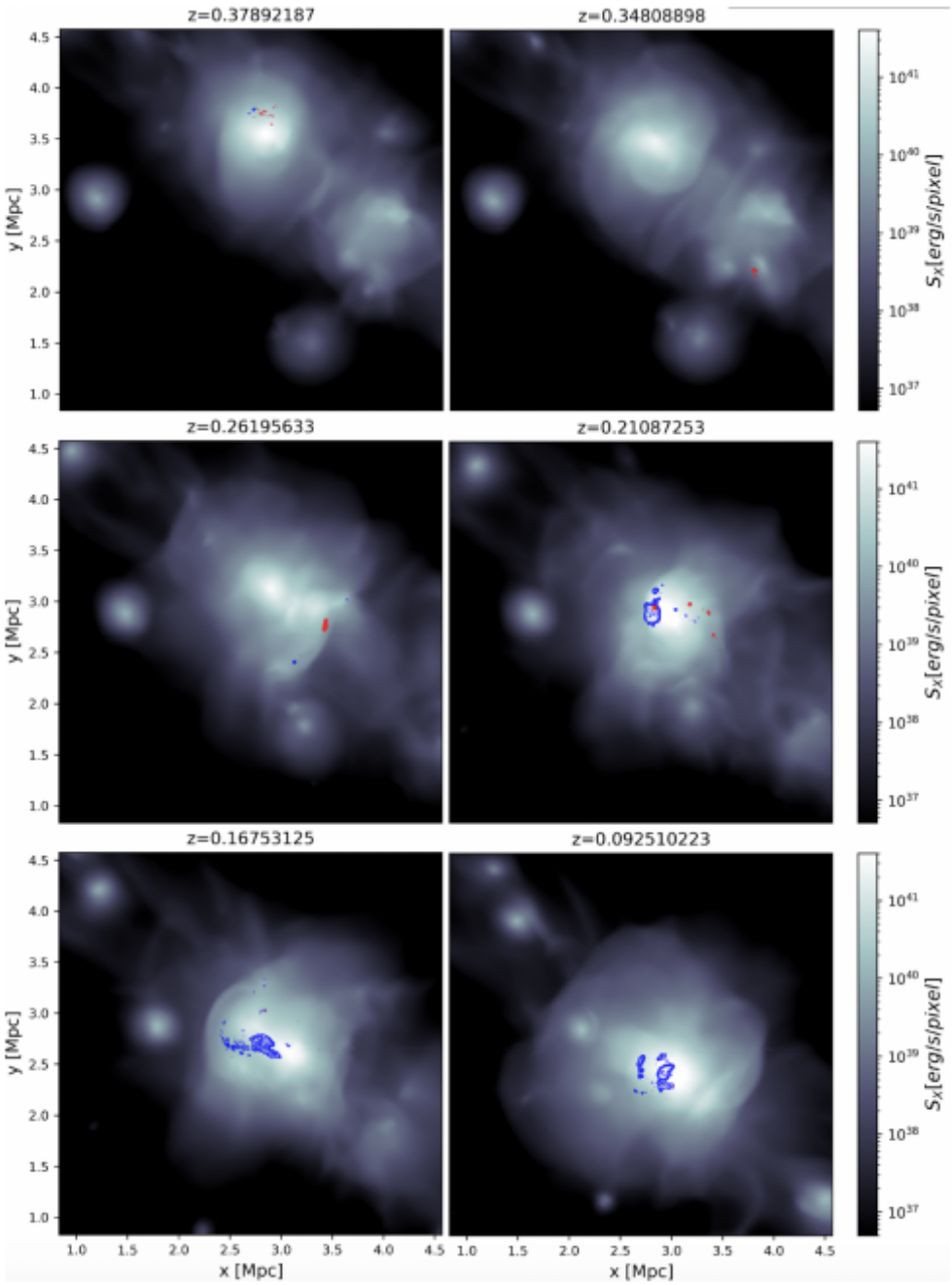

Figure 2.4: Evolution of the X-ray surface brightness (grey colours) and of the detectable radio emission at 50 MHz with LOFAR LBA for z $\leq$ 0.4, for all electrons seeded by radio jets at z = 0.5 and later re-accelerated by shocks and turbulence [6].

2.3 Mathematical modelling and numerical analysis

To compare our cluster simulations to observations, I can compute the expected hadronic γ-ray photon flux from the formula [59],

$$F_\gamma = \int q_\gamma(r, E_\gamma) dE_\gamma dV \tag{2.2}$$

with function q_γ from Pfrommer & Enßlin (2004),

$$q_\gamma(r, E_\gamma) \simeq \sigma_{pp} c n_N(r)(\tilde{n}_{CRp}(r)) \times \frac{2^{4-\alpha_\gamma}}{3\alpha_\gamma}(\frac{m_{\pi^o}c^2}{Gev})^{-\alpha_\gamma}[(\frac{2E_\gamma}{m_{\pi^o}c^2})^{\delta_\gamma} + (\frac{2E_\gamma}{m_{\pi^o}c^2})^{-\delta_\gamma}]^{\frac{-\alpha_\gamma}{\delta_\gamma}} \quad (2.3)$$

where,

- σ_{pp} is $32(0.96+ e^{4.4-2.4\alpha_\gamma})$ is the effective cross section for proton-proton collision in mbarn;
- c is the speed of light;
- $n_N = n_e(r)/1 - 0.5X_{He}$ is the target number density ($n_e(r)$ is the electron number density taken from simulation and $X_{He} = 0.24$ is the fraction of helium;
- $\alpha_\gamma = 4(\alpha_p - 0.5)/3$ is the γ spectral index;
- m_{π^o} is the mass of pion;
- $\delta_\gamma = 0.14\alpha_\gamma^{-1.6} + 0.44$ is the shape parameter;
- $\tilde{n}_{CRp}$ is the cosmic ray density.

In my thesis I produced new code implementations, in the Julia language, to efficiently compute the resulting gamma-ray flux for each simulation and at all simulated epochs, for a variety of plausible model described in Section 2.1. With the observational results obtained from Fermi LAT Satellite, I tentatively constrain the initial amount of CRp in radio jet. This approach promises to be a powerful theoretical tool to combine observed radio properties of diffuse radio sources in clusters of galaxies, and constraints from gamma-rays, to better understand the composition of jets from AGN and their feedback activity in the ICM.

I integrate over the energy range E_γ= [0.5, 200] GeV to get the final flux in ph/s/cm^2. Absolute flux is calculated to compare the simulated flux with observation flux of clusters at different distances. In the analysis along with the σ_{pp} in Eqn 2.3, I also employed alternative cross-section formula from Kelner et al (2006) to make comparisons and identify the most realistic one.

$$\sigma_{pp} = \left(1.0 - \left(\frac{1.22}{E_{\text{proton}}}\right)^4\right)^2 \cdot (34.3 + 1.88 \cdot L + 0.25 \cdot L^2) \text{ mb} \quad (2.4)$$

where, $L = \ln(E_{\text{proton}}/\text{Tev})$. The simulations which I analyzed typically contain $10^4 \sim 10^5$ tracers, which sample the cosmic ray electrons and protons spectra within 90 energy bins. Instead of using a constant spectral index over the entire energy range, the integration was performed using spectral index predicted by the Fokker-Planck evolution of

the CR spectra and the respective shape parameter and γ spectral index was used. The analysis is conducted for both the evolutionary models as discussed in the Section 2.1. In my modeling, I not only calculate the gamma-ray flux but also separately focus on determining the neutrino flux. I perform distinct mathematical modeling and analysis to understand the production and propagation of neutrinos in the system. To calculate the produced neutrino flux, I utilize the gamma-ray flux from Equation 2.3 and compute it by applying the following equation [48]:

$$F_\nu = q_\gamma \times (Z_{\nu_\mu} + Z_{\nu_e}) \tag{2.5}$$

where,

$$Z_{\nu_\mu} = \frac{4 \cdot (3 - 2 \cdot \mathrm{kk} - \mathrm{kk}^{\alpha_\gamma} \cdot (3 - 2 \cdot \mathrm{kk} + \alpha_\gamma - \mathrm{kk} \cdot \alpha_\gamma))}{\alpha_\gamma \cdot (1 - \mathrm{kk})^2 \cdot (\alpha_\gamma + 2) \cdot (\alpha_\gamma + 3)} + (1 - \mathrm{kk})^{\alpha_\gamma - 1} \tag{2.6}$$

$$Z_{\nu_e} = 24 \cdot \left(\frac{(1 - \mathrm{kk}) \cdot \alpha_\gamma - \mathrm{kk} \cdot (1 - \mathrm{kk}^{\alpha_\gamma})}{\alpha_\gamma \cdot (1 - \mathrm{kk})^2 \cdot (\alpha_\gamma + 1) \cdot (\alpha_\gamma + 2) \cdot (\alpha_\gamma + 3)} \right) \tag{2.7}$$

$$\mathrm{kk} = \frac{m^2_{\mu^{+/-}}}{m^2_{\pi^{+/-}}} = 0.573 \tag{2.8}$$

The upper flux limits obtained from FERMI observations, as discussed in Section 1.14, serve as an important benchmark for my simulations. I use these limits to compare and analyze the simulated gamma-ray flux in order to gain insights into the physical processes governing cosmic ray protons and their diffusion into the ICM over time. My thesis also focuses on aging of tracers i.e, the different ways in which the tracers can lose their energy while diffusing into the ICM. Losses due to ionisation, radiation, advection is taken into consideration. The final energy loss of a tracer depends on both loss mechanisms and the energy gain obtained from turbulent re-acceleration.

Chapter 3

Results and discussions

3.1 Single radio galaxy

This section examines the hadronic gamma ray flux generated by a single radio galaxy, based on the properties of Run A described in Table 2.1. It is similar to Run D parameters in Table 2.2 but with a SMBH with a jet injection phase of 10 Myr.

Initially, I provide an overview and analyze the plots to identify their general trends. I then address open questions pertaining to various cross-sections, spectral index variations, and different models.

- In Sections 2.3 and 2.1.2, two different models with distinct cross-sections were discussed. Figure 3.2, 3.3, and 3.6 present the results, indicating that the Np2 model produces slightly higher flux than the Np1 model. This discrepancy can be attributed to the re-acceleration mechanism, which boosts the energy of the tracers and consequently enhances the gamma-ray flux in the Np2 model.

- Furthermore, when comparing Figure 3.2 and 3.3, it becomes evident that the flux produced by a variable α_p is greater than that generated by a constant α_p, where α_p is set to 2.2. The observation about constant α_p should align with the findings of Beckmann et al (2022), where the maximum flux was achieved at $\alpha_p = 2.2$. But in my model, I have observed that the generated flux for variable α_p exceeds the maximum flux reported in Beckmann et al (2022). Potential factors that could contribute to the higher flux output in my model are thoroughly investigated in the further sections.

- Upon examining the flux generated by different cross sections, both for constant and variable α_p, as depicted in Figure 3.2 and 3.3, it is evident that the use of Kelner et al (2006) (Eqn 2.4) for σ_{pp} results in significantly lower flux, approximately two

orders of magnitude less, compared to the flux calculated using (Eqn 2.3) pfrommer & Enslinn (2004). Eqn 2.4 from Kelner et al (2006) is employed in recent papers. Despite its use in the literature, its impact on the overall flux output is crucial. Thus Kelner et al (2006) is retained for the rest of the gamma ray estimates in the thesis.

- Overall, for further calculations and discussions, a variable α_p with σ_{pp} using Equation 2.4 is only considered.

- The upper limits on point-mass γ-ray fluxes are from Ackermann et al (2014) across a span of virial masses, $0.2 \leq \frac{M_{200}}{10^{15} M_{\odot}/H_{70}} \leq 0.4$. The selection of the mass range was made to closely align with the mass of the cluster simulated. This comparison encompasses both cool and non-cool clusters, as my simulation doesn't pertain to any particular cluster type. In the plots, the limits corresponding to cool clusters are shaded in green, while the limits for non-cool core clusters are shaded in brown.

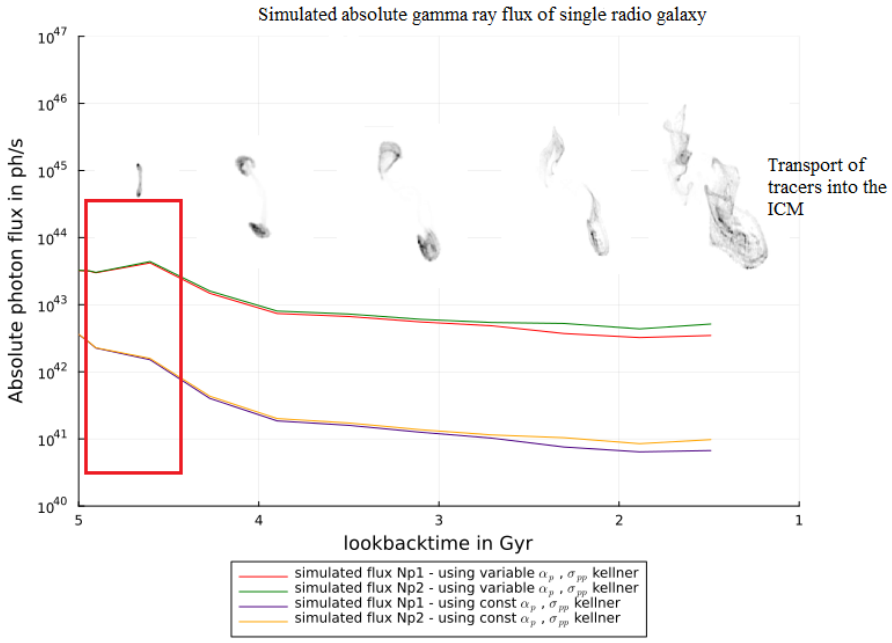

Figure 3.1: Absolute gamma ray flux calculated for the models Np1 and Np2 with a variable and constant α_p condition using the cross-section from Eqn 2.4. It is visualised along the transport of tracers into the ICM. The red box indicates the initial phase after jet injection, which we do not consider to compare with observations (see text for explanations).

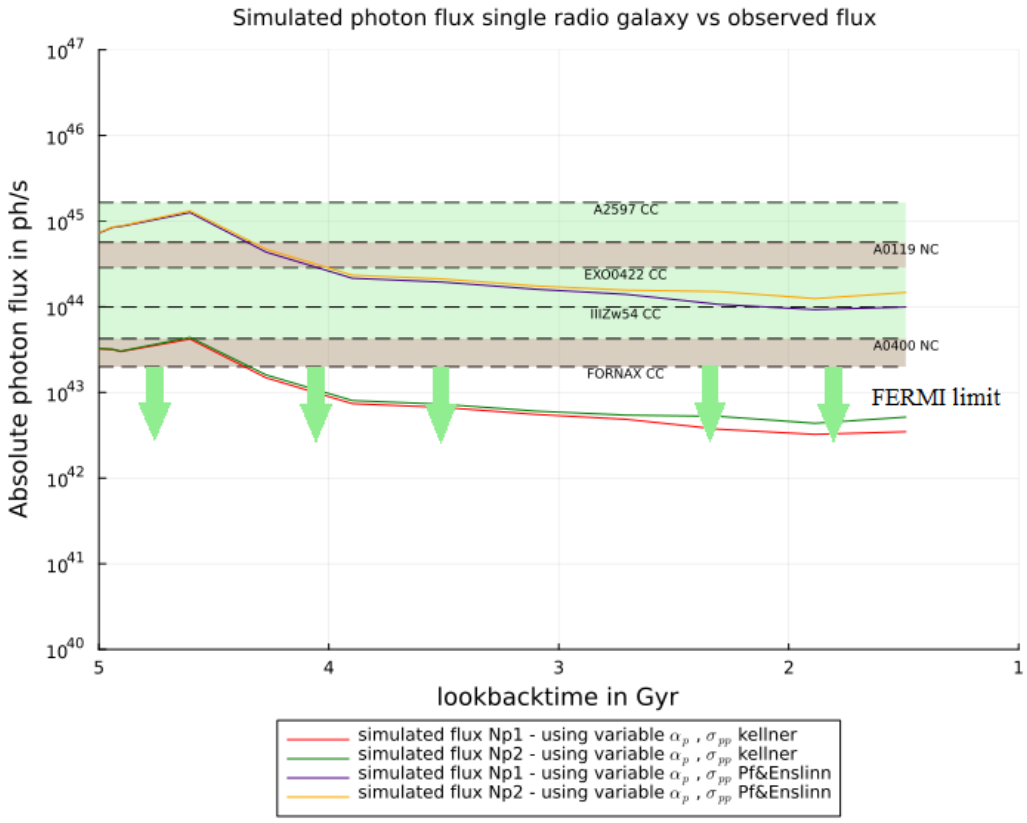

Figure 3.2: Absolute gamma ray flux calculated for the models Np1 and Np2 with a variable α_p condition for different cross-section.

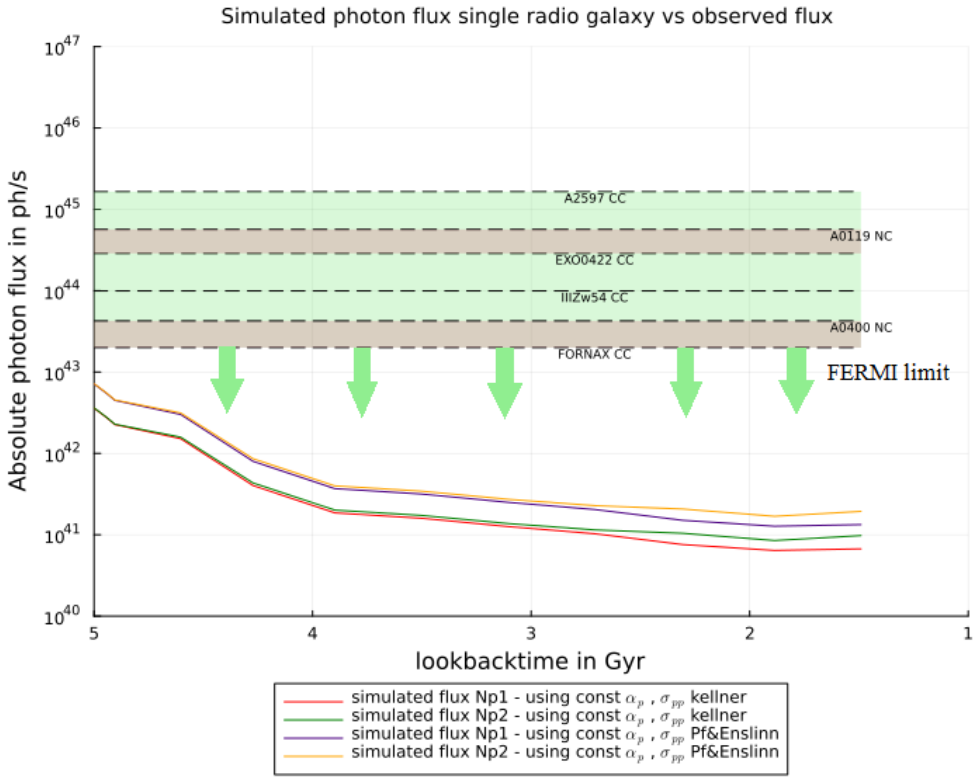

Figure 3.3: Absolute gamma ray flux calculated for the models Np1 and Np2 with a constant α_p condition for different cross-section.

The trends observed in the graphs consistently remain the same regardless of the specific values of α_p and σ_{pp} used in the simulations. Having analyzed the effects of the spectral index and cross-section on the flux production, I now focus on the absolute gamma-ray flux trends and their comparison with the FERMI limits. To ensure a meaningful comparison, I consider the flux after it has undergone evolution and diffusion into the ICM after a period of 4 Gyr. The time period inside the red box in Fig 3.4 is neglected for discussions and comparison. The choice of this specific time frame is justified by the following reasons:

- During the initial phase of 100 Myr, when the radio lobes are not yet fully extended, the AGN is as a bright compact gamma-ray source. Notably, FERMI observations of the ICM take into account this AGN contribution and focus on detecting the gamma-ray flux solely from the ICM, after removing the AGN contribution. As a result, the higher flux levels produced by the simulations during this initial 100 Myr phase can be considered negligible when comparing with the FERMI observations of the ICM. It is also well know that the physics of AGN at small distances remains a mystery.

- During the transition period, lasting until approximately 1 Gyr after the jet injection phase, the radio source becomes invisible in radio observations. This has been also witnessed in the simulation of single and multiple radio galaxies where the cosmic rays electrons are invisible for a certain period of time and then re-emerge when they encounter a re-acceleration event Vazza et al (2021) A&A. This occurs roughly 200 Myr after the jet injection phase begins. The primary reason for this phenomenon is that the electrons in the system lose their energy rapidly, primarily through synchrotron and inverse compton radiation within a relatively short timescale of about 10^8 years, in the absence of re-acceleration. The lack of re-acceleration events during the initial phase leads to the complete invisibility of the radio source. Consequently, comparison of gamma-ray flux produced during this transition phase with FERMI limits does not provide any meaningful result. Thus, for the purpose of discussion, this initial period is disregarded.

- In my simulations, the jets are not fully devoid of thermal gas or filled only by magnetic field energy; they have some initial gas density. As a result, during the initial period, the presence of this gas density contributes to the production of a high gamma-ray flux. As the jets evolve and diffuse into the ICM, which is a region of lower density, the γ ray flux produced gradually decreases. As a result of the various reasons discussed, the initial period is disregarded in my analysis, and my focus is primarily on the later stages. During this later period, I closely examine the gamma-ray flux produced and assess its implications on the cosmic content within the jet.

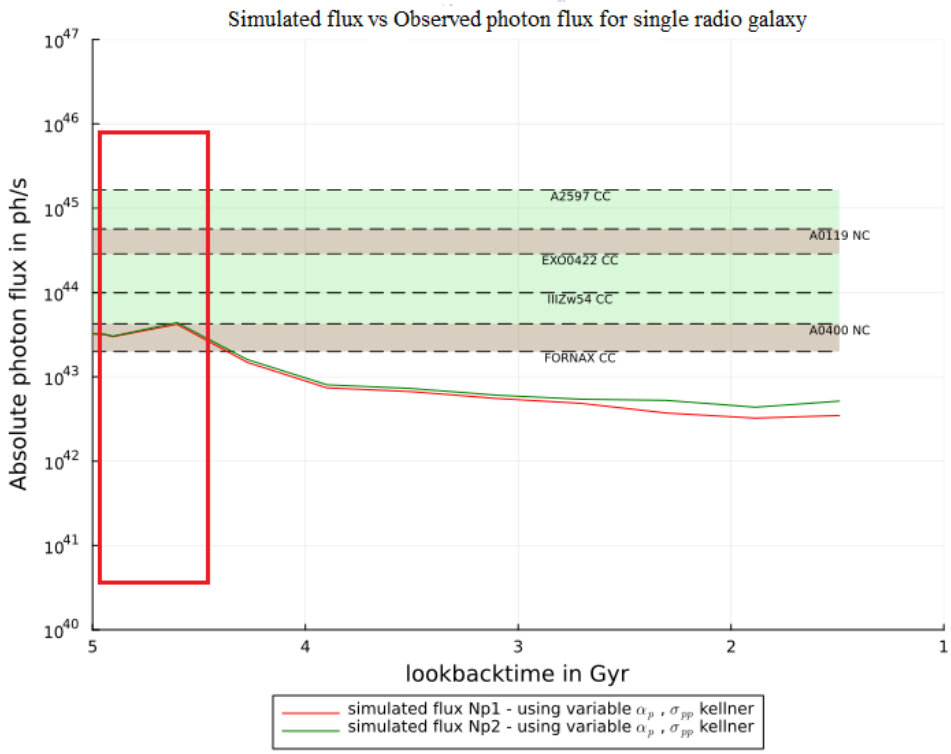

Figure 3.4: Absolute gamma ray flux calculated for the models Np1 and Np2 with a variable α_p condition for cross-section using Eqn 2.4. The red box indicates the initial phase after jet injection, which we do not consider to compare with observations (see text for explanations).

While the current analysis, based on Fig 3.4 and my chosen considerations (variable α_p and σ_{pp} using Equation 2.4), shows that the gamma-ray flux remains $3 \sim 4$ times below the FERMI limits, it is crucial to acknowledge that this is not the final result. My examination is limited to a single episode of AGN feedback scenario. In reality, multiple episodes can occur, as evidenced in the Perseus and A1795 clusters. For example, using *Chandra* in A1795 cluster the complex structure observed in the northwest (NW) direction is an indicative of three epochs of AGN activity. Two distinct edges are observed: the NW edge and the arc edge, with the latter being closer to the core. These two regions contain compressed material and acts as the boundary between three cavities, corresponding to the three outbursts. All observed signatures both in radio and X-ray are consistent with several consecutive episodes of AGN activity, which gave rise to the observed morphology NW and SW from the core [61]. Also, the detailed studies of cavities in nearby clusters have revealed that there are possibilities to have $N_{Burst} \geq 4$ (Sanders et al (2006), De Gasperin et al (2012), Brienza et al (2021)).

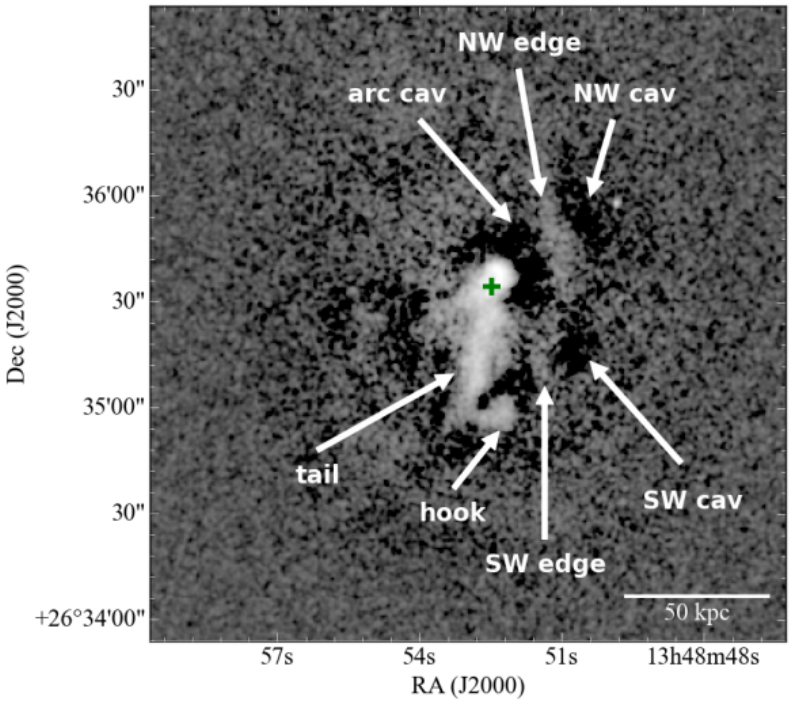

Figure 3.5: Chandra X-ray surface brightness residual map of A1795 in the 0.5–7 keV band. Various features of interest in the core of A1795 are labeled [61].

Thus, these multiple episodes have the potential to collectively surpass the FERMI limits, offering valuable constraints on the cosmic content within the jets. By accounting for 3-4 recurrent bursts, the cumulative gamma-ray emission by feedback episodes of similar power will exceed the FERMI limit.

Indeed, the analysis considering 3-4 radio bursts is not the final case for putting constraints on the cosmic content within the jets. It provides valuable insights for a single radio galaxy with a fixed power scenario, but to gain a comprehensive understanding, I must also explore how varying the power of the jet influences the gamma-ray flux produced. Would jets of a different initial power change this simulated γ ray emission level in a significant way? To address this question , in the next section I investigate the impact of different jet powers from the AGN on the gamma-ray flux. Understanding how higher jet power can lead to increased gamma-ray emission is essential as it can alter the constraints imposed on the cosmic content within the jets.

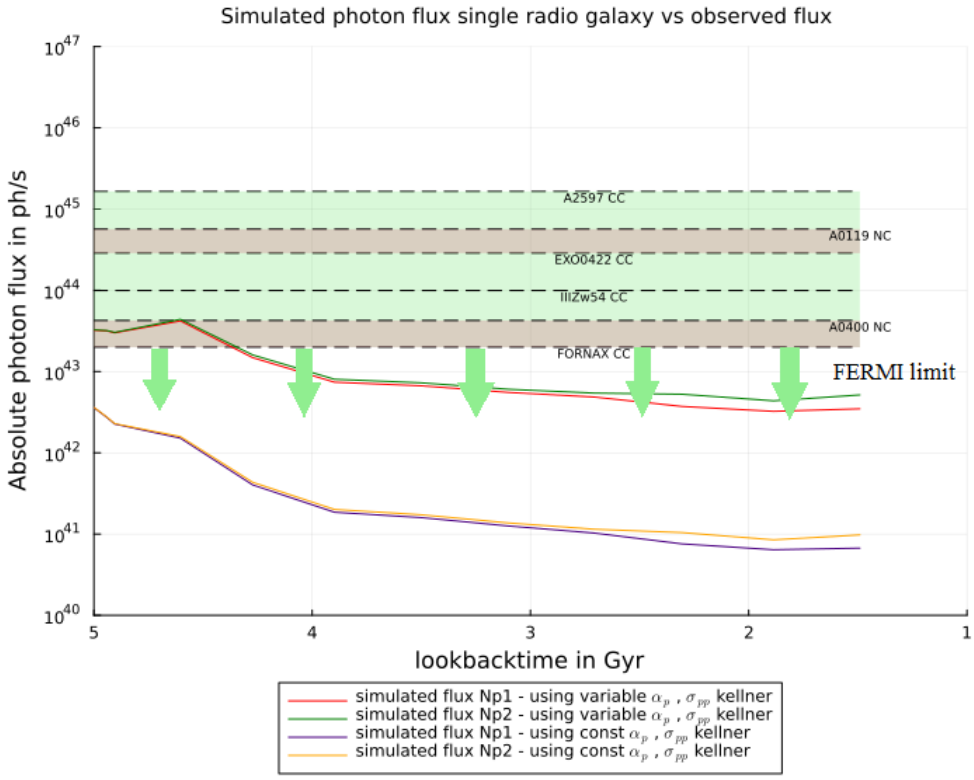

Figure 3.6: Absolute gamma ray flux calculated for the models Np1 and Np2 with a variable and constant α_p condition using the cross-section from Eqn 2.4.

3.1.1 Gamma-ray maps of a single radio galaxy

Before analysing a single radio galaxy with varying powers, I have generated γ-ray maps based on the parameters of Run A for a single radio galaxy with constant power. This helps to obtain a clarity of the spatial distribution and mixing of tracers within the thermal gas of the ICM as the time evolves. This visualization approach not only facilitates a more insightful comprehension of tracer trajectories but also serves as a valuable tool for comparing the temporal progression of tracers under varying power conditions and when multiple radio galaxies are introduced. The interpretation also contributes to the understanding of the mechanism behind gamma-ray generation.

γ-ray maps of single radio galaxy evolving with time

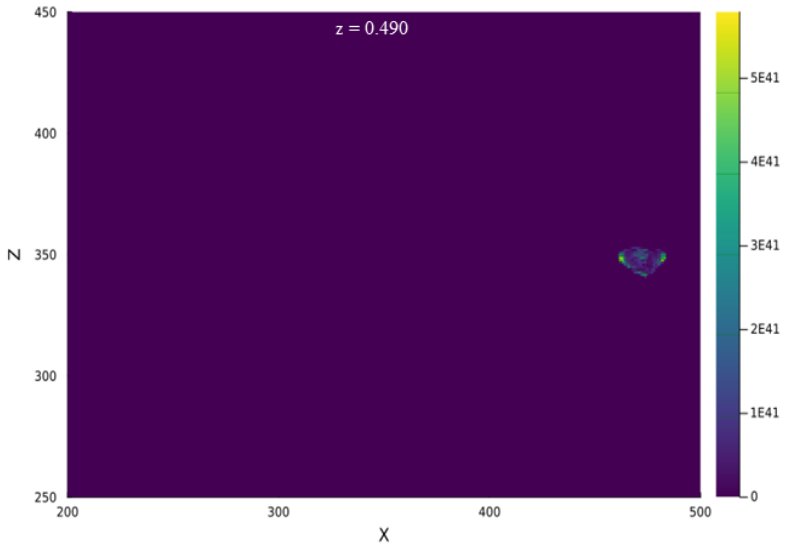

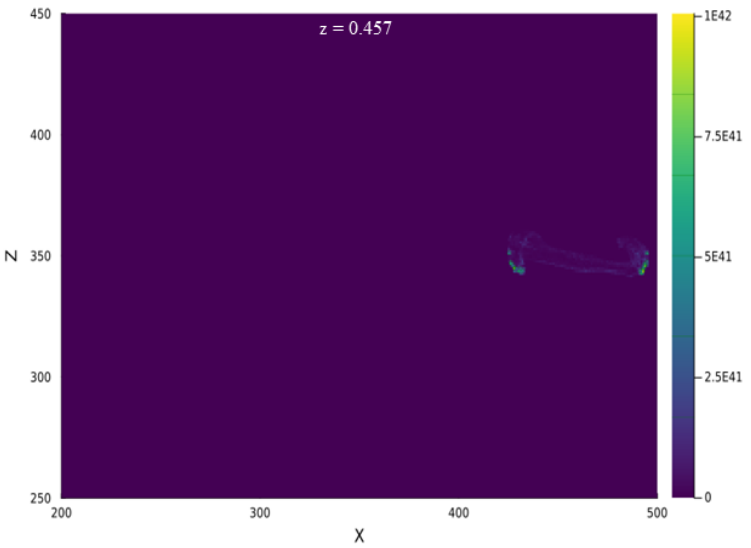

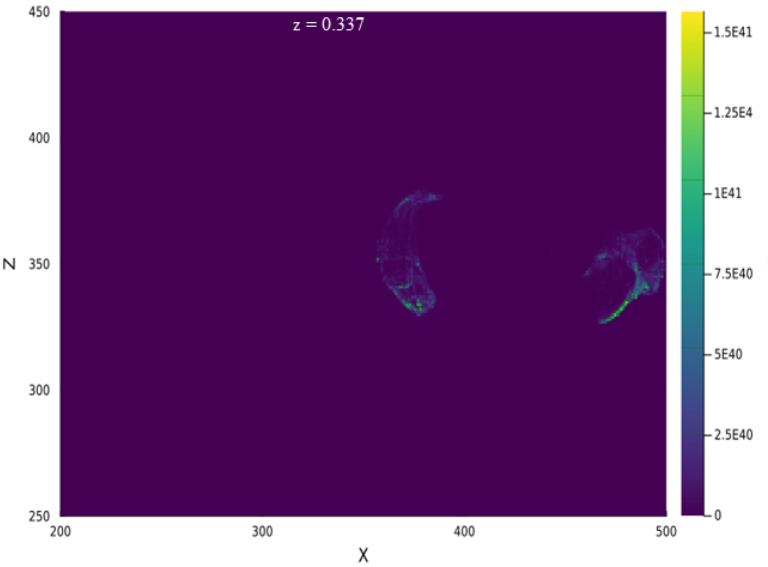

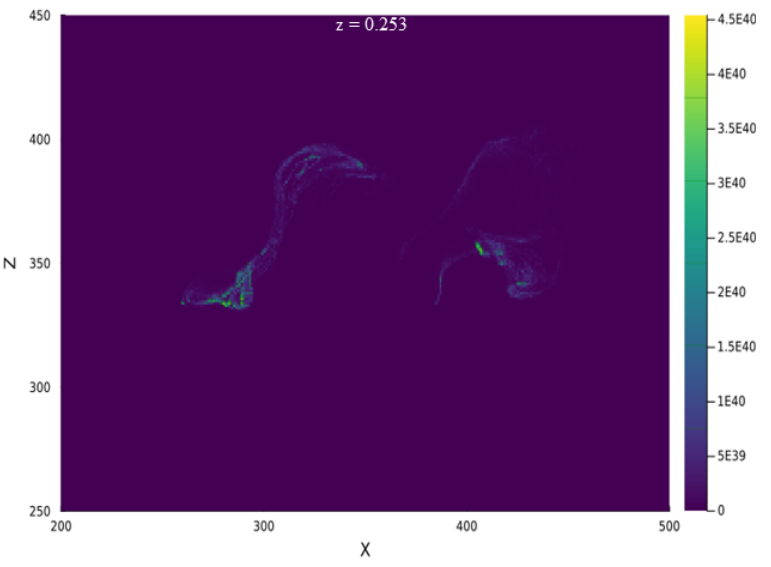

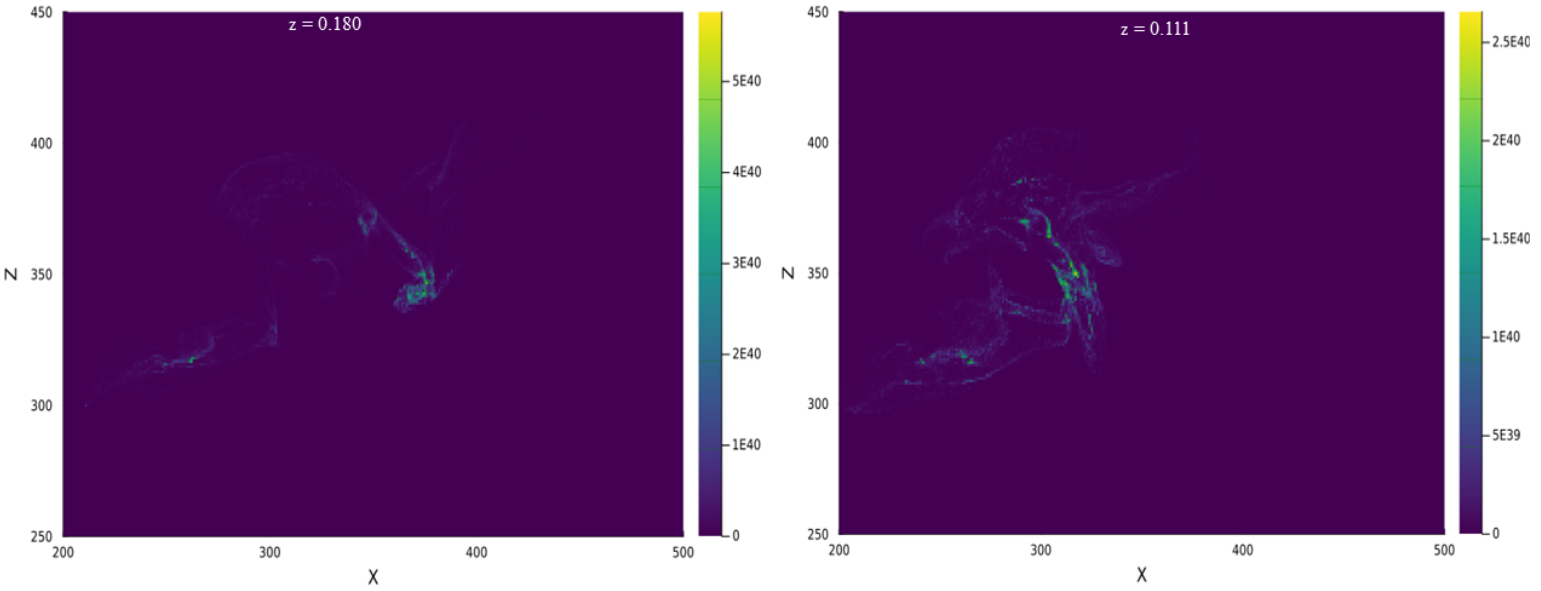

Figure 3.7: γ-ray maps representing the spatial evolution of the tracers with time into the ICM from a single radio jet. The X and Z axes represent the distance traveled by the tracers in the respective axes in kpc and z is the redshift at which the map is being produced. The minimum resolution of the γ-ray map is 8.86 kpc. Colorbar representing the gamma-ray flux generated by individual tracer in ph/s.

From the Figure 3.7, the evolution of tracers within the ICM becomes apparent. Initially, the tracers are closely confined in proximity to the AGN (γ-ray maps at z = 0.490, 0.457). However, as time progresses, the expansion of the radio lobes leads to the dispersion of these tracers across a broader region within the ICM.

3.2 Single radio galaxy with different powers

In this section, I delve into the variation of gamma-ray flux as a function of jets with different powers. To conduct this analysis, I utilize the simulation dataset specified in Table 2.2, which provides the necessary parameters for my calculations. By employing the parameters from the dataset, I evaluate the gamma-ray flux for different power settings. This comprehensive examination allows me to understand the relationship between jet power and the resulting gamma-ray emission. As indicated in Table 2.2, the analysis encompasses five distinct models. Taking into account the conclusions drawn in Section 3.1, where I decided to focus solely on a variable α_p with σ_{pp} using Eqn 2.4 due to various reasons, I now focus into how the power of AGN influences the gamma-ray flux.

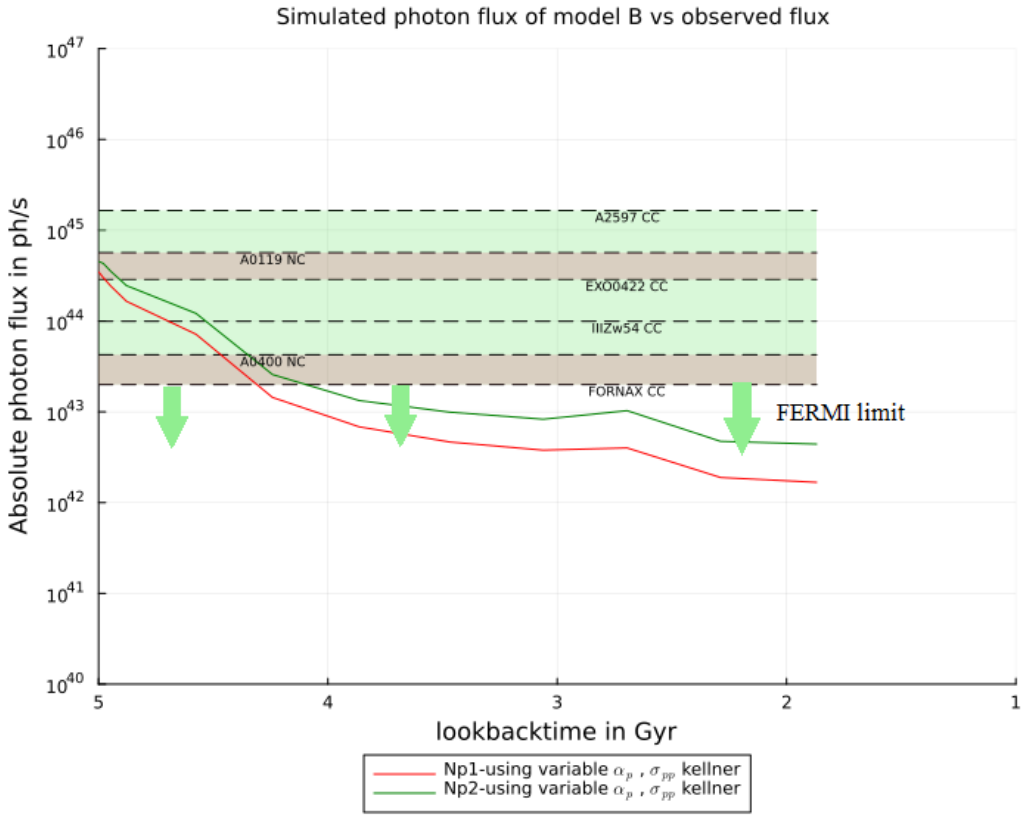

Figure 3.8: Absolute gamma ray flux calculated for the models Np1 and Np2 with a variable α_p condition using the cross-section from Eqn 2.4 for Run B.

In Run B, I observe a relatively lower jet power of 3×10^{44} ergs/s compared to the power used in my previous Run A discussed in section 3.1. Surprisingly, despite the lower power, the gamma-ray flux produced in this model, as shown in Fig 3.8, is two orders of magnitude higher. Although I can neglect the initial phase of gamma ray flux, as discussed in the previous Run A, the overall higher flux in Run B demands an explanation. The explanation for this intriguing phenomenon lies in the behavior of the radio lobes at lower jet powers. With lower power, the radio lobes are unable to extend out to a larger distance from the cluster core, causing them to remain confined within a high-density core region. This is evident in the γ-ray maps depicted in Figure 3.9. Even at a redshift of 0.29, the tracers exhibit a consistent concentration near the AGN's vicinity, and they have travelled to a very low extent. The gamma-ray flux is influenced by a combination of gas density and cosmic ray number density, as expressed in Eqn 2.3 ($F_\gamma \propto n_{th} \cdot n_{CR}$). At lower jet powers, the confined radio lobes interact with the higher-density , resulting in a substantial increase in the gamma-ray flux. The confinement of radio lobes in a high-density region thus plays a crucial role in generating this elevated gamma-ray emission. This interplay is very crucial because as the power increases the tracers can travel to farther low density regions thus reducing the total gamma-ray flux.

In the previous Run A, I did not observe a distinct difference between Np1 and Np2, except in the final phase. However, in Run B, a notable difference between Np1 and Np2 is evident. This difference arises due to the presence of turbulence and shock re-acceleration events in Run B.

In Run B, the radio lobes are confined, which means that the cosmic rays tend to remain in proximity to the AGN. As these cosmic rays propagate through the confined regions, they encounter merger shocks and undergo DSA re-acceleration. Moreover, in high-density regions within the radio lobes, turbulent re-acceleration events are also present. This phenomenon offers a plausible explanation for the distinct differences observed between Np1 and Np2 models in Run B. In Run B, where turbulence and shock re-acceleration events are mostly arising in the cluster core region produces a higher flux.

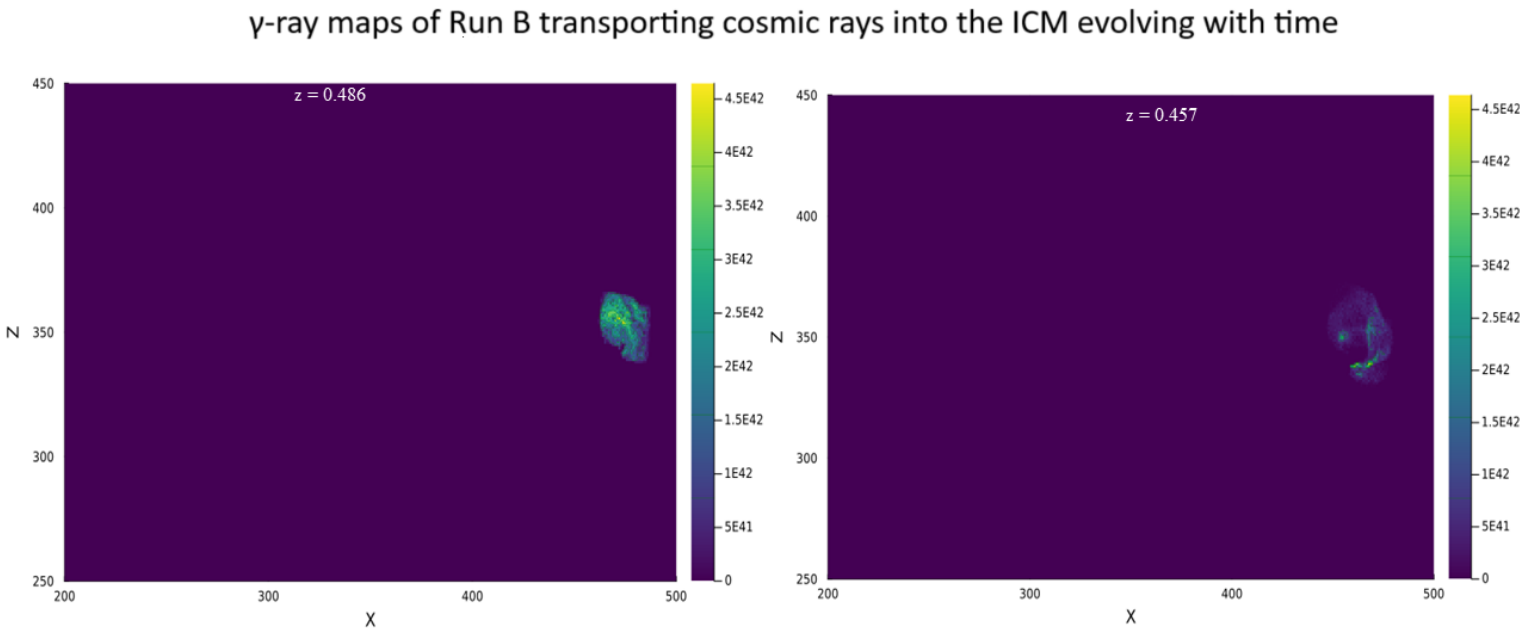

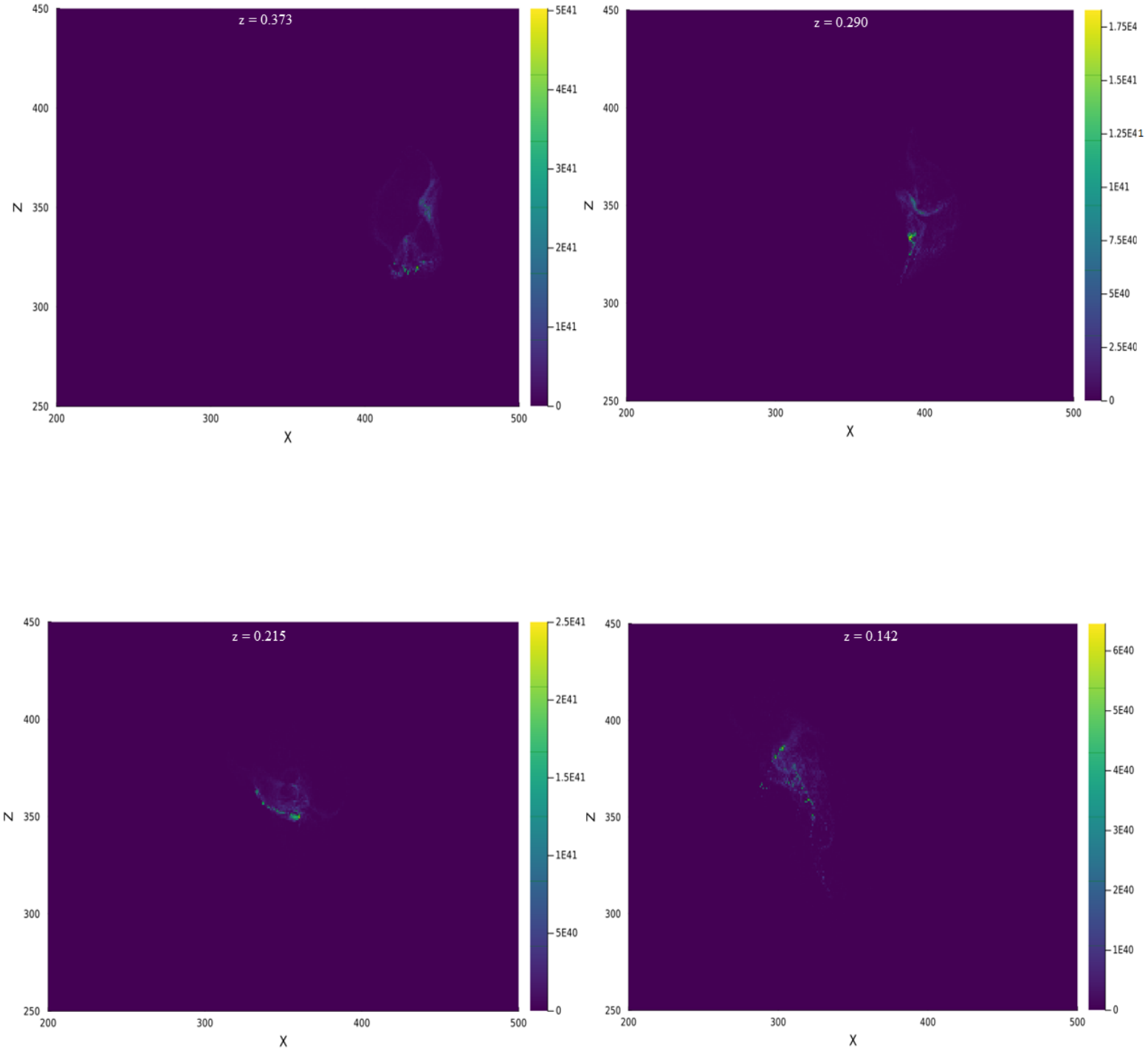

Figure 3.9: γ-ray maps representing the spatial evolution of the tracers with time into the ICM in Run B. The X and Z axes represent the distance traveled by the tracers in the respective axes in kpc and z is the redshift at which the map is being produced. The minimum resolution of the γ-ray map is 8.86 kpc. Colorbar representing the gamma-ray flux generated by individual tracer in ph/s.

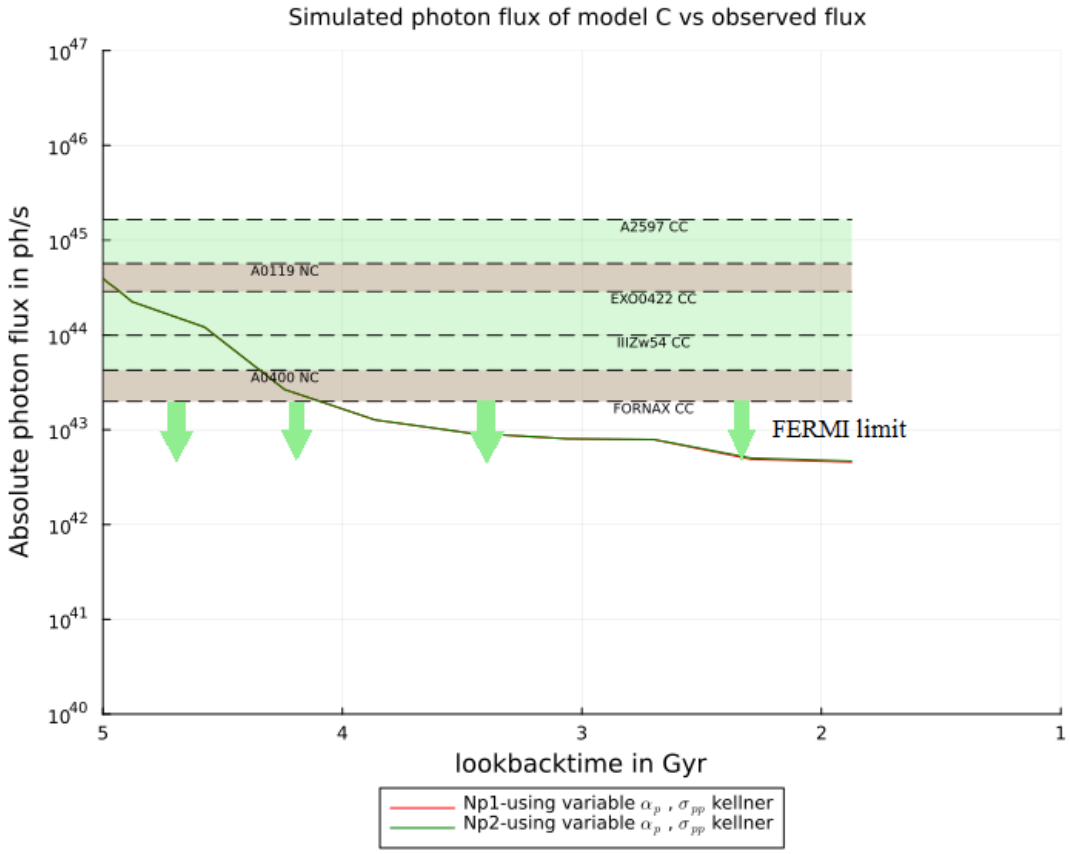

Figure 3.10: Absolute gamma ray flux calculated for the models Np1 and Np2 with a variable α_p condition using the cross-section from Eqn 2.4 for Run C.

In Run C, the jet power is increased three times compared to Run B, rising from 3×10^{43} erg/s to 9×10^{43} erg/s. However, despite this power increase, the simulation output indicates that it is insufficient to propel the tracers in the jet to far distances. In Fig 3.11 despite a better diffusion of tracers into the ICM when compared to the Fig 3.9 the distance they have traversed remains almost consistent. In the γ-ray map Fig 3.11, at z = 0.375 the lobes are still closer to the AGN and confined. The inability of the jets to reach lower dense regions limits the reduction of gamma-ray flux in Run C. An intriguing observation in Run C is that the gamma-ray flux for both the Np1 and Np2 models is identical. This can be attributed to the increase in cosmic ray number density (as shown in Table 2.2), which subsequently augments the gamma-ray flux in the Np1 model. The increase in cosmic ray number density leads to an increase in the rate of particle interactions and gamma-ray production, resulting in a higher flux for the Np1 model. The increase in cosmic ray number density also explains the better diffusion of tracers into the medium (Fig 3.11) when compared to the γ-ray maps of B Run (Fig 3.9).

Conversely, the Np2 model in Run C does not experience the generation of new re-acceleration sites or shock re-acceleration. As a consequence, the gamma-ray flux in the

Np2 model remains the same as observed in Run B, since re-acceleration events overall do not significantly change the CR proton spectra in this run.

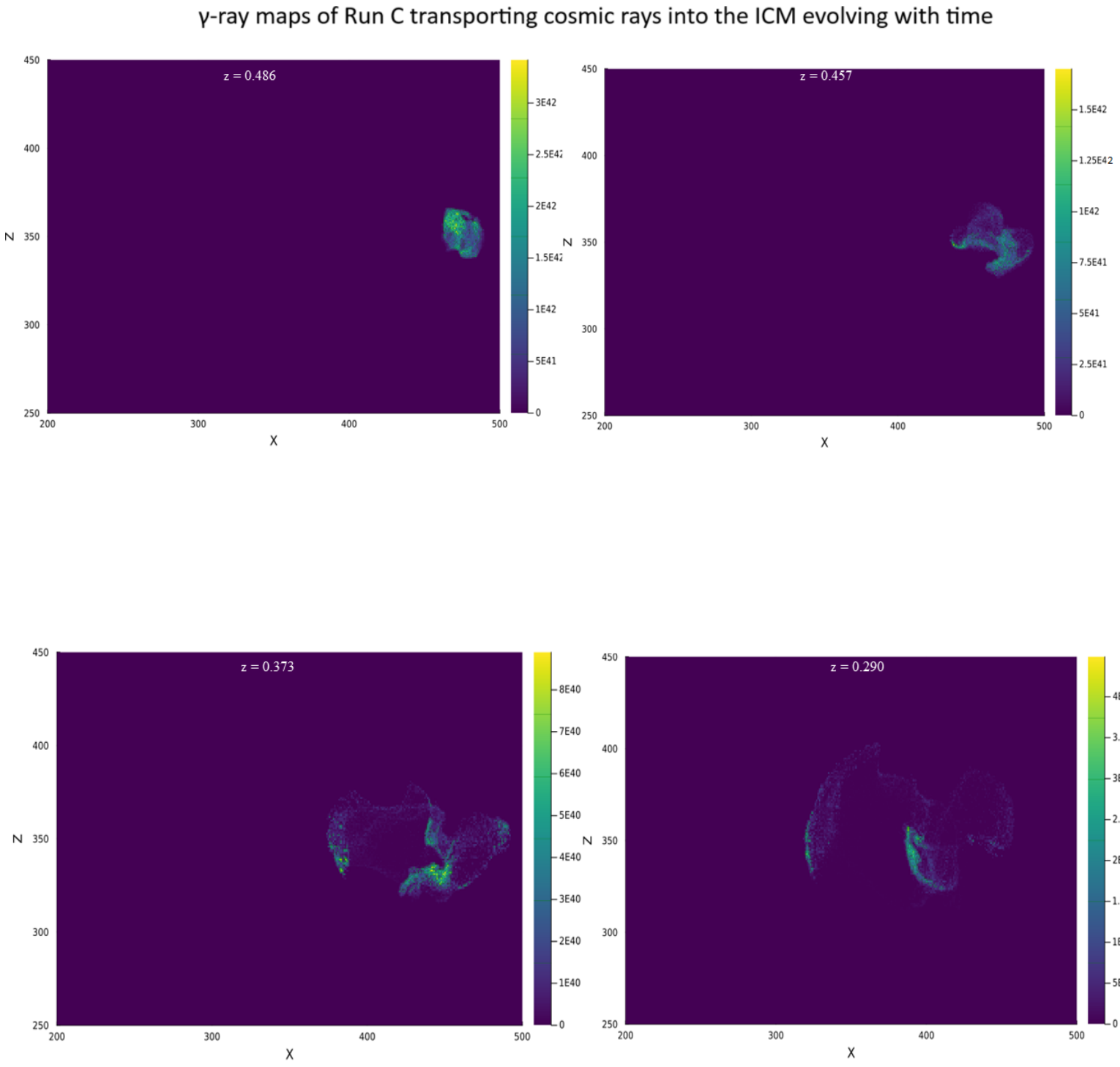

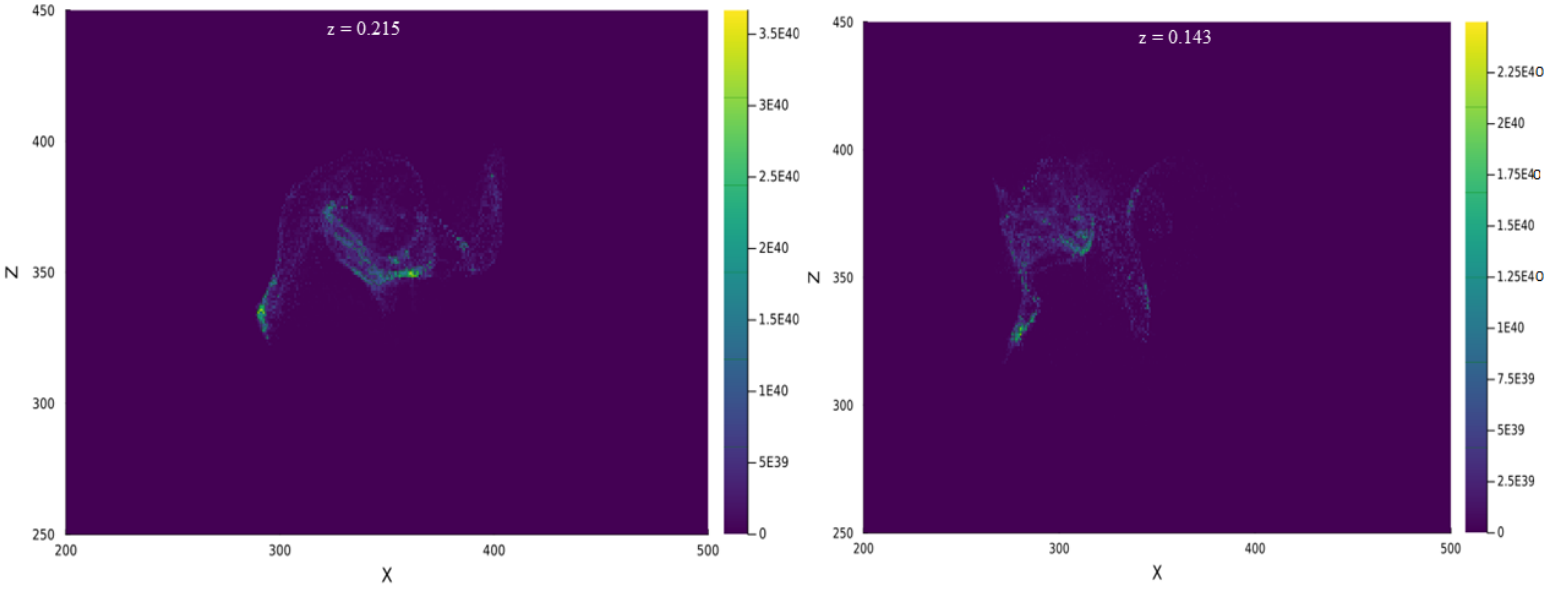

Figure 3.11: γ-ray maps representing the spatial evolution of the tracers with time into the ICM in Run C. The X and Z axes represent the distance traveled by the tracers in the respective axes in kpc and z is the redshift at which the map is being produced. The minimum resolution of the γ-ray map is 8.86 kpc. Colorbar representing the gamma-ray flux generated by individual tracer in ph/s.

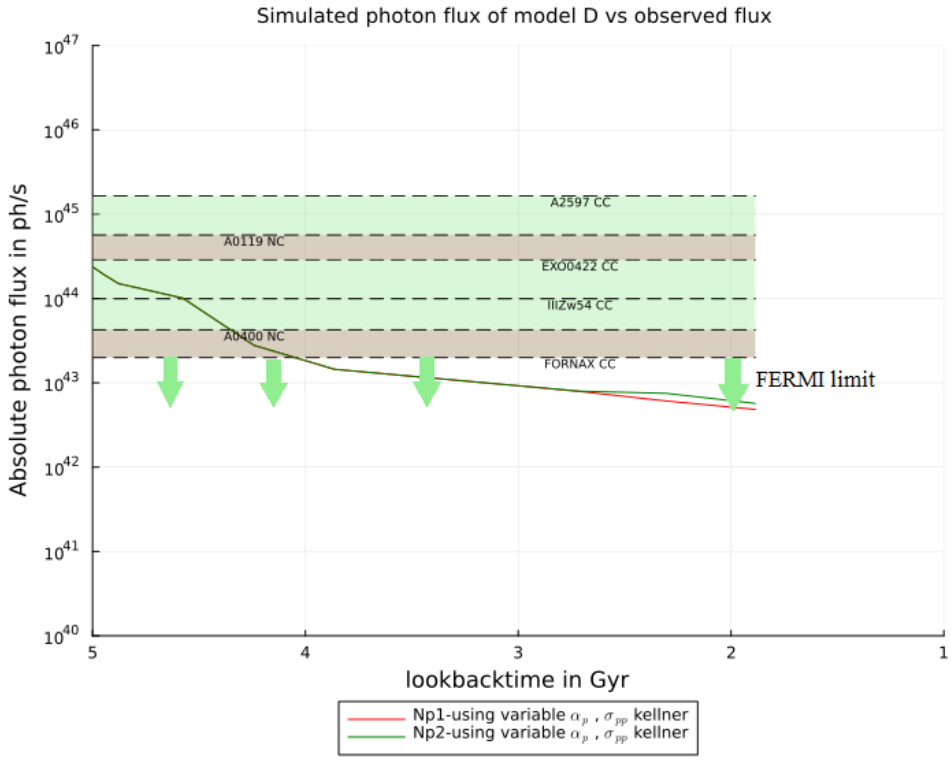

Figure 3.12: Absolute gamma ray flux calculated for the models Np1 and Np2 with a variable α_p condition using the cross-section from Eqn 2.4 for Run D.

In Run D, the jet power has increased significantly by an order of magnitude to 3×10^{44} erg/s. Surprisingly, despite this substantial increase in power, the gamma-ray flux has only reduced by half when compared to the previous Run C. Eventhough the cosmic ray number density increases in each run, the observed decrease in flux can be attributed to the tracers' extended diffusion into regions characterized by lower density. This is vividly seen in the γ-ray maps showcased in Figure 3.13, particularly at z = 0.215 and 0.143. The consistent trends observed in the Np1 and Np2 models are similar to those seen in Run C, as they are driven by the same underlying mechanisms. In the final phase of Run D, a slightly higher gamma-ray flux is observed for the Np2 model. This increase in flux can be attributed to some turbulent re-acceleration events.

γ-ray maps of Run D transporting cosmic rays into the ICM evolving with time

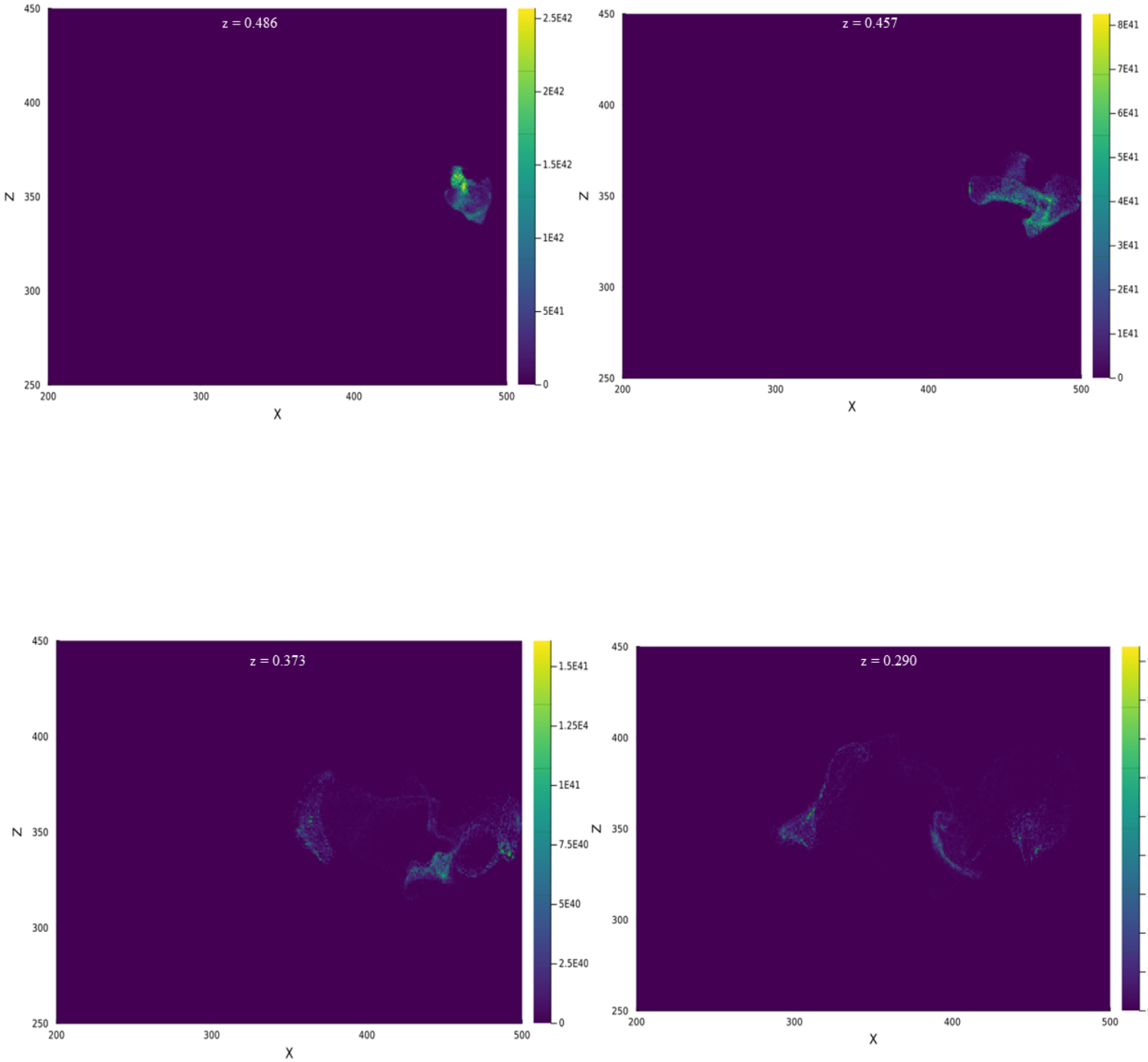

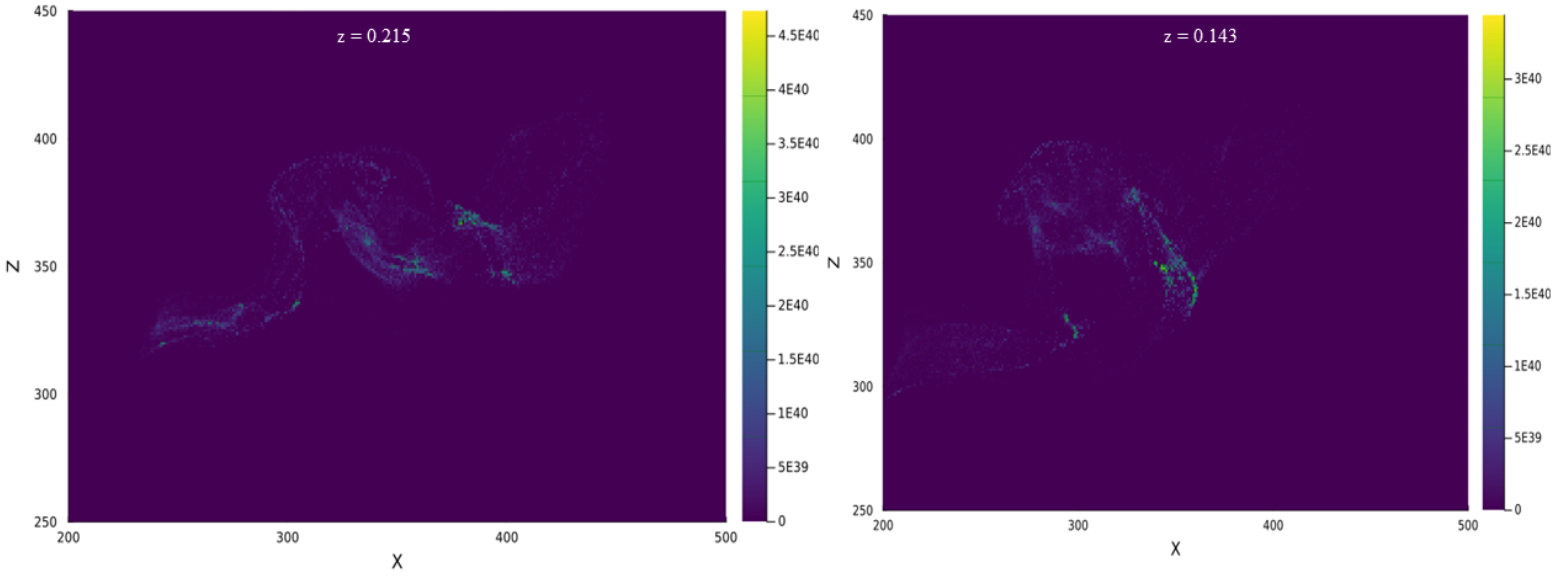

Figure 3.13: γ-ray maps representing the spatial evolution of the tracers with time into the ICM in Run D. The X and Z axes represent the distance traveled by the tracers in the respective axes in kpc and z is the redshift at which the map is being produced. The minimum resolution of the γ-ray map is 8.86 kpc. Colorbar representing the gamma-ray flux generated by individual tracer in ph/s.

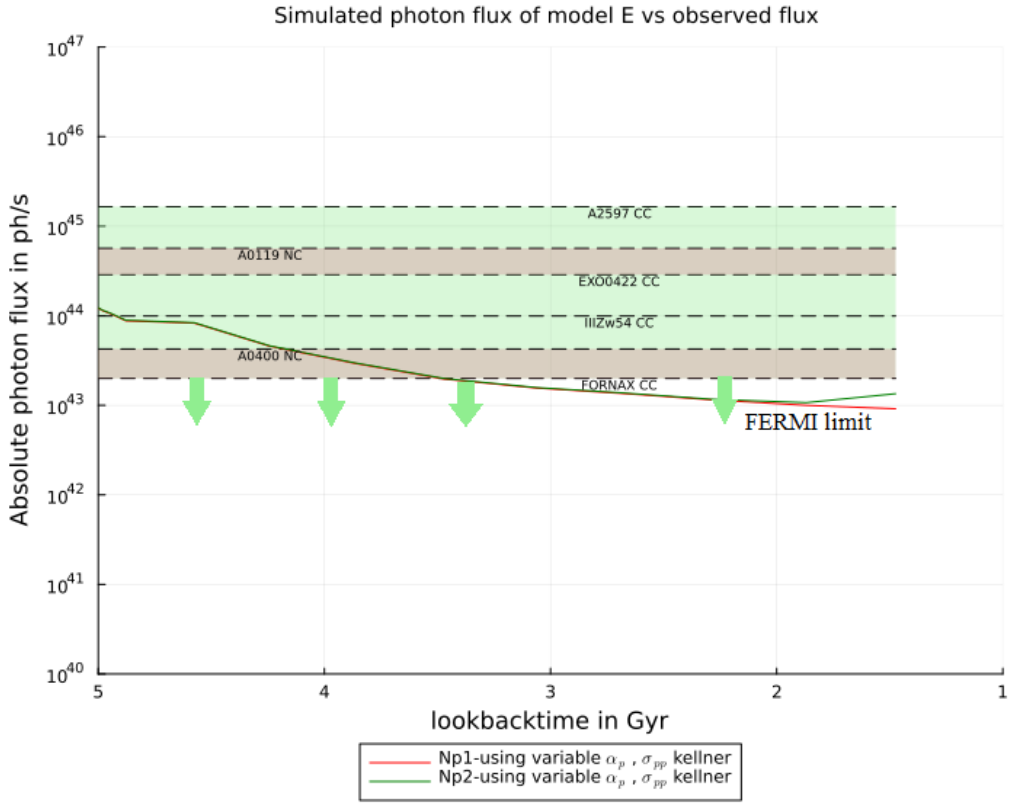

Figure 3.14: Absolute gamma ray flux calculated for the models Np1 and Np2 with a variable α_p condition using the cross-section from Eqn 2.4 for Run E.

In Run E, the jet power is approximately 9×10^{44} erg/s but the gamma-ray flux has again only reduced by a negligible amount compared to the previous run. The behavior of the Np1 and Np2 models in this run continues to follow the same trend, with a slightly elevated flux observed in the Np2 model during the final stages. In the γ-ray maps Fig 3.15 there is a effective mixing of tracers when compared to the distribution of tracers in Run D (Fig 3.13). Despite this effective mixing, the tracers have covered a similar distance as observed in Run D (Figure 3.13). This effective mixing of tracers over an equivalent distance is likely the primary factor contributing to the slight reduction in gamma-ray flux. Given that the gamma-ray flux results from the interplay of factors ($F_\gamma \propto n_{th} \cdot n_{CR}$), a reduction in gas number density due to the influence of high jet power that can carry tracers to a lower density region leads to a corresponding decrease in the flux. Once the tracers have effectively mixed within the ICM as expected the tracers exhibit a notable decrease in numbers, as demonstrated at redshift z = 0.110 in Fig 3.15.

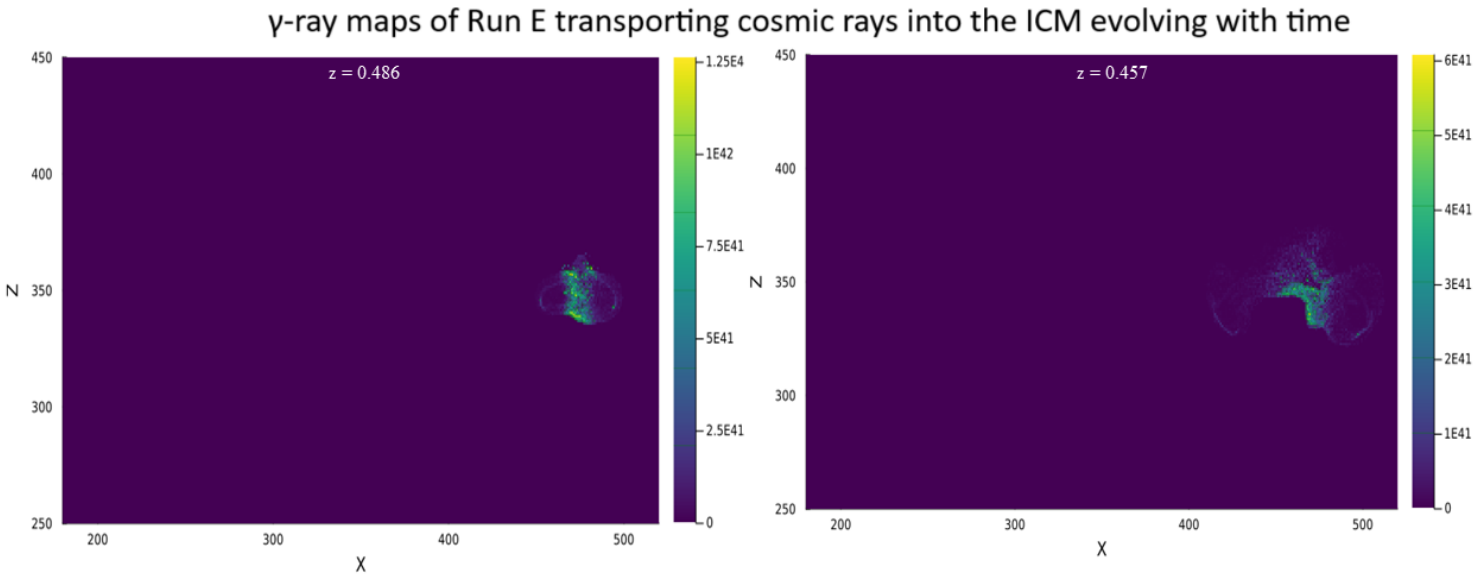

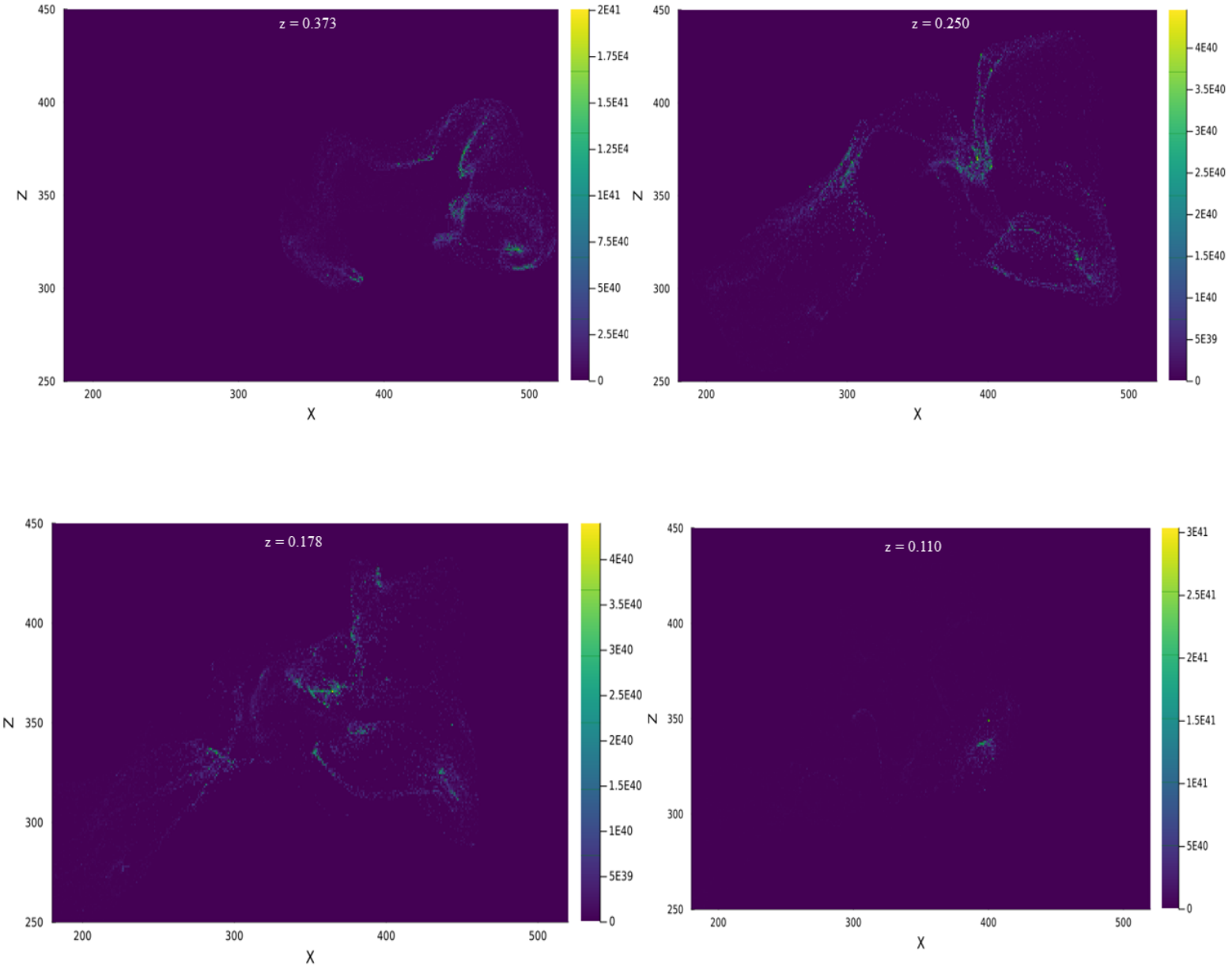

Figure 3.15: γ-ray maps representing the spatial evolution of the tracers with time into the ICM in Run E. The X and Z axes represent the distance traveled by the tracers in the respective axes in kpc and z is the redshift at which the map is being produced. The minimum resolution of the γ-ray map is 8.86 kpc. Colorbar representing the gamma-ray flux generated by individual tracer in ph/s.

In Run F (Fig 3.16), the overall flux produced shows no significant difference compared to the previous Run E. However, during the transition period between 4.5 to 4 Gyr, there appears to be an increased flux. Nonetheless, I must disregard the flux during this period due to the higher gas density in the simulation and the transitional nature of the radio galaxy, rendering it completely invisible. As with Run C, both Np1 and Np2 models in Run F exhibit the same flux throughout the evolution.

Despite the higher jet power, shocks are predominantly produced at the interface where the jets interact with the ICM. However, in this study, I focus on the tracers confined

within the lobes that could potentially be re-accelerated in the cavities. If I were to consider the contribution from these shocks, it is possible that the acceleration of particles in the shock could have caused cosmic content and flux to increase. Since the study is confined just to the lobes Np1 and Np2 models remain the same even at high jet power. The phenomenon of cavities and their dynamics remains an area of active research and is not yet fully understood.

The γ-ray maps displayed in Fig 3.17 vividly illustrate the impact of significantly higher power in comparison to the other Runs. This elevated power results in the tracers covering a considerably greater distance and quickly dispersing throughout the medium. At a z = 0.250, it becomes evident that the tracers have undergone rapid and extensive mixing with the ICM, leaving behind only a sparse number of tracers.

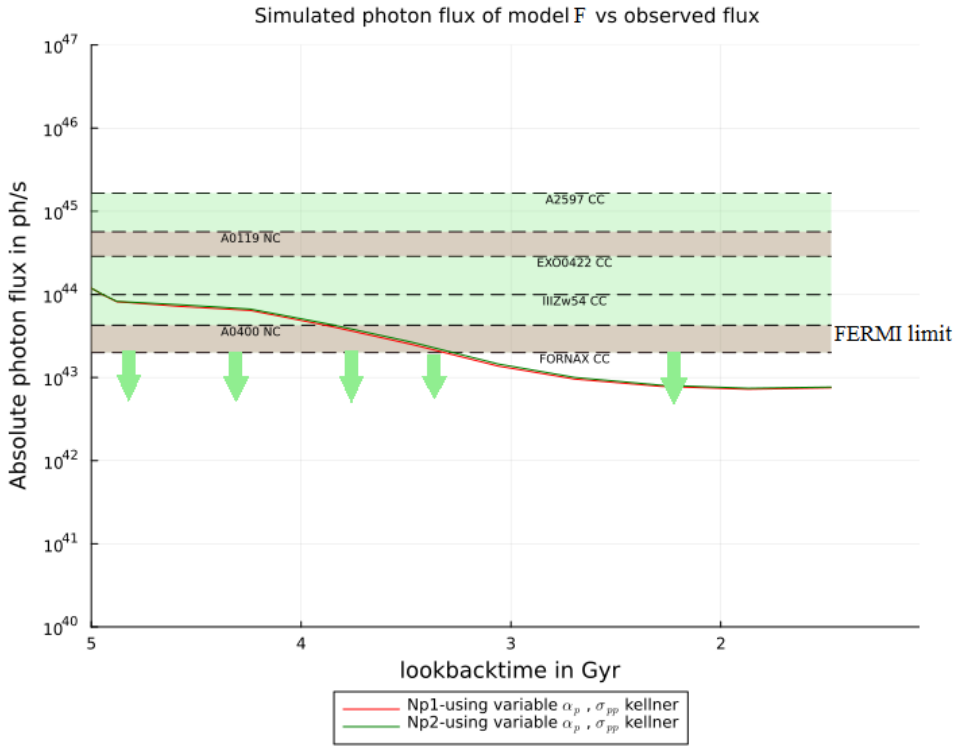

Figure 3.16: Absolute gamma ray flux calculated for the models Np1 and Np2 with a variable α_p condition using the cross-section from Eqn 2.4 for Run F.

γ-ray maps of Run F transporting cosmic rays into the ICM evolving with time

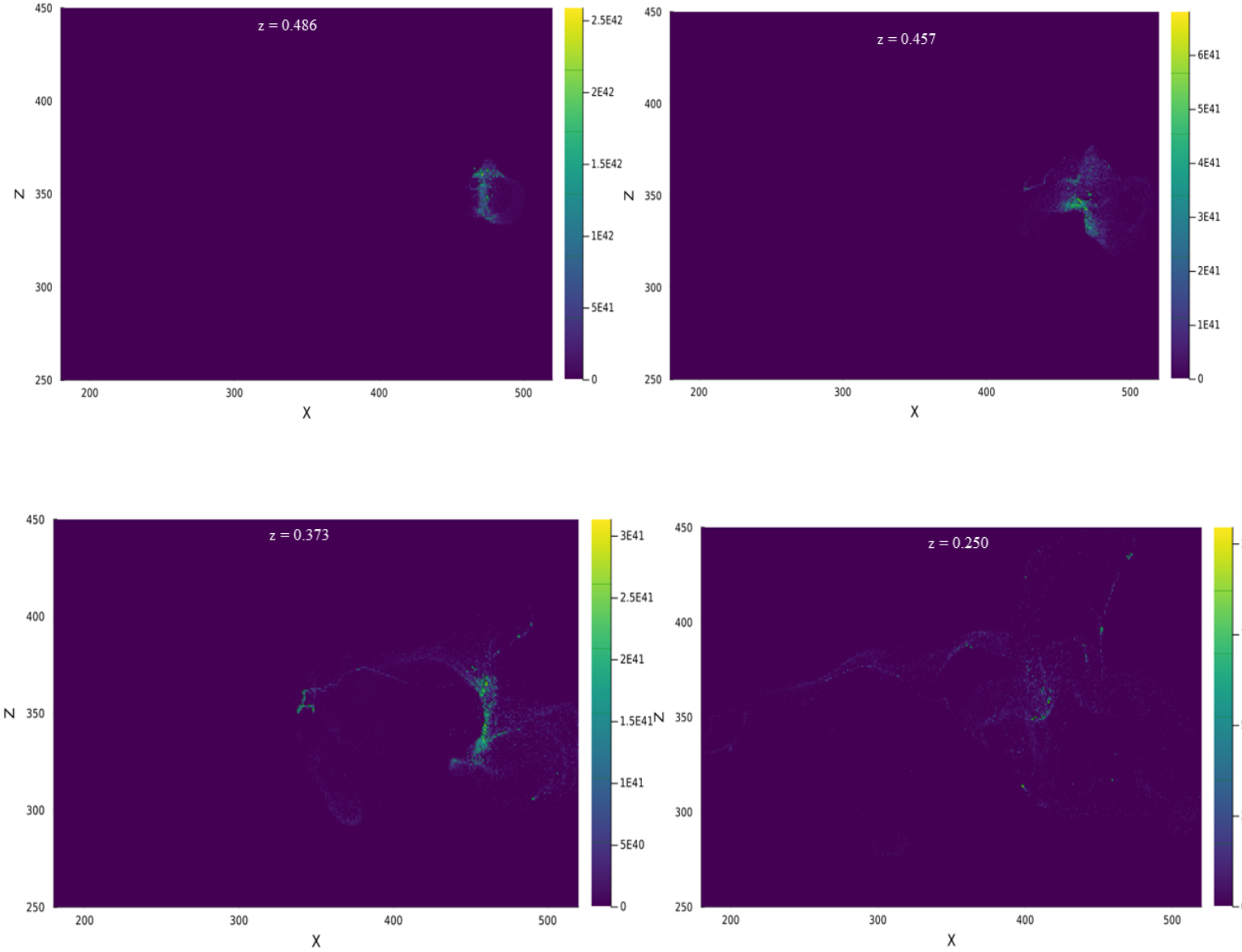

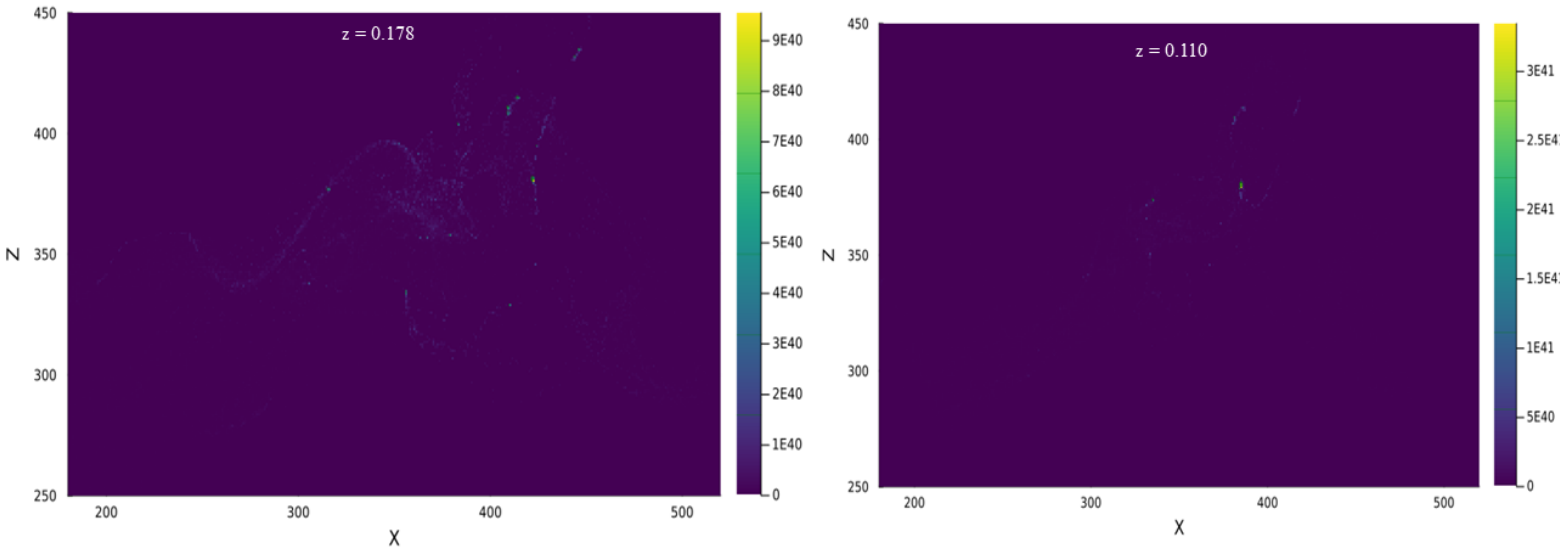

Figure 3.17: γ-ray maps representing the spatial evolution of the tracers with time into the ICM in Run F. The X and Z axes represent the distance traveled by the tracers in the respective axes in kpc and z is the redshift at which the map is being produced. The minimum resolution of the γ-ray map is 8.86 kpc. Colorbar representing the gamma-ray flux generated by individual tracer in ph/s.

To investigate the relationship between the power of AGN jets and the gamma-ray flux produced, I plotted the power of five different runs against the gamma-ray flux at the final stages, corresponding to a redshift of z = 0.11 (final redshift so that the tracers have effectively mixed with the ICM). Despite observing some changes in the flux concerning the power, the variations are not significant, hovering around the same order of magnitude. This result highlights a crucial finding: **the power of AGN does not heavily impact the gamma-ray flux compared to other parameters.** As I discussed earlier in the previous sections, the primary factors influencing the flux are the gas density and cosmic ray number density. When the power increases, the jets can reach farther distances, expanding into lower gas-dense regions in the ICM. However, at the same time, there is an increase in cosmic ray number density (Tab 2.2), which counterbalances the effect of lower gas density. As a result, the overall impact of power on the gamma-ray flux tends to remain relatively stable across different power levels.

The distinct differences between Np1 and Np2 models have been previously discussed for each run separately, and they demonstrate how various physical processes and conditions can lead to different gamma-ray flux outcomes.

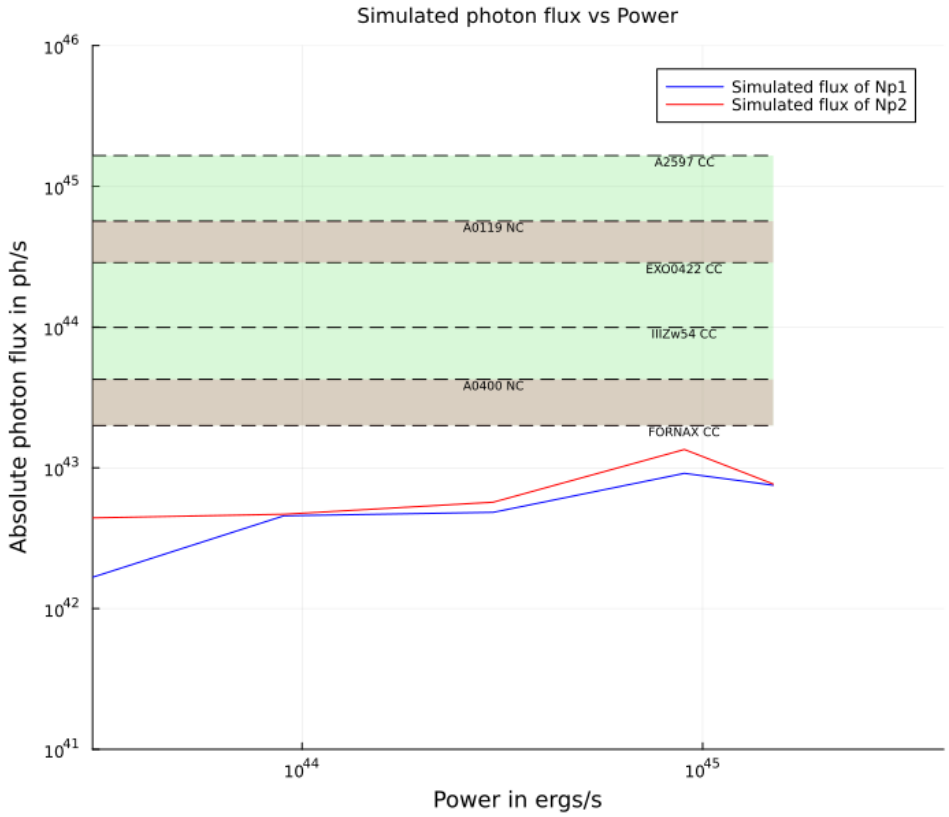

Figure 3.18: Absolute gamma ray flux calculated for the models Np1 and Np2 with a variable α_p condition using the cross-section from Eqn 2.4 for all the Runs.

3.3 Multiple radio galaxies

After I have established that the gamma-ray flux is not much affected by power in a single radio galaxy, it is important to examine the influence of multiple radio galaxies, before drawing any definitive conclusions. My dataset includes five radio galaxies, each characterized by the parameters listed in Table 2.3.

In the case of multiple radio galaxies, the resulting gamma flux is approximately an order of magnitude higher (Fig 3.19), when compared to the flux produced by a single radio galaxy alone (Fig 3.2). While the presence of multiple radio galaxies does indeed introduce various tracers into the ICM, the overall increase in flux remains relatively small, particularly in the later stages, which is mainly considered for my discussion in comparison with FERMI limits.

The nearly unchanged flux (Fig 3.19) in the later stages can be attributed to the spatial distribution of the radio galaxies within the cluster. Despite the fact that there are now five radio galaxies, the radio galaxy positioned at the cluster's center still plays a predominant role in transporting tracers into the ICM compared to the other four radio galaxies, located in the peripheral region at a lower density (Fig 2.3). The position of

radio galaxies has already been discussed in Subsec 2.2. During the initial stage, the four radio galaxies situated in the peripheral region exhibit lower power in comparison to the central radio galaxy (10^{43} erg/s). In the previous section, I established that the power of the radio galaxies does not significantly impact the gamma-ray flux produced. However, in the current context, I observe that the power of the radio galaxies does influence the distance to which the tracers can be transported into the ICM. Consequently, these peripheral radio galaxies lack the capacity to extend their lobes to significant distances.

Given that the peripheral radio galaxies are situated in low-density regions, the resulting gamma-ray flux they generate is significantly lower, and practically negligible, when compared to the flux produced by the radio galaxy positioned at the cluster's center. As a result, the gamma-ray flux produced at the early phase (z = 0.5 $\sim$ 0.4) is primarily determined by the central radio galaxy alone.

The cavities produced by the peripheral radio galaxies later as time evolves disperse the tracers through out the ICM. Thus, overall the contributions of the peripheral radio galaxies are comparatively minor in comparison to the central one. This suggests that the hadronic gamma-ray emission in real clusters of galaxies is mostly dominated by the contribution of CR injected by the central, BCG galaxies (possibly with multi bursts).

Figure 3.19: Absolute gamma ray flux calculated for the models Np1 and Np2 with a variable α_p condition using the cross-section from Eqn 2.4 for multiple radio galaxies.

I could also see a distinct difference between Np1 and Np2 model at later stages. This difference in the gamma-ray flux arises from the increased number of turbulent and shock re-acceleration events, which are a direct consequence of the presence of additional radio galaxies, accretion of sub-structures etc,. During the initial phase around $z = 0.5 \sim 0.4$, there is not much variation in the flux. However, at $z = 0.37$, I observe patches of tracers crossing shocks and turbulent re-acceleration sites, leading to a distinctive contrast in the flux behavior between Np1 and Np2 models (refer Fig 2.4). Subsequently, at $z = 0.26$, a noticeable bump (Fig 3.19) in the flux occurs as the tracers encounter shocks induced by the accretion of substructures, as discussed in Section 2.2. This analysis highlights the critical impact of turbulent and shock re-acceleration events, which becomes more evident with multiple radio galaxies than the single radio galaxy present in the Np2 model.

There are two key aspects to be discussed concerning the γ-ray maps, further reinforcing the arguments mentioned earlier:

- As previously indicated, the central radio galaxy holds a prominent position compared to the radio galaxies located in the periphery. This distinct central dominance is evident from the initial stages. For instance, at $z = 0.457$, a central radio galaxy exhibits considerably higher flux and tracers in contrast to the gamma-ray flux produced by all peripheral galaxies.

- At $z = 0.349$ and $z = 0.284$, tracers originating from all radio galaxies mix, primarily remaining in close proximity to the AGN site. Subsequently, as time progresses, these tracers undergo rapid dispersion into the surrounding medium.

γ-ray maps of multiple radio galaxies transporting cosmic rays into the ICM evolving with time

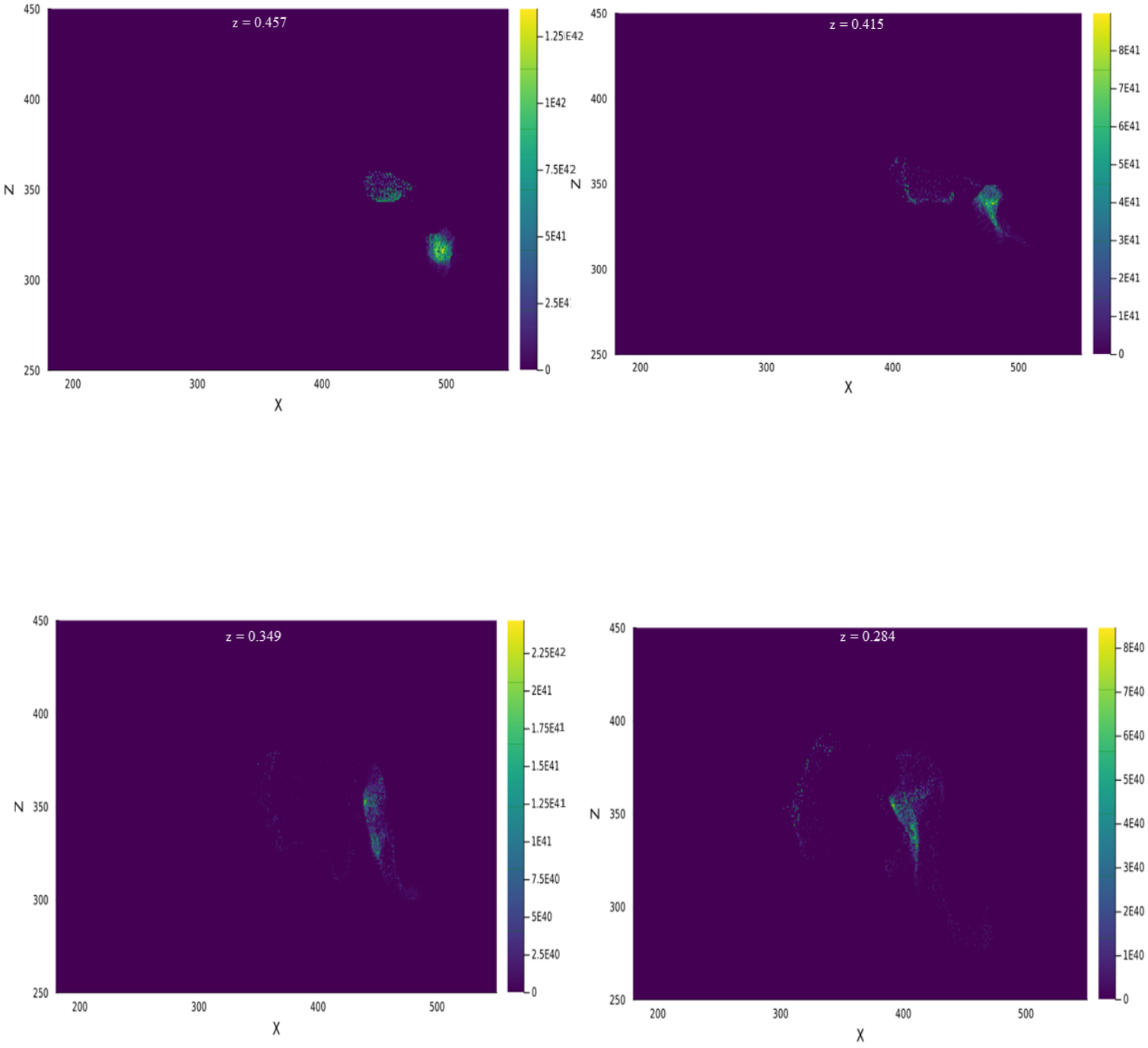

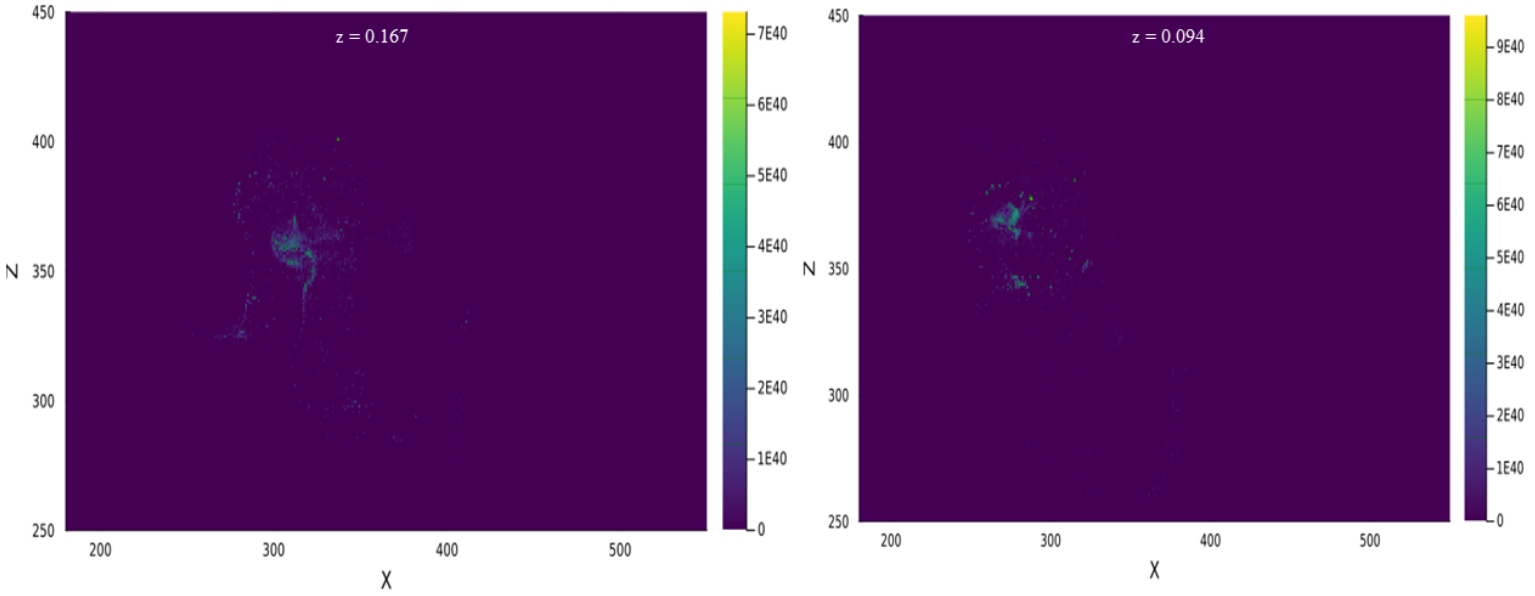

Figure 3.20: γ-ray maps representing the spatial evolution of the tracers with time into the ICM from multiple radio jets. The X and Z axes represent the distance traveled by the tracers in the respective axes in kpc and z is the redshift at which the map is being produced. The minimum resolution of the γ-ray map is 8.86 kpc. Colorbar representing the gamma-ray flux generated by individual tracer in ph/s.

Drawing a conclusion regarding the cosmic content in the jet is now possible, as it was evident in my earlier analysis with a single radio galaxy, even with just 3-4 episodes of AGN feedback, the resulting flux will exceed the FERMI limit. This holds true for multiple radio galaxies too. This observation poses a constraint on the cosmic content present in the jet.

Throughout my analysis, I assumed the initial energy of the cosmic ray proton content of the jets to be in perfect equality with the magnetic field energy ($E_B = E_{CR}$). However, when considering multiple episodes of radio bursts, the flux surpasses the FERMI limit, indicating that the assumption of equality may not hold true in this scenario. It is probable that the cosmic energy content in the jet is less than the magnetic field energy content to ensure that the flux remains below the FERMI limit. In particular, my analysis suggests that the jets in this system, fairly independent of their initial power, must have an initial energy $E_{CR} = \frac{E_B}{N_{Burst}}$, or less, where N_{Burst} is the typical number of repeated bursts for a BCG galaxy. Fixing a precise value of N_{Burst} is not possible, because the duty cycle of radio galaxies in clusters is not fully constrained by the obser-

vations. However, detailed studies of cavities in nearby clusters suggests that $N_{Burst} \geq 4$ (Sanders et al (2006), De Gasperin et al (2012), Brienza et al (2021)).

In the case of $N_{Burst} = 4$ then the jets with an initial $E_{CR} = E_B/4$ will be only allowed. This finding raises questions about the exact cosmic energy - magnetic field energy relationship in the presence of multiple radio bursts. My analysis has also shown that the flux produced by re-acceleration models is not necessarily always higher than the flux produced without them. This result highlights the critical influence of various parameters, including gas density, cosmic ray number density, and jet power, among others. As a consequence, the flux exhibits a diverse range of behaviors, varying from one model to another, rather having a uniform trend.

3.4 Neutrino flux - Single radio galaxy

I have also investigated the neutrino flux produced by clusters of galaxies to understand the contribution of extragalactic sources to the neutrino background observed by IceCube. In the hadronic scenario, the rates of various branches of the reaction indicate that for each emitted (γ)-ray photon , I expect $2\nu_\mu$, meaning two muonic neutrinos, to be produced. Additionally, I anticipate $1\nu_e$, which is one electron neutrino, for each (γ)-ray photon that interacts with a muon (μ) (Eqn 1.57). Therefore, the proton-proton interactions responsible for these processes yield not only gamma-ray photons but also neutrinos, anti-neutrinos, electrons, and positrons as final products. Thus, the resulting energy distribution can be expressed as follows:

$$E_\gamma \approx \frac{E_p}{5}$$

$$E_e \approx E_\nu \approx \frac{E_p}{20}$$

Only 1/20 of the cosmic ray proton energy is transferred to neutrinos. Therefore, to make a meaningful comparison with the IceCube limits of $10^{-8}\ GeV/s/cm^2/str$ (Ha et al. (2020)), it is crucial to choose the appropriate energy bins. For the neutrino calculations, I consider the momentum bins $20 \times 10^5 < \frac{p}{m_0 c} < 20 \times 10^6$ from the simulated spectra.

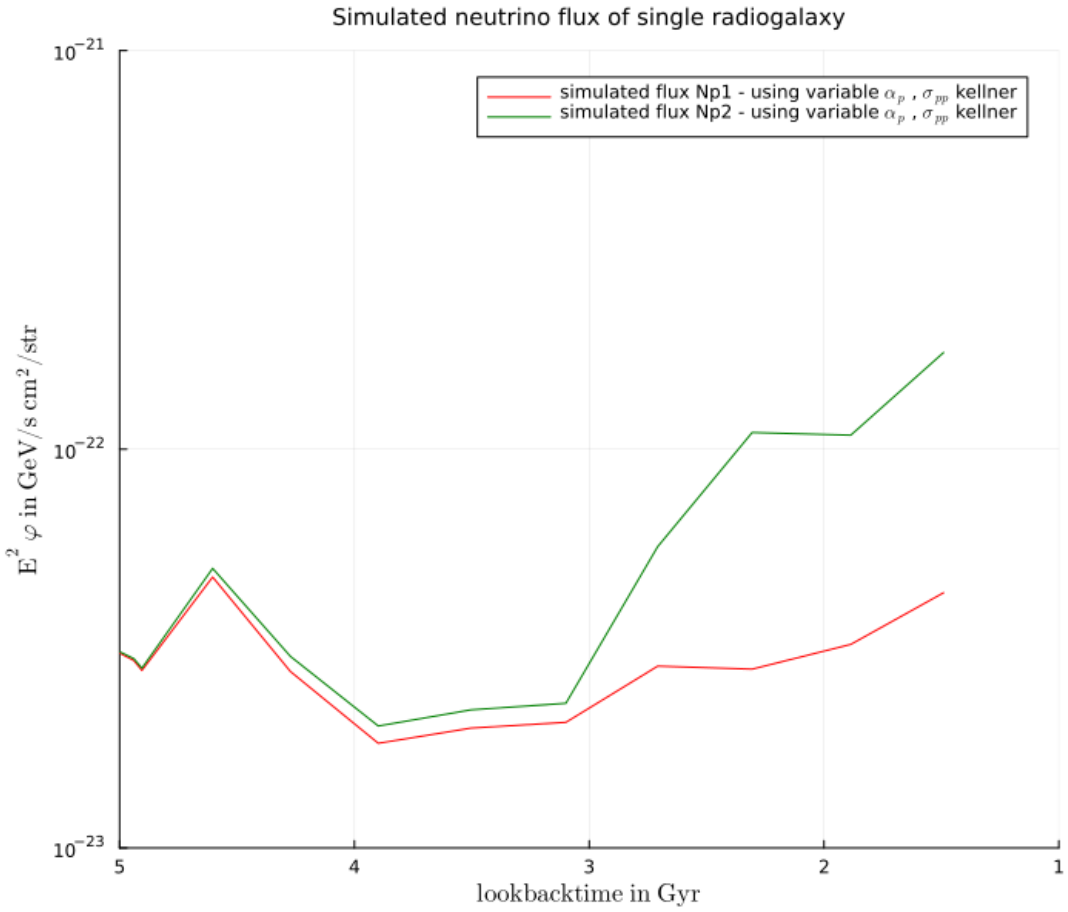

Figure 3.21: Neutrino flux calculated for the models Np1 and Np2 with a variable α_p condition using the cross-section from Eqn 2.4 for single radio galaxy (Run A), in the energy range $10^5 - 4 \times 10^6$ GeV.

Before presenting the analysis of the neutrino flux, it is important to notice that the trends of neutrino flux may differ from those of the gamma-ray flux, because of the different energy bin range. The neutrino flux shown here is generated by a single radio galaxy, based on the properties of Run A described in Table 2.1. The gamma-ray flux in 0.5-200 GeV range is produced by lower energy bins in the spectra, which are generally flat, whereas for the neutrino flux, very high energy bins are employed. At such high energies the effect of radiative losses on CR protons can become most significant, and as a result the spectral slope at larger energies can be a bit steeper. As a consequence, there is an initial drop in neutrino flux around 200 Myr after injection phase of radio jets (between 5 $\sim$ 4.8 Gyr). This is due to the power-law nature of the spectrum (at high energies), where the number of tracers at higher energies is relatively fewer compared to the number of tracers at lower energies. Consequently, this is reflected in the produced neutrino flux.

Subsequently, there is an observable rise in the neutrino flux (between 4.8 $\sim$ 4.5 Gyrs), which may be attributed to shocks encountered close to the AGN. These shocks might

re-accelerate particles to high energies, thus contributing to the increased neutrino flux. As the tracers lose energy through hadronic interactions, the neutrino flux decreases (between $4.5 \sim 4$). This dynamic behavior of the ICM near AGN is likely to explain the observed fluctuating trend of neutrino emission.

However, understanding the physics of AGN at small scales remains challenging, and many aspects of AGN behavior are still in mystery. Moreover, during the discussion of the gamma-ray flux, it was explored that between 5 - 4 Gyr, there is a transition period when the radio galaxy becomes invisible. Thus, it may be justifiable to ignore the initial part of the neutrino flux as well. After 4 Gyr, the neutrino flux tends to remain relatively constant (between 3.1 - 4.1 Gyr) as the tracers start to diffuse and spread out into the ICM. The observed phenomenon can be again attributed to the power-law nature of the specified energy bins, where high-energy tracers have already interacted with the medium, producing neutrinos, and thus, leaving behind a larger number of low-energy tracers. As these low-energy tracers diffuse into the ICM, leads to the observable effects on the neutrino flux.

Finally, after 3 Gyr, the evolution of the neutrino flux depends on their interactions with the ICM, the possibility of generating new high-energy particles, and encountering re-acceleration events.

In particular, the impact of re-acceleration events is more affected in the neutrino flux compared to the gamma-ray flux. This difference is due to the use of high-energy bins for the neutrino flux, where even a small re-energization of particles can lead to a more significant increase in flux compared to the low-energy tracers with a flat spectrum. It is also observed in Ha et al. (2020), although for a different seeding model for CRs.

3.5 Neutrino flux - Single radio galaxy with different powers

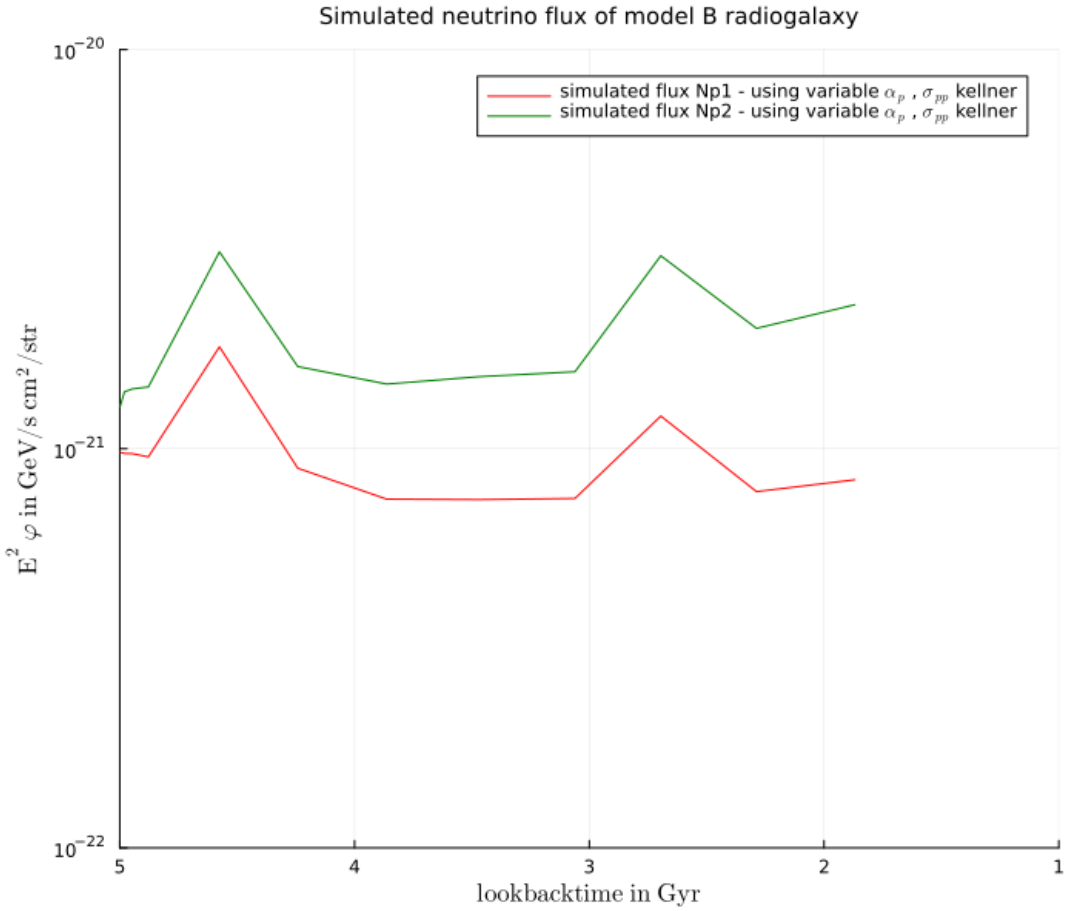

Figure 3.22: Neutrino flux calculated for the models Np1 and Np2 with a variable α_p condition using the cross-section from Eqn 2.4 for single radio galaxy in Run B, in the energy range $10^5 - 4 \times 10^6$ GeV.

Similar to gamma-ray flux, in order to understand the effects of power on neutrino flux, the latter is calculated for different powers. At first, I analyze Run B with the parameters outlined in Table 2.2. The interpretation of the trends observed in Fig 3.22 should follow the same explanation as previously described for the single radio galaxy Run A, as mentioned before Fig 3.21. In particular, the distinct difference in Np1 and Np2 in Run B should exhibit similarities to what I observed in Run B of the gamma-ray flux. With a lower power of 3×10^{44} ergs/s, the radio lobes would not have extended much further, thus being confined within a high-density region. As a consequence, this confinement would lead to a higher flux when compared to the previous run. Moreover, in this scenario, the radio lobes encounter turbulent and shock re-acceleration events, further contributing to the distinct difference between Np1 and Np2.

Between 2.75-2.5 Gyr there is an increase in the neutrino flux. At the same epoch

there is an increase in the gamma-ray flux (Fig 3.8 , 3.10, 3.19). This phenomena can be attributed to the cluster merger that happens in this object (Vazza et al (2021) A&A, Vazza et al (2023) Galaxies). During this merger, the cluster experiences heightened density due to compression motions. Subsequently, increased proton-proton collisions, leading to amplified gamma and neutrino fluxes. Additionally, this merger-induced activity gives rise to the generation of shocks and turbulence within the medium. Depending on where the CR is in each run at this epoch, this produces further difference in the model Np1 or Np2.

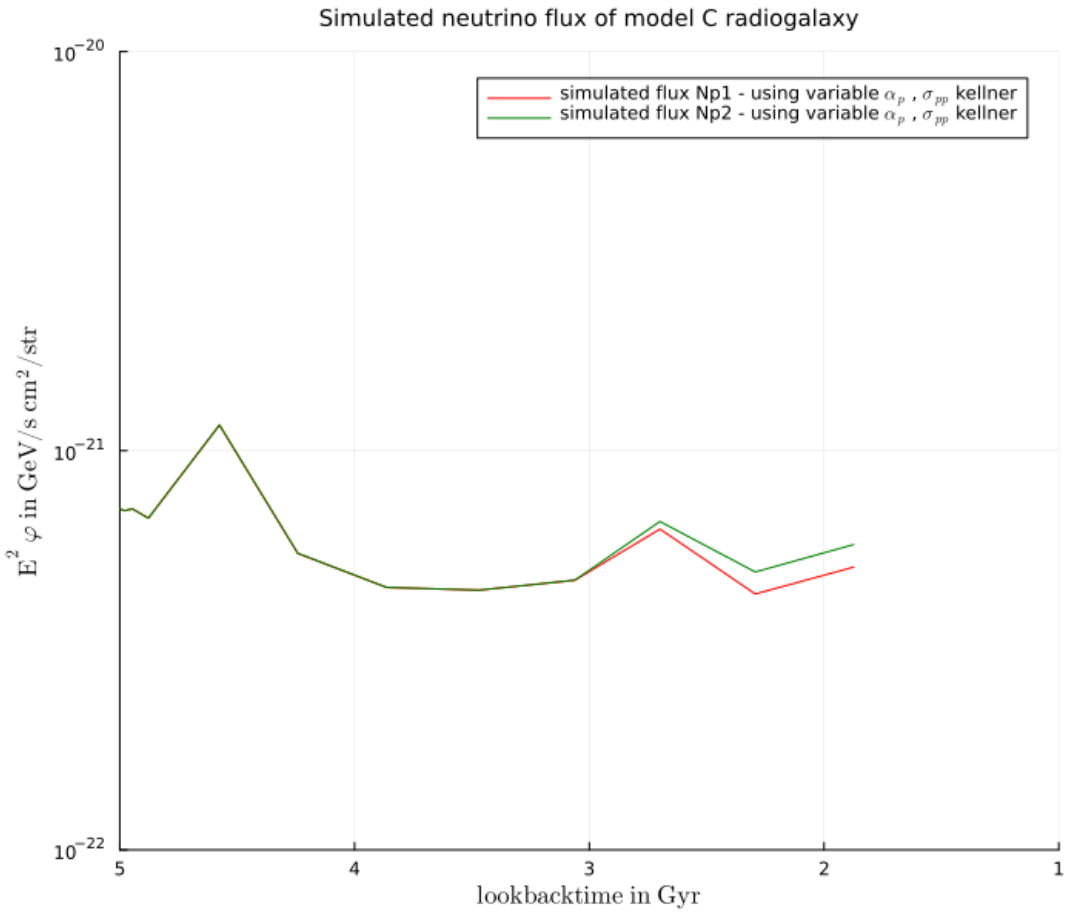

Figure 3.23: Neutrino flux calculated for the models Np1 and Np2 with a variable α_p condition using the cross-section from Eqn 2.4 for single radio galaxy in Run C, in the energy range $10^5 - 4 \times 10^6$ GeV.

An essential aspect of my investigation is to understand the impact of power on the neutrino flux, analogous to the gamma-ray flux. As I increase the power in different runs, the number of cosmic rays and cosmic ray number density increases (Tab 2.2). As a result, the number of tracers at high-energy bins decreases, leading to a reduction in the neutrino flux. This is observed in subsequent runs after B where the neutrino flux is reduced.

The trends observed in Np1 and Np2 for Run C, Run D, and Run E are expected to align with the explanations provided for the gamma-ray flux as discussed in section

3.2. The concurrence in these trends arises from the fact that both the neutrino flux and the gamma-ray flux are directly influenced by cosmic ray density and gas density. In summary, the distinct difference between Np1 and Np2 in the neutrino flux is influenced by factors such as how far the tracers can travel through jets, the gas density they encounter, and the cosmic ray number density present. These factors play a significant role in shaping the neutrino flux distribution, just as they do in the gamma-ray flux analysis.

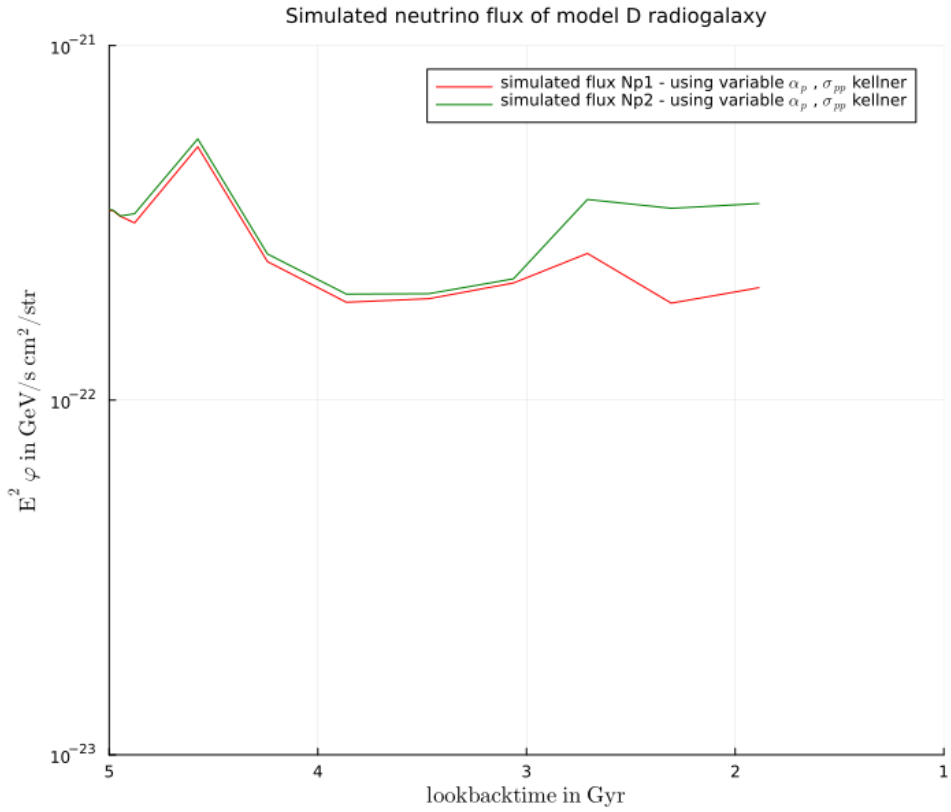

Figure 3.24: Neutrino flux calculated for the models Np1 and Np2 with a variable α_p condition using the cross-section from Eqn 2.4 for single radio galaxy in Run D, in the energy range $10^5 - 4 \times 10^6$ GeV.

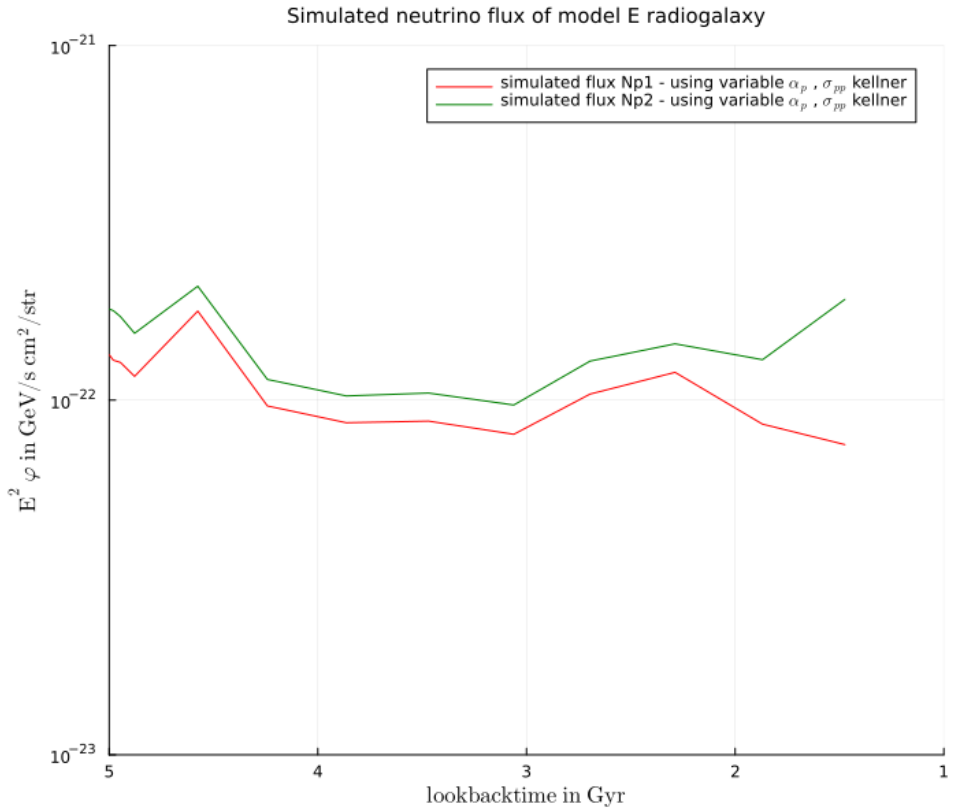

Figure 3.25: Neutrino flux calculated for the models Np1 and Np2 with a variable α_p condition using the cross-section from Eqn 2.4 for single radio galaxy in Run E, in the energy range $10^5 - 4 \times 10^6$ GeV.

Now, I focus only on Run F which has a different behaviour when compared to other runs and gamma ray flux of Run F. Run F, has the highest power of 1.5×10^{44} ergs/s. The trends observed in the gamma-ray flux (Fig 3.16) show that Np1 and Np2 models exhibit no difference, as previously discussed in Section 3.2. Also due to the high power, the cosmic rays ejected from radio galaxy in Run F can travel a farther distance. However, when I examine Fig 3.29, a notable distinction emerges between Np1 and Np2 in the neutrino flux. During the initial phase, there is a clear and abrupt jump of Np2 to a significantly higher value, rather than the gradual increase observed in other runs. This discrepancy requires a detailed explanation.

Upon further analysis of the momentum of CR spectra of Run F at different redshifts, an interesting phenomena is observed. In the early period, the cosmic ray electron spectra, appears to be steep (Figure 3.26). However, at redshift 0.449 (Figure 3.27), the cosmic ray electron spectrum suddenly became flat. This suggests that at this point, the tracers might have encountered re-acceleration events, leading to the change in their energy distribution. Due to minimal energy losses in cosmic ray protons, the effect of re-acceleration events is not clearly observable in their spectrum (It is a very small difference between CRp1 and CRp2 in Fig 3.27). However, the impact of these events is more evident in the cosmic ray electron spectrum confirming the re-acceleration sites as

seen by the sudden flattening of the spectrum in Fig 3.27.

In my analysis in the Np1 model, there is no consideration of any re-acceleration events, and the Np2 model incorporates them. In the highlighted red region of both Figure 3.27 and Figure 3.28, which is the relevant one for the production of neutrinos in the IceCube energy range, there is a slight increase in the Np2 spectra when compared to Figure 3.26. Eventhough this difference may seem negligible in a log-log plot, it has a substantial effect on the neutrino flux produced as the the impact of these re-acceleration events is more pronounced in the neutrino flux compared to the gamma ray flux, as discussed earlier.

The reason I do not observe the same effect in gamma rays is due to the fact that in all the spectra images at low energy bins (which are used for calculating gamma ray flux), there is not much difference between the Np1 and Np2 models. The distinction between these models becomes evident only at high energy bins, thereby affecting the neutrino flux significantly.

The abrupt re-acceleration observed in the spectrum could potentially be attributed to several factors. One likely explanation, also suggested by evolving electron spectrum is that the high-power jets of this model generating strong shocks in the vicinity of the AGN. Considering that assessing the true thermal particle content of the jet in this early stage might be difficult as discussed in Section 3.1. The neutrino emission at this stage should be considered with some caution.

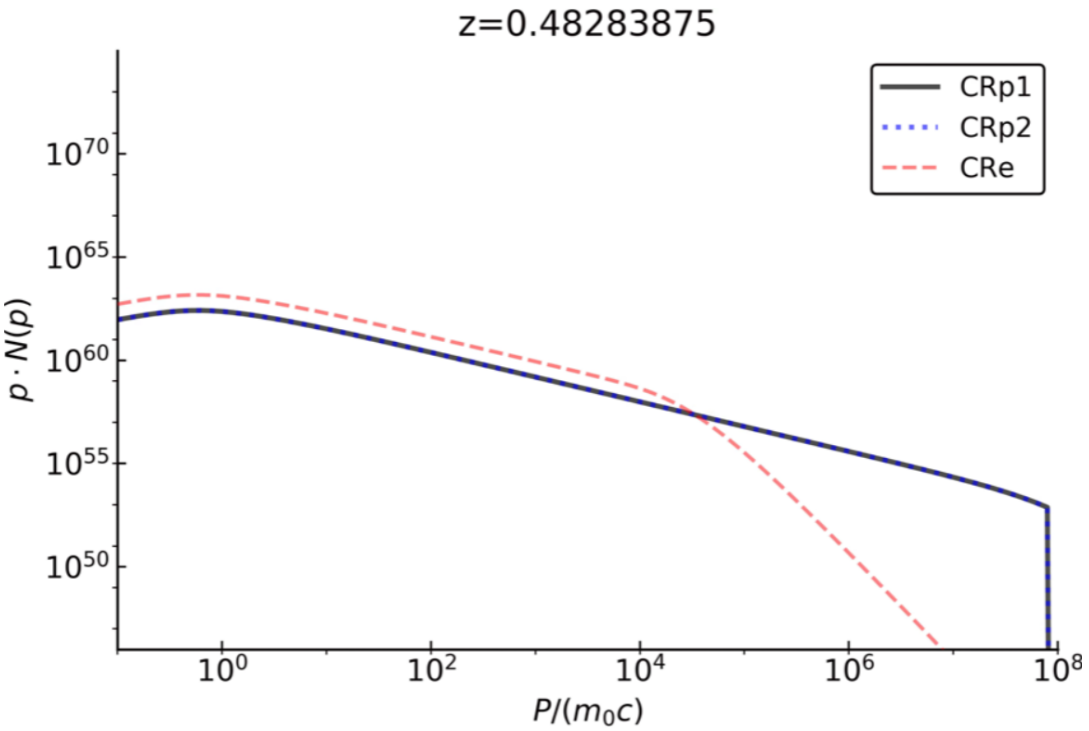

Figure 3.26: Spectra of cosmic ray protons (Np1 and Np2 model) and electrons of Run F at z = 0.482.

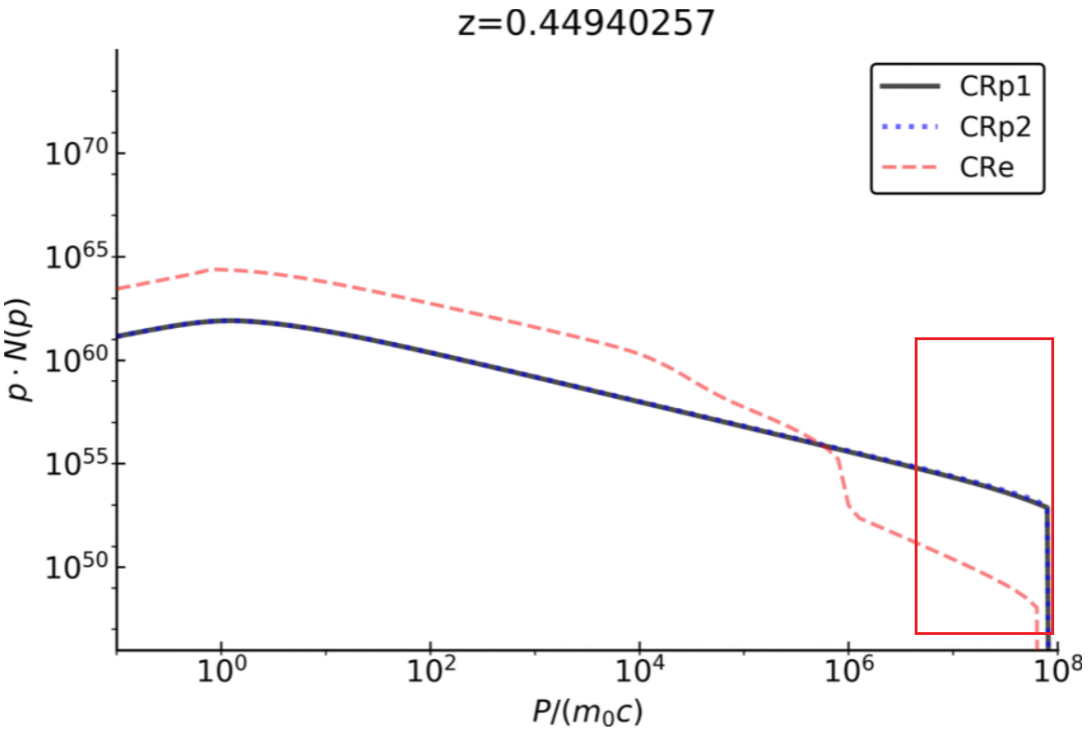

Figure 3.27: Spectra of cosmic ray protons (Np1 and Np2 model) and electrons of Run F at z = 0.449.

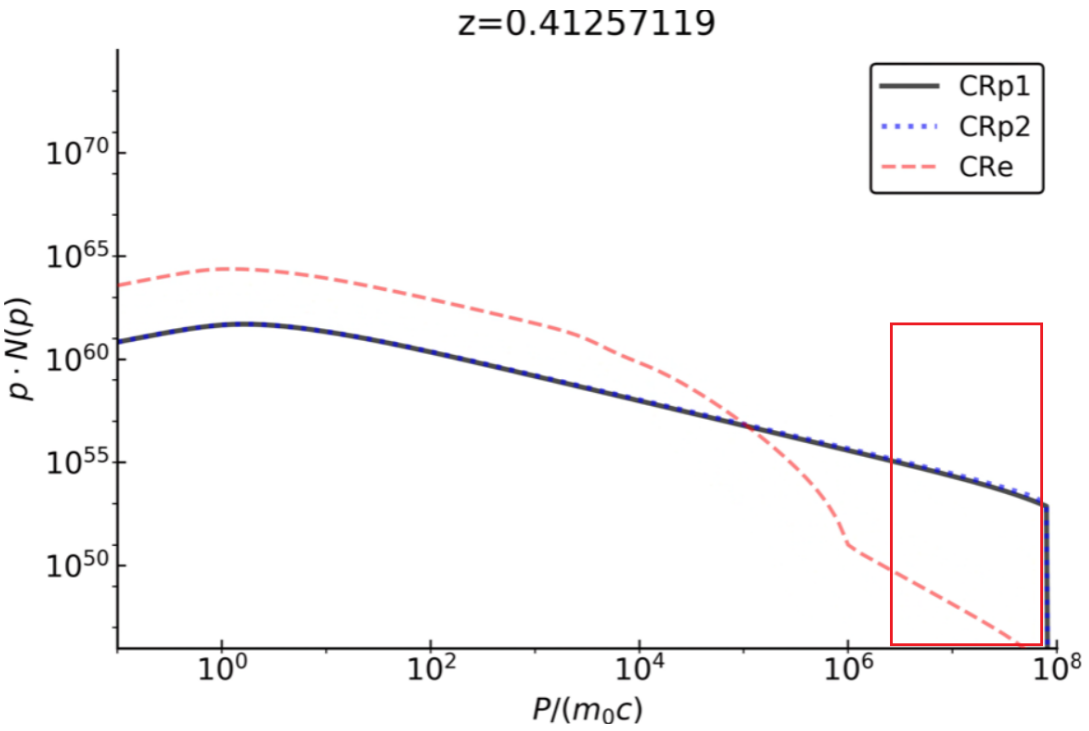

Figure 3.28: Spectra of cosmic ray protons (Np1 and Np2 model) and electrons of Run F at z = 0.412.

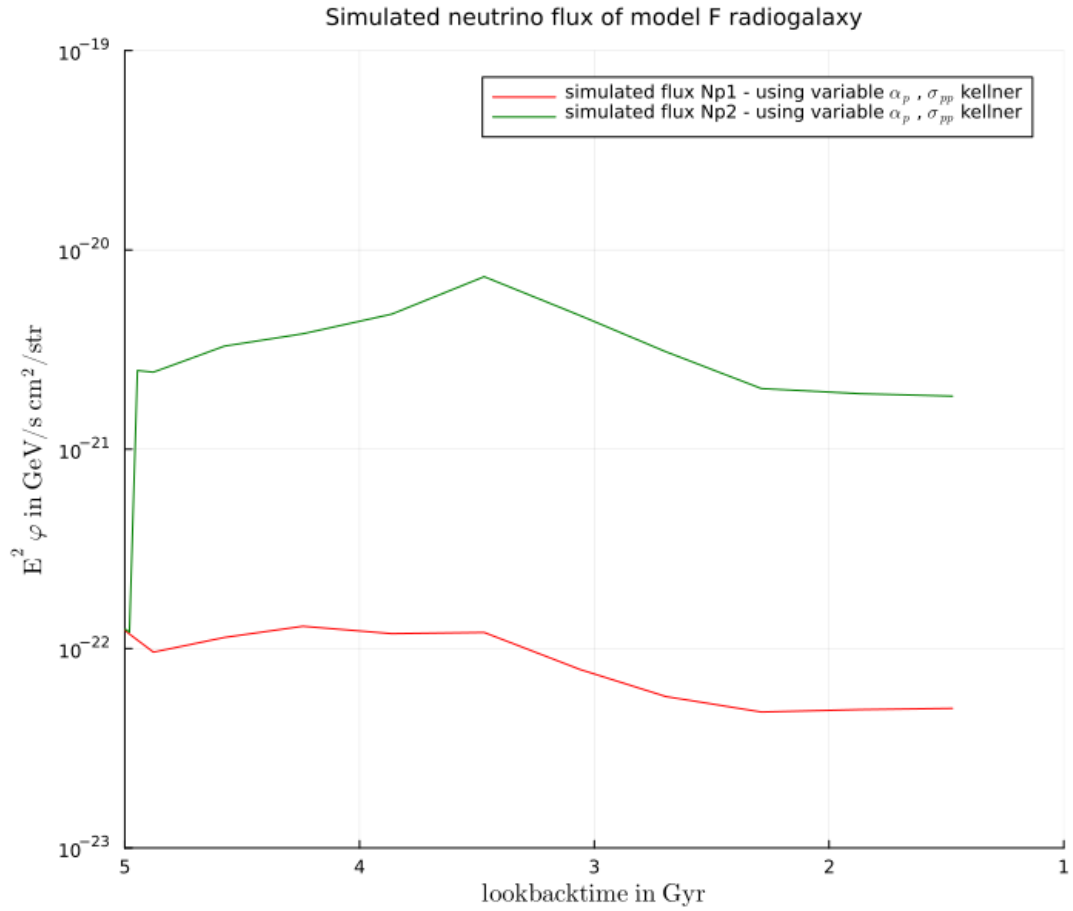

Figure 3.29: Neutrino flux calculated for the models Np1 and Np2 with a variable α_p condition using the cross-section from Eqn 2.4 for single radio galaxy Run F, in the energy range $10^5 - 4 \times 10^6$ GeV.

The neutrino flux exhibits a prominent peak at around 3.5 Gyr, following which it gradually decreases, consistent with the typical behavior of a power law in the energy bin range for neutrinos. A substantial number of low-energy tracers are left behind in the chosen energy bin for calculation, contributing to the gradual decline in the flux.

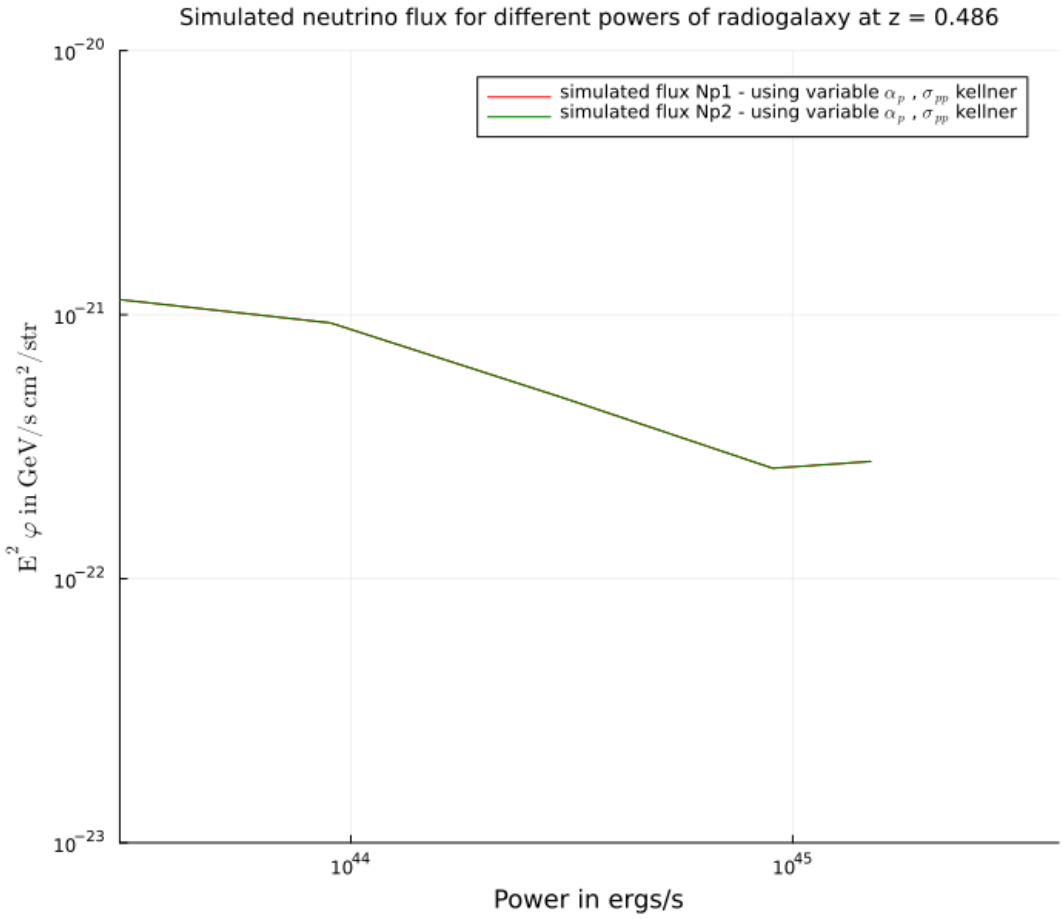

Figure 3.30: Absolute neutrino flux calculated for the models Np1 and Np2 with a variable α_p condition using the cross-section from Eqn 2.4 for all the Runs at the initial phase of jet evolution at z = 0.489.

To investigate the relation between jet power and neutrino emission, similar to the case of gamma-ray flux, I plotted the power versus neutrino flux at the initial phase of the jet in Fig 3.30 and after the jet has completely evolved in Fig 3.31. Interestingly, during the initial epoch, both the Np1 and Np2 models yielded identical fluxes. This outcome is intuitive, as it represents the early stages when the jets are still in proximity to the AGN and re-acceleration events triggered by the interaction with ICM are not present. Since re-acceleration events are yet to take place during this initial period, the fluxes produced by both models remain the same.

After the jets have evolved through the interaction with the ICM, the flux produced

for different models is very intriguing. The neutrino flux with respect to power in Fig 3.31, has a significant contrast compared to the plot obtained for the gamma ray flux in Fig 3.18. One crucial observation is that the lower energy bins have less sensitivity to changes in power compared to the higher energy bins. The neutrino flux is notably affected by power, showcasing a distinct behavior.

The power-law nature of the cosmic ray proton spectrum for the both the model implies that it is again a contribution of $n_{th} \times n_{CR}$, for CR in the energy range of IceCube, particularly these high-energy tracers are displaced out to further distances in a low-dense ICM. Consequently, this leads to a steep decline in the neutrino flux, as depicted in the plot.

Notably, in the Np2 graph, a peak in the flux is observed around 1.5 $\times 10^{45}$ erg/s. This is consistent with the discussion on how the spectra of Run F evolve in the previous paragraphs. The main takeaway is that, unlike gamma-ray flux, **the neutrino flux is strongly influenced by the power** and it can fluctuate by ~ 1 order of magnitude, depending on the input power of the jets, timing and efficiency of further re-acceleration events acting on the high energy tail of the CR population in a cluster. In general (and in a rather counter-intutive way) were powerful jet leads to ***less*** neutrino flux at later stages, because CRs are delivered to regions of the clusters with lower gas density leading to less hadronic interactions.

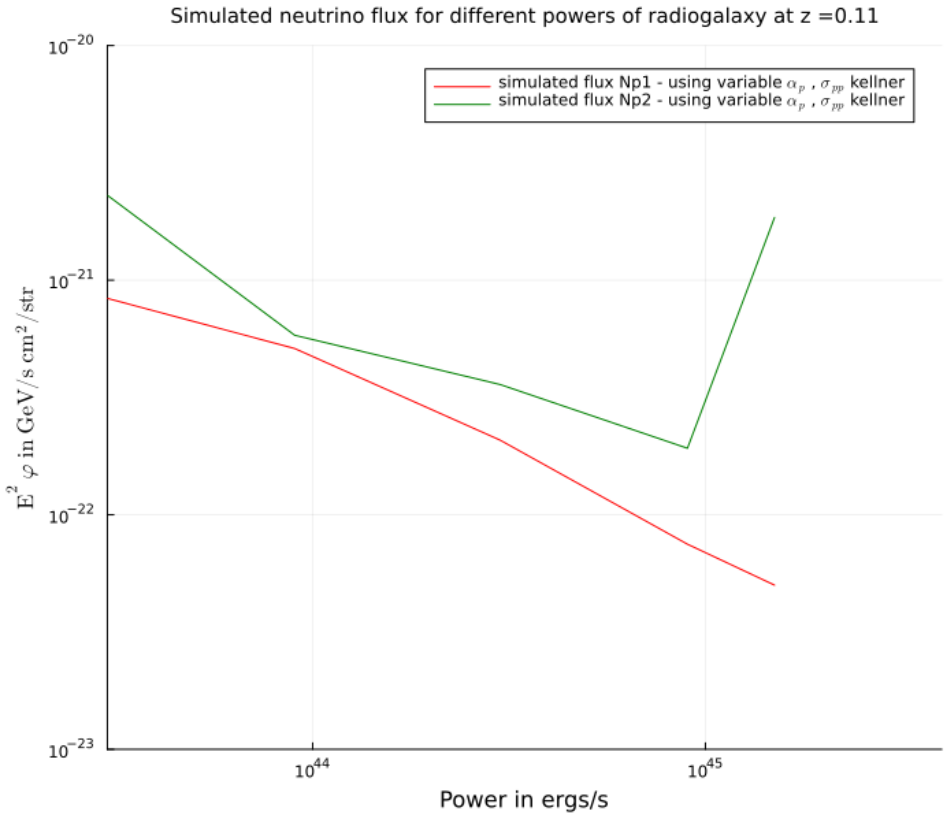

Figure 3.31: Absolute neutrino flux calculated for the models Np1 and Np2 with a variable α_p condition using the cross-section from Eqn 2.4 for all the Runs after the jet has completely evolved at z =0.110.

3.6 Neutrino flux - Multiple radio galaxies

As anticipated, the multiple radio galaxies configuration appears to have a limited impact on the flux, which can be attributed to its spatial arrangement and relatively lower power, as discussed in Section 3.3. The observed increase in neutrino flux by half, compared to the highest power at Run F, is a consequence of the central radio galaxy contributing to the neutrino flux in the multiple radio galaxies setup with a power of 1.4×10^{43} erg/s. This power is lower than the power at Run F (1.5×10^{44} ergs/s). Since the radio lobes are confined to high-density regions, they can produce more neutrino flux. Indeed, the difference between Np1 and Np2 as expected, is similar in both neutrino and gamma ray fluxes. This can be attributed to the presence of additional radio galaxies capable of facilitating re-acceleration events and promoting the accretion of sub-structures within the cluster, as discussed in Subsec 3.3 (Vazza et al (2021) A&A, Vazza et al (2023) Galaxies).

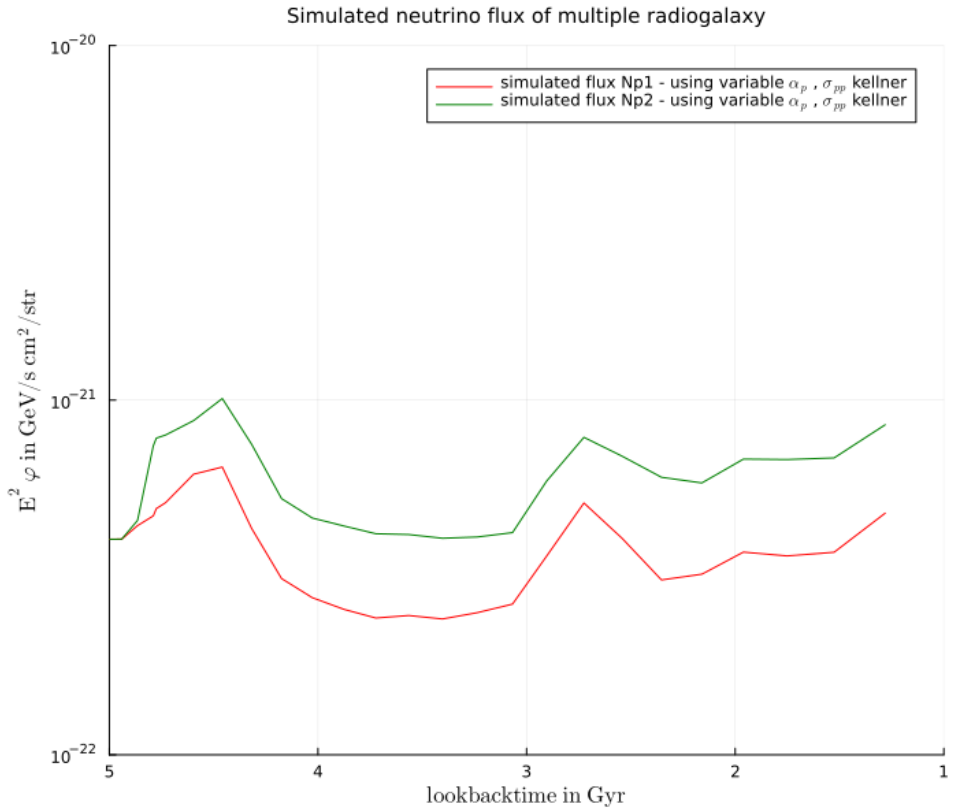

Figure 3.32: Absolute neutrino flux calculated for the models Np1 and Np2 with a variable α_p condition using the cross-section from Eqn 2.4 for multiple radio galaxies, in the energy range $10^5 - 4 \times 10^6$ GeV.

In contrast to the gamma-ray flux analysis, which allowed us to draw conclusions and establish constraints, assessing the neutrino flux requires a comparison with the IceCube limits. Since there are no detection of neutrinos from a single cluster, this result can only be seen as the basis for future work in which I will extrapolate and compare with the available constraints on the full sky neutrino background. I need to perform extrapolation and consider multiple clusters with varying masses and volumes to achieve a more meaningful comparison. This extended analysis, focusing on extrapolation, will be a part of my future research perspectives.

Chapter 4

Conclusion

In this study, my focus was on establishing the critical criteria necessary for maintaining gamma-ray flux within the bounds of the FERMILAT limit, especially by constraining the initial cosmic ray energy content in the radio jet. The intriguing characteristic of galaxy clusters lies in their capacity to efficiently accelerate and confine high-energy cosmic rays, thereby providing a unique environment for TeV - PeV neutrino production [64]. Thus, as an additional task the neutrino flux generated by cluster was calculated, exploring their contribution to the overall neutrino budget as observed by IceCube.

My analysis was built upon extensive datasets from the simulations in Vazza et al (2021) A&A, Vazza et al (2023) A&A, and Vazza et al (2023) Galaxies. These datasets encompassed scenarios involving a single radio galaxy with a fixed power, single radio galaxy with varying powers, and multiple radio galaxies. The primary aim was to identify optimal parameters for subsequent investigations of constraining the cosmic content in the radio jets and to ensure robustness, I examined different assumptions.

At first I compared between a constant α_p value and variable α_p across different momentum bins within the evolving spectra. Additionally, I conducted an in-depth analysis of two distinct proton-proton collision cross-sections and identified the most appropriate choice. The cross-section outlined in Kelner et al (2006), which is also widely used in recent literature produces reduced gamma-ray flux compared to the flux produced from pfrommer & Enslinn (2004) cross-section. Thus, in my study a variable α_p and the σ_{pp} formula from Kelner et al (2006) were used for subsequent calculations.

- From the analysis and the subsequent generation of simulated γ-ray emission from the single radio galaxy case, the derived gamma-ray flux remained below the FERMI limit. To explore the potential influence of the radio jet's power on gamma-ray flux generation, I examined a single radio jet featuring with varying power levels. This investigation revealed that the power of the radio jet does not

have much impact on the resulting gamma-ray flux. The reason for this is that high power jets have high cosmic ray number density and push the CRs farther away from the cluster core, where the density of the thermal targets is lower. Therefore, generating moreover same gamma-ray emission level for both high and low jet power. This insight, although initially unexpected, clarified that the radio jet's power is not an important parameter in the gamma-ray flux generation.

- My work also extended in analysing multiple radio galaxies (5 radio galaxies). However, the outcomes of this analysis was similar to that of a single radio galaxy. This is due to the fact that the influence of peripheral radio galaxies on the overall gamma-ray flux was overshadowed by the significant contribution of the central BCG. These analyses were systematically conducted across two distinct models: the Np1 model, characterized by the absence of shock and turbulent re-acceleration, and the Np2 model, which incorporates both shock and turbulent re-acceleration mechanisms.

- I have successfully imposed constraints on the cosmic ray composition within the jets. The simulated gamma-ray flux exceeds the FERMI limit, particularly when considering multiple occurrences of radio bursts. Initially, the cosmic ray energy content in the jets is in perfect equality with the magnetic field energy (i.e., $E_B = E_{CR}$). If they have multiple episode of radio bursts, they deviate from this equality. I can therefore deduce that the initial cosmic ray energy to be $E_{CR} = \frac{E_B}{N_{Burst}}$. From the simulation and the output plots, I found that $N_{Burst} = 4$. Thus, the permissible value for the initial cosmic ray energy (E_{CR}) within the FERMI limit is $E_B/4$ or lower.

- Several studies have already focused on constraining the cosmic ray energy distribution within jets. In a recent work by Beckmann et al (2022), on a self-regulated, cosmic-ray-dominated jets highlighted that, a significant value of the fixed energy fraction, denoted as f_{CR}, where $L_{kin} = (1-f_{CR})L_{AGN}$, is not consistent with observational data for massive clusters for very high values. To remain consistent with the FERMI gamma-ray flux limits, the study proposed that f_{CR} should be limited to a value of 0.1, or less. In summation, the study led to the deduction that the CR energy equivalent up to 10% of the AGN luminosity, or less, is required. My thesis findings align with this notion of maintaining a lower cosmic ray energy fraction. However, my approach differs from that of Beckmann et al (2022). Rather than using the kinetic energy deposited within the jets as a basis, as mentioned in their study, I have conducted my analysis starting from the perfect equality condition. This alternate perspective introduces fresh insights into the interplay between the energy of magnetic fields and cosmic rays within the jets.

- I have tested two distinct models, namely Np1 (only cooling losses) and Np2 (which also includes Fermi I and Fermi II re-acceleration), into my thesis analysis. These models have also been the subject of prior researches. A study by Ha et al. (2020), has explored the impact of shock re-acceleration on the gamma-ray flux. Remarkably, the difference in gamma-ray flux remains marginal irrespective of whether re-acceleration is introduced or not. Even in cases where re-acceleration is accounted for, the resulting flux consistently remains within the FERMI limits. This outcome aligns precisely with my findings, where the difference in gamma-ray flux between the Np2 and Np1 models is negligible across all conducted simulations. Furthermore, as emphasized earlier, the gamma-ray flux is a combination of cosmic ray number density and gas number density. The findings of Ha et al. (2020) illustrate that for the model employing $\delta = 1$ (maximum cosmic ray number density) where $n_{CR}(r,p) \propto n_{gas}(r)^{\delta}$, the gamma-ray flux was still within the FERMI limits.
- In accordance with the spectral index adopted in the study by Zandanel et al. (2015), it was established that even for values of α_p exceeding 2, the gamma-ray flux remains significantly below the threshold defined by FERMI. Their study included the injection of CRs originating from both structure formation shocks and AGN. In my thesis, I exclusively consider radio jets as the source of CRs. Although my numerical analysis integrates a variable spectral index, a substantial majority of the calculated α_p values are greater than 2. Also according to the results of Zandanel et al. (2015) a spectral index exceeding 2 corresponds to gamma-ray fluxes that are bounded by 1% of the measurements recorded by FERMI.

Just as I calculated the gamma-ray flux for all simulations, I also computed neutrino flux in higher energy bins ($20 \times 10^5 < \frac{p}{m_0 c} < 20 \times 10^6$). The findings from Zandanel et al. (2015), mentions that neutrinos remain below the IceCube limit for spectral indices $\alpha_p > 2$, a finding that matches with the outcomes of my numerical analysis. The neutrino flux derived from IceCube measurements which is set as a limit falls within the range of 10^{-8} GeV/cm^2/s/str for $E_\nu = 1PeV$.

At a spectral index value of $\alpha_p = 1.5$, the neutrino flux exhibits a magnitude comparable to that observed by IceCube, as noted in Zandanel et al. (2015). While this alignment holds true when considering a constant spectral index, in my study for a variable spectral index achieving an equivalence in magnitude with the IceCube measurement becomes unfeasible. Furthermore, to highlight that having a spectral index of $\alpha_p = 1.5$ is implausible. Such a steep spectral shape contradicts the conclusions drawn from the most recent spectral fitting of the IceCube neutrino flux, as evidenced by Aartsen et al (2014).

A similar analysis was conducted in a recent study by Hussain et al (2023), where they

ruled out the possibility of $\alpha_p \leq 2$ as a spectral index. Again, the reason behind this exclusion is that, with such a steep spectral index, the resulting neutrino flux closely approaches the IceCube limits. The energy range considered in their research was between 10^{16} to 10^{17} eV. This suggests that with particle spectra flatter than 2, galaxy clusters alone have the potential to account for the entire diffuse emission observed by the IceCube. However, recent IceCube observations have indicated that only 9-13%, of the neutrino flux originating from clusters can contribute to the overall diffuse emission detected by the IceCube. At present, a direct comparison with my results is not feasible since my findings pertain to a single cluster, whereas the IceCube results includes an entire cluster population.

Also, in Hussain et al (2023), it is mentioned that spectral indices $\alpha_p \geq 2$ is required to align with this observations. Notably, when $\alpha_p \geq 2.3$ in, the neutrino flux consistently falls below the IceCube limits. As previously highlighted, the majority of the calculated α_p values in my thesis exceed 2. This shows that my numerical analysis, even when applied to just one cluster, yields results consistent with the literature. Regarding the energy content of cosmic rays, they explored various scenarios, ranging from 0.1% to 1% of the cluster's luminosity. When cosmic rays were constrained to 0.1 times the cluster's luminosity, the gamma-ray flux consistently remained below the upper limits. But in my analysis, I adopted the equality condition, rather than relying solely on cluster luminosity or kinetic energy fractions from AGN.

The neutrino flux produced in my analysis is within the range of approximately 10^{-23} to 10^{-22} GeV/cm^2/s/str. In contrast, in Ha et al. (2020), the neutrino flux generated for nearby clusters (Coma, Perseus,Ophiuchus, Virgo and Centaurus cluster) ranged from 10^{-4} to 10^{-5} times smaller than the IceCube limits. This difference in outcomes may be attributed to the variation in the number of cluster samples used for extrapolation, as well as to the larger masses of clusters considered by Ha et al. (2020).

Another important aspect found in the simulated neutrino flux is that unlike gamma-rays, neutrinos are sensitive to jet power. Moreover, the effect of re-acceleration has more impact in neutrinos compared to the gamma-ray emission. This difference primarily arises from variations in the energy bins used for neutrino and gamma-ray emission. Specifically, higher energy bins has more impact, even with minor re-acceleration events. This aligns with the results of Ha et al. (2020), where the Np2 model demonstrated a more prominent impact on re-acceleration events in neutrino emissions than gamma-ray emissions.

To summarise the course of my thesis, I

- Constrained the cosmic ray energy content within the radio jets ($E_{CR} = E_B/4$). The cosmic ray energy budget should be $\leq 25\%$ of magnetic field energy in the radio jet. This gives a strict limit of only four multiple bursts allowed in radio galaxies to ensure that gamma-ray flux remains within the acceptable FERMI limits.

- Conducted numerical analysis of the neutrino flux for a single cluster under various conditions, including scenarios involving a single radio galaxy, a single radio galaxy with varying jet power, and multiple radio galaxies.

- Was also able to prove that the radio jet power does not affect the gamma-ray generated. Instead, the dominant factors are the number density of cosmic rays and thermal gas density. In contrast, the change in jet power has a notable impact on the neutrino flux produced. The re-acceleration events are highly sensitive to high energy bins than low energy bins thus impacting the Np2 model of neutrino emission. In the case of multiple radio galaxies, the central BCG plays a more important role in generating the gamma and neutrino flux than the peripheral galaxies do, thus behaving like a single radio galaxy.

This thesis has primarily focused on radio jets as the source of cosmic rays in the ICM. However, in reality, there are numerous other sources and accelerators to consider like shocks within the cluster, shocks in the hotspots of radio jets, or shocks resulting from the cluster merging events, all contributing to an increased number of cosmic rays. While this study has also focused on re-acceleration event due to shocks and turbulence (Np2 model), it is important to note that shocks can also inject fresh cosmic rays into the ICM. This expanded consideration of cosmic ray sources could provide more stringent constraints on the cosmic content within the radio jets, potentially leading to a reduction in the number of multiple bursts allowed. Therefore, as a future perspective, I could incorporate cosmic ray contributions from various sources, including shocks and radio jets, to gain a more comprehensive understanding of cosmic content constraints. Along with this, the primary challenge in analysing the neutrinos lies in the fact that the flux calculations were limited to a single cluster, making direct comparisons with IceCube limits impractical. To address this, my aim is to extrapolate these findings to the entire cluster population, especially in a scenario involving multiple bursts. By doing so, I will be able to establish a basis for assessing whether the constraints imposed by gamma-ray and neutrino observations align with each other.

Bibliography

[1] Gianfranco Brunetti and Thomas W Jones. Cosmic rays in galaxy clusters and their nonthermal emission. *International Journal of Modern Physics D*, 23(04):1430007, 2014.

[2] Markus Ackermann, M Ajello, A Albert, A Allafort, WB Atwood, Luca Baldini, J Ballet, G Barbiellini, D Bastieri, K Bechtol, et al. Search for cosmic-ray-induced gamma-ray emission in galaxy clusters. *The Astrophysical Journal*, 787(1):18, 2014.

[3] F Vazza, D Wittor, L Di Federico, M Brüggen, M Brienza, G Brunetti, F Brighenti, and T Pasini. Life cycle of cosmic-ray electrons in the intracluster medium. *arXiv preprint arXiv:2210.01591*, 2022.

[4] F Vazza, D Wittor, G Brunetti, and M Brüggen. Simulating the transport of relativistic electrons and magnetic fields injected by radio galaxies in the intracluster medium. *Astronomy & Astrophysics*, 653:A23, 2021.

[5] F Vazza, D Wittor, L Di Federico, M Brüggen, M Brienza, G Brunetti, F Brighenti, T Pasini, et al. Life cycle of cosmic-ray electrons in the intracluster medium. *Astron. Astrophys*, 669:A50, 2023.

[6] Franco Vazza, Denis Wittor, Marcus Brüggen, and Gianfranco Brunetti. Simulating the enrichment of fossil radio electrons by multiple radio galaxies. *Galaxies*, 11(2):45, 2023.

[7] Argyro Tasitsiomi. The state of the cold dark matter models on galactic and subgalactic scales. *International Journal of Modern Physics D*, 12(07):1157–1196, 2003.

[8] ESA hubble . `https://esahubble.org/wordbank/gravitational-lensing`.

[9] Gravitational lensing of abell cluster 2218. `https://hubblesite.org/contents/media/images/2000/07/942-Image.html`.

[10] James Binney and Scott Tremaine. *Galactic dynamics*, volume 20. Princeton university press, 2011.

[11] Hans Böhringer, Gayoung Chon, and Masataka Fukugita. The extended rosat-eso flux-limited x-ray galaxy cluster survey (reflex ii)-vii. the mass function of galaxy clusters. *Astronomy & Astrophysics*, 608:A65, 2017.

[12] M Arnaud. The β-model of the intracluster medium-commentary on: Cavaliere a. and fusco-femiano r., 1976, a&a, 49, 137. *Astronomy & Astrophysics*, 500(1):103–104, 2009.

[13] François Mernier, Jelle de Plaa, Jelle S Kaastra, Y-Y Zhang, Hiroki Akamatsu, Liyi Gu, Peter Kosec, Junjie Mao, Ciro Pinto, Thomas H Reiprich, et al. Radial metal abundance profiles in the intra-cluster medium of cool-core galaxy clusters, groups, and ellipticals. *Astronomy & Astrophysics*, 603:A80, 2017.

[14] Sofia A Cora, Luca Tornatore, Paolo Tozzi, and Klaus Dolag. On the dynamical origin of the icm metallicity evolution. *Monthly Notices of the Royal Astronomical Society*, 386(1):96–104, 2008.

[15] CL Carilli and GB Taylor. Cluster magnetic fields. *Annual Review of Astronomy and Astrophysics*, 40(1):319–348, 2002.

[16] Alfred Bennun. High energy dimensioning the quantum space-time of the electron. 2020.

[17] Gabriele Ghisellini. *Radiative processes in high energy astrophysics*, volume 873. Springer, 2013.

[18] Donald G Shirk. A practical review of the kompaneets equation and its application to compton scattering. 2006.

[19] Malcolm S Longair. *High energy astrophysics*. Cambridge university press, 2010.

[20] Wolfgang Bietenholz. The most powerful particles in the universe: a cosmic smash. *arXiv preprint arXiv:1305.1346*, 2013.

[21] Alessandra Pacini. Cosmic rays: Bringing messages from the sky to the earth's surface. *Revista Brasileira de Ensino de Física*, 39, 01 2017.

[22] A Botteon, GIANFRANCO Brunetti, Dongsu Ryu, and S Roh. Shock acceleration efficiency in radio relics. *Astronomy & Astrophysics*, 634:A64, 2020.

[23] Reinout J Van Weeren, Huub JA Röttgering, Marcus Brüggen, and Matthias Hoeft. Particle acceleration on megaparsec scales in a merging galaxy cluster. *Science*, 330(6002):347–349, 2010.

[24] Giannandrea Inchingolo, Denis Wittor, Kamlesh Rajpurohit, and Franco Vazza. Radio relics radio emission from multishock scenario. *Monthly Notices of the Royal Astronomical Society*, 509(1):1160–1174, 2022.

[25] Difference between FRI and FRII. `https://iopscience.iop.org/article/10.1088/1757-899X/452/4/042052/pdf`.

[26] MJ Hardcastle and JH Croston. Radio galaxies and feedback from agn jets. *New Astronomy Reviews*, 88:101539, 2020.

[27] Andreas Müller and Max Camenzind. Relativistic emission lines from accreting black holes-the effect of disk truncation on line profiles. *Astronomy & Astrophysics*, 413(3):861–878, 2004.

[28] Shobha Kumari and Sabyasachi Pal. A catalogue of newly discovered hybrid morphology radio (hymor) galaxies from the vla first survey. In *Conference: 21st national space science symposium*.

[29] RJ Van Weeren, F de Gasperin, H Akamatsu, Marcus Brüggen, L Feretti, H Kang, A Stroe, and F Zandanel. Diffuse radio emission from galaxy clusters. *Space Science Reviews*, 215:1–75, 2019.

[30] Myriam Gitti, Fabrizio Brighenti, and Brian R McNamara. Evidence for agn feedback in galaxy clusters and groups. *Advances in Astronomy*, 2012:1–24, 2012.

[31] Raffaella Morganti. The many routes to agn feedback. *Frontiers in Astronomy and Space Sciences*, 4:42, 2017.

[32] Alister W Graham and Nicholas Scott. The (black hole)-bulge mass scaling relation at low masses. *The Astrophysical Journal*, 798(1):54, 2014.

[33] Nicholas J McConnell, Chung-Pei Ma, Karl Gebhardt, Shelley A Wright, Jeremy D Murphy, Tod R Lauer, James R Graham, and Douglas O Richstone. Two ten-billion-solar-mass black holes at the centres of giant elliptical galaxies. *Nature*, 480(7376):215–218, 2011.

[34] Andrey V. Kravtsov and Stefano Borgani. Formation of galaxy clusters. *Annual Review of Astronomy and Astrophysics*, 50:353–409, 2012.

[35] F Santoro, C Tadhunter, D Baron, R Morganti, and J Holt. Agn-driven outflows and the agn feedback efficiency in young radio galaxies. *Astronomy & Astrophysics*, 644:A54, 2020.

[36] Andrew C Fabian. Observational evidence of active galactic nuclei feedback. *Annual Review of Astronomy and Astrophysics*, 50:455–489, 2012.

[37] Bullet cluster. https://www.esa.int/ESA$_$Multimedia/Images/2007/07/The$_$Bullet$_$Cluster2.

[38] Dongsu Ryu, Hyesung Kang, Eric Hallman, and TW Jones. Cosmological shock waves and their role in the large-scale structure of the universe. *The Astrophysical Journal*, 593(2):599, 2003.

[39] Maurizio Spurio. *Particles and astrophysics*. Springer, 2014.

[40] Rein Silberberg and CH Tsao. Spallation processes and nuclear interaction products of cosmic rays. *Physics Reports*, 191(6):351–408, 1990.

[41] Maurizio Spurio, Spurio, and Bellantone. *Probes of Multimessenger Astrophysics*. Springer, 2018.

[42] Daniel Gomez Toro. *Temporal Filtering with Soft Error Detection and Correction Technique for Radiation Hardening Based on a C-element and BICS*. PhD thesis, 12 2014.

[43] Roberto Aloisio, Veniamin Berezinsky, Pasquale Blasi, Askhat Gazizov, Svetlana Grigorieva, and Bohdan Hnatyk. A dip in the uhecr spectrum and the transition from galactic to extragalactic cosmic rays. *Astroparticle Physics*, 27(1):76–91, 2007.

[44] Christoph Pfrommer and Torsten A Ensslin. Constraining the population of cosmic ray protons in cooling flow clusters with γ-ray and radio observations: Are radio mini-halos of hadronic origin? *Astronomy & Astrophysics*, 413(1):17–36, 2004.

[45] RJ van Weeren, TW Shimwell, A Botteon, G Brunetti, M Brüggen, JM Boxelaar, R Cassano, G Di Gennaro, F Andrade-Santos, E Bonnassieux, et al. Lofar observations of galaxy clusters in hetdex-extraction and self-calibration of individual lofar targets. *Astronomy & Astrophysics*, 651:A115, 2021.

[46] Shao-Qiang Xi, Xiang-Yu Wang, Yun-Feng Liang, Fang-Kun Peng, Rui-Zi Yang, and Ruo-Yu Liu. Detection of gamma-ray emission from the coma cluster with fermi large area telescope and tentative evidence for an extended spatial structure. *Physical Review D*, 98(6):063006, 2018.

[47] Denis Wittor, Franco Vazza, Dongsu Ryu, and Hyesung Kang. Limiting the shock acceleration of cosmic ray protons in the icm. *Monthly Notices of the Royal Astronomical Society: Letters*, 495(1):L112–L117, 2020.

[48] Ji-Hoon Ha, Dongsu Ryu, and Hyesung Kang. Gamma-ray and neutrino emissions due to cosmic-ray protons accelerated at intracluster shocks in galaxy clusters. *The Astrophysical Journal*, 892(2):86, 2020.

[49] Kohta Murase, Susumu Inoue, and Shigehiro Nagataki. Cosmic rays above the second knee from clusters of galaxies and associated high-energy neutrino emission. *The Astrophysical Journal*, 689(2):L105, 2008.

[50] Kohta Murase, Markus Ahlers, and Brian C Lacki. Testing the hadronuclear origin of pev neutrinos observed with icecube. *Physical Review D*, 88(12):121301, 2013.

[51] Fabio Zandanel, Irene Tamborra, Stefano Gabici, and Shin'ichiro Ando. High-energy gamma-ray and neutrino backgrounds from clusters of galaxies and radio constraints. *Astronomy & Astrophysics*, 578:A32, 2015.

[52] Kohta Murase and Eli Waxman. Constraining high-energy cosmic neutrino sources: implications and prospects. *Physical Review D*, 94(10):103006, 2016.

[53] Greg L Bryan, Michael L Norman, Brian W O'Shea, Tom Abel, John H Wise, Matthew J Turk, Daniel R Reynolds, David C Collins, Peng Wang, Samuel W Skillman, et al. Enzo: An adaptive mesh refinement code for astrophysics. *The Astrophysical Journal Supplement Series*, 211(2):19, 2014.

[54] Andreas Dedner, Friedemann Kemm, Dietmar Kröner, C-D Munz, Thomas Schnitzer, and Matthias Wesenberg. Hyperbolic divergence cleaning for the mhd equations. *Journal of Computational Physics*, 175(2):645–673, 2002.

[55] Peng Wang, Zhi-Yun Li, Tom Abel, and Fumitaka Nakamura. Outflow feedback regulated massive star formation in parsec-scale cluster-forming clumps. *The Astrophysical Journal*, 709(1):27, 2009.

[56] JH Croston, J Ineson, and MJ Hardcastle. Particle content, radio-galaxy morphology, and jet power: all radio-loud agn are not equal. *Monthly Notices of the Royal Astronomical Society*, 476(2):1614–1623, 2018.

[57] Nadia Biava, Marisa Brienza, Annalisa Bonafede, Myriam Gitti, Etienne Bonnassieux, Jeremy Harwood, Alastair C Edge, Christopher J Riseley, and Adrian Vantyghem. Constraining the agn duty cycle in the cool-core cluster ms 0735.6+ 7421 with lofar data. *Astronomy & Astrophysics*, 650:A170, 2021.

[58] Gianfranco Brunetti and Franco Vazza. Second-order fermi reacceleration mechanisms and large-scale synchrotron radio emission in intracluster bridges. *Physical Review Letters*, 124(5):051101, 2020.

[59] Ricarda S Beckmann, Yohan Dubois, Alisson Pellissier, Valeria Olivares, Fiorella L Polles, Oliver Hahn, Pierre Guillard, and Matthew D Lehnert. Cosmic rays and thermal instability in self-regulating cooling flows of massive galaxy clusters. *Astronomy & Astrophysics*, 665:A129, 2022.

[60] Stanislav R Kelner, Felex A Aharonian, and Vistcheslav V Bugayov. Energy spectra of gamma rays, electrons, and neutrinos produced at proton-proton interactions in the very high energy regime. *Physical Review D*, 74(3):034018, 2006.

[61] Georgi Kokotanekov, Michael W Wise, Martijn de Vries, and Huib T Intema. Signatures of multiple episodes of agn activity in the core of abell 1795. *Astronomy & Astrophysics*, 618:A152, 2018.

[62] AC Fabian, Jeremy S Sanders, GB Taylor, SW Allen, CS Crawford, RM Johnstone, and K Iwasawa. A very deep chandra observation of the perseus cluster: shocks, ripples and conduction. *Monthly Notices of the Royal Astronomical Society*, 366(2):417–428, 2006.

[63] F De Gasperin, E Orrú, M Murgia, A Merloni, H Falcke, R Beck, R Beswick, L Bîrzan, A Bonafede, M Brüggen, et al. M 87 at metre wavelengths: the lofar picture. *Astronomy & astrophysics*, 547:A56, 2012.

[64] Ke Fang and Angela V Olinto. High-energy neutrinos from sources in clusters of galaxies. *The Astrophysical Journal*, 828(1):37, 2016.

[65] Mark G Aartsen, M Ackermann, J Adams, JA Aguilar, M Ahlers, M Ahrens, D Altmann, T Anderson, C Arguelles, TC Arlen, et al. Observation of high-energy astrophysical neutrinos in three years of icecube data. *Physical review letters*, 113(10):101101, 2014.

[66] Saqib Hussain, Giulia Pagliaroli, and Elisabete M Pino. High-energy neutrino and gamma ray production in clusters of galaxies. *arXiv preprint arXiv:2307.15851*, 2023.